UNIVERSITY OF CALIFORNIA
RIVERSIDE

Characterizing the Pathways That Initiate and Stop Dynamic Blebbing in Human Embryonic Stem Cells

A Dissertation submitted in partial satisfaction
of the requirements for the degree of

Doctor of Philosophy

in

Cell, Molecular, and Developmental Biology

by

Nikki Jo-Hao Weng

August 2016

Dissertation Committee:
Dr. Prue Talbot, Chairperson
Dr. Bir Bhanu
Dr. Jiayu Liao

The Dissertation of Nikki Jo-Hao Weng is approved:

_____

_____

_____

Committee Chairperson

University of California, Riverside

Acknowledgements

The text and figures in Chapter 2, in part or in full, are reprint of the materials as it appear in Springer book/ Video Bioinformatics, Chapter 8/ A Video Bioinformatics Method to Quantify Cell Spreading and Its Application to Cells Treated with Rho-Associated Protein Kinase and Blebbistatin, Volume 22, 2015, pp.151-166, Jo-Hao Weng; George Phandthong; Prue Talbot, with permission of Springer. The co-author (George Phandthong) listed in this publication helped with data analysis. The co-author (Dr. Prue Talbot) listed in this publication directed and supervised the research which forms the basis for this chapter.

The text and figures in Appendix A, in part or in full, are reprint of the materials as it appear in Springer book/ Video Bioinformatics, Chapter 7/ Bio-Inspired Segmentation and Detection Methods for Human Embryonic Stem Cells, Volume 22, 2015, pp.135-150, Benjamin X. Guan, Bir Bhanu, Prue Talbot, Nikki Jo-Hao Weng with permission of Springer. The co-author (Benjamin X. Guan) listed in this publication generated the program and wrote the manuscript. The co-author (Nikki Weng) listed in this publication helped with collecting all the video data. The co-authors (Dr. Prue Talbot and Dr. Bir Bhanu) listed in this publication directed and supervised the research which forms the basis for this chapter.

The text and figures in Appendix B, in part or in full, are reprint of the materials as it appear in 2014 IEEE. Reprinted, with permission, from Benjamin X. Guan, Bir Bhanu, Prue Talbot, Sabrina Lin, Nikki Jo-Hao Weng, Comparison of Texture Features for Human Embryonic Stem Cells with Bio-Inspired Multi-Class Support Vector Machine. IEEE. ICIP, Oct. 2014. The co-author (Benjamin X. Guan) listed in this publication

generated the program and wrote the manuscript. The co-authors (Dr. Prue Talbot and Dr. Bir Bhanu) listed in this publication directed and supervised the research which forms the basis for this chapter. The co-author (Nikki Weng and Dr. Sabrina Lin) listed in this publication helped with collecting video data.

The text and figures in Appendix C, in part or in full, are reprint of the materials as it appear in 2011 IEEE. Reprinted, with permission, from Benjamin X. Guan, Bir Bhanu, Prue Talbot, Nikki Jo-Hao Weng, Extraction of Blebs in Human Embryonic Stem Cell Videos. IEEE. Computational Biology and Bioinformatics, 2011. The co-author (Benjamin X. Guan) listed in this publication generated the program and wrote the manuscript. The co-author (Nikki Weng) listed in this publication helped with collecting all the video data. The co-authors (Dr. Prue Talbot and Dr. Bir Bhanu) listed in this publication directed and supervised the research which forms the basis for this chapter.

This dissertation would not have been possible without the help of so many people in so many ways. My deep gratitude goes first to my adviser Dr. Prue Talbot, who expertly guided me through my entire PhD and who provided a conducive lab environment. Her unwavering enthusiasm for sciences kept me constantly engaged with my research, and her personal generosity helped make my time at UCR enjoyable. My appreciation also extends to my dissertation committee members, Dr. Bir Bhanu and Dr. Jiayu Liao, for proving feedback and suggestions every year. I am grateful to Dr. Martins-Green for providing the prostate cancer cell, Dr. Leah Haimo for providing some inhibitors and her advice for the first 3 years.

I would like to acknowledge the contributions of several people for helping my research. I thank Dr. Sabrina Lin for collecting BioStation IM data of mouse embryonic stem cell, prostate cancer cell, and mouse embryonic fibroblast. I also thank George Phandthong for help with data analysis for Chapter 2 and Dr. Cindy Cheung for help with data collection for Chapter 3. I am thankful to undergrads, Henry Yip and Brenda Montes who helped collect and analyze for parts of the project. I am also thankful to Ben Guan for the contributions of the projects which are presented in the appendix.

I thank California Institute for Regenerative Medicine, NSF IGERT, and Academic Senate for providing funding to develop of this project.

I would also like to thank Dr. Sabrina Lin, Dr. Vasundhra Bahl, Dr. Vijayalekshmi Nair, Rachel Behar, Monique Williams, Barbra Davis, Atena Zahedi, Careen Khachatoorian, Giovanna Pozuelos, and Yuhuan Wang for helping with research work and being amazing friends. Last but not least, I would like to thank my parents, younger sister Sherry, and lovely friends for their unwavering support throughout my Ph.D. years and in life in general.

Dedication

This dissertation is dedicated to my parents, I-Hsin Weng and Fong-Wu Chiang. They have raised me to be the person I am today and have been with me every step of the way through the good times and the bad. Their unconditional love, guidance, and support have helped me to accomplish everything that I have today. I appreciate their sacrifices and I wouldn't have been able to get to this stage without them.

ABSTRACT OF THE DISSERTATION

Characterizing the Pathways That Initiate and Stop Dynamic Blebbing in Human Embryonic Stem Cells

by

Nikki Jo-Hao Weng

Doctor of Philosophy, Graduate Program in Cell, Molecular, and Developmental Biology
University of California, Riverside, August, 2016
Dr. Prue Talbot, Chairperson

Dynamic blebs are membrane protrusions on the surface of healthy cells that function in cell division and migration. The purpose of this dissertation was to discover better methods to control dynamic blebbing by identifying pathways that initiate and inhibit blebbing in human embryonic stem cells (hESC). Live cell imaging experiments demonstrated that dynamic and apoptotic blebbing were morphologically and temporally distinct during passaging of hESC. Dynamic blebs retracted faster than apoptotic blebs and had an intact cytoskeleton. Dynamic blebbing was prolonged by depolymerization of microtubules and stopped by drugs that disrupted actin microfilaments or inhibited myosin II. Plating on laminin-521 or Matrigel overcoated with laminin-111 efficiently stopped blebbing by activating an integrin-focal adhesion kinase pathway.

To identify the pathway that initiates dynamic blebbing, we tested the hypothesis that the P2X7 calcium channel is activated by ATP released during passaging. Immunocytochemistry and PCR showed that the P2X7 receptor is expressed in hESC, but not in cells starting differentiation. P2X7 inhibitors and siRNA decreased dynamic

blebbing. Extracellular ATP concentration increased during passaging. While apyrase, which degrades ATP, reduced the percentage of blebbing cells, addition of ATP to the culture medium prolonged blebbing. When Ca^{2+} was chelated by either EGTA or BAPTA, dynamic blebbing was inhibited. Rac activation was associated with decreased blebbing and cell attachment, while blebbing was activated though the ROCK pathway. These data support the idea that dynamic blebbing in hESC is initiated by extracellular ATP binding to P2X7, allowing Ca^{2+} influx which in turn initiates dynamic blebbing via the ROCK- myosin II pathway. Decreased extracellular ATP is accompanied by activation of Rac, cessation of blebbing, and attachment.

These results introduce better ways to control dynamic blebbing and improve cell survival during passaging. The use of P2X7 inhibitors and laminin substrates enables attachment and improves single hESC plating efficiency, which will facilitate quantitative work in drug discovery and toxicology. These results also introduce: (1) P2X7 as a cell surface marker for pluripotency; (2) hESC as an excellent model for studying dynamic blebbing and (3) the possibility of using hESC, which are similar to epiblast cells, to study cell movements during gastrulation.

Table of Contents

List of Figures

intervals for hESC, 60 second intervals for prostate cancer cells and mEF, and 120 second intervals for mESC. The percentage of blebbing and attached cells were significantly different for hESC than for the other cell types. F and G were analyzed by two-way ANOVA. *** = p<0.001. (H, I) Morphological and temporal comparisons of four patterns of blebbing behavior in hESC. (H) Phase contrast images of hESC at various times in culture showing the four patterns of behavior (DB = dynamic blebbing; A = attached; AB = apoptotic blebbing; R = rounding). Dynamic blebs appear dense, while apoptotic blebs are bright. (I) Percentage of cells in each of the behavior groups shown in H over 225 minutes of incubation. Each group is based on a count of 25 cells. The average time to attachment, rounding, or apoptotic blebbing ± the standard deviation is shown. The percentage of cells in each group is given on the Y axis. (J) Gray means of dynamic blebs and apoptotic blebs were analyzed using ImageJ followed by a t-test. *** p< 0.001. ……67

Figure 3.2: Verification of cell death and comparison of expansion and retraction times. (A-H) Phase contrast (A-D) and fluorescence images (E-H) at various times in culture showing that dynamically blebbing cells (E-G) have a strong fluorescence which is lost in apoptotic cells (H). (I-T) Phase contrast (I-N) and fluorescence images (O-T) at various times in culture showing cells preloaded with Magic Red. Dynamically blebbing and attached cells (I-J and O-P) do not show fluorescence. Cells undergoing apoptosis (L-N and R-T) have red fluorescence indicative of activation of caspase 3 & 7. (U) The frequency of dynamic and apoptotic blebs in various time intervals of bleb formation. (V) The frequency of dynamic and apoptotic blebs in various time intervals of retraction. Both frequency graphs are based on 80 dynamic and 69 apoptotic cells from three

Figure 4.6: Rho and Rac Regulate Dynamic Blebbing and Cell Attachment hESC (A, B) Dynamic blebbing was fully inhibited and attachment was accelerated in hESC treated with Y27632. Analyses were done by counting the percentage of blebbing and attached cells in three different BioStation videos at 20 minute intervals. Data are plotted as the means ± standard deviations of three independent experiments. (C, D) Cells treated with NSC23766, a Rac inhibitor, underwent more blebbing and less attachment than the control groups. Analyses were done by counting the percentage of blebbing and attached cells in three different BioStation videos at 12 minute intervals. Data in C and D are plotted as the means ± standard deviations of three experiments. (E, F) hESC were nucleofected with GFP-RAC activated plasmid and incubated in a BioStation IM. Phase contrast and fluorescence images of single cells are shown in at 3 and 6 hours of incubation. (F) Dynamic blebbing was inhibited in hESC after nucleofection. The D0 cells were plated and imaged in the BioStation right after nucleofection, while in the D5 cells were grown for 5 days before replating and imaging with the BioStation. Analyses were done by counting the percentage of blebbing and non-blebbing cells in nine different BioStation videos in three independent biological samples. (G, H) Blebbing cells were removed from the plates, then plated on non-coating dishes for 1 hour at 37°C. Lysates of attached and blebbing cells were collected and went through the pull-down assay to monitor Rac1 and Rho activation. (G) Western blotting showed the expression of Rac-GTP was higher in attached cells than in dynamic blebbing cells. Quantification of western blot was done by ImageJ with three independent experiments. (H) Western blotting showed the expression of Rho-GTP was higher in dynamically blebbing cells than in attached cells. * = $p < 0.05$, ** = $p < 0.01$, *** = $p < 0.001$……..115

Chapter 1: Introduction

Stem Cells

Overview: Stem cells are present in many tissues, and they are usually named according to their source. For example, embryonic stem cells come from embryos, while adipose stem cells come from fat. Until 1981, most research with stem cells was done using adult stem cells, which are limited in their ability to differentiate and are usually restricted to the lineages that they normally give rise to *in vivo*. Research on adult stem cells has generated a great deal of excitement and numerous publications. Researchers have found adult stem cells in many different tissues and new sources of adult stem cells are being found each year [1]. These discoveries give researchers opportunities to develop stem cell therapies. In fact, adult hematopoietic, or blood-forming stem cells from bone marrow, have been used in transplants for more than 40 years [2]. Stem cells from bone marrow and adipose tissue are currently used by many physicians to treat joint problems, although these procedures are not FDA approved [3,4]. Adult stem cells are believed less likely to initiate rejection after transplantation and less likely to form tumors. In principle, adult stem cells could be obtained from a patient, expanded in culture, coaxed into a specific cell type, and then transplanted back into the patient. However, adult stem cells generally do not divide quickly *in vitro,* and they are often hard to obtain and usually cannot be passaged indefinitely. These factors plus their limited potency make adult stem cells less attractive than pluripotent stem cells (PSC) for use in research. As a consequence, most differentiation and toxicological studies involving stem cells are currently being done with embryonic stem cells (ESC), which are derived from preimplantation embryos, or with induced pluripotent stem cells (iPSC), which are derived by reprogramming differentiated adult cells.

Pluripotent Stem Cells

ESC: ESC are especially attractive candidates for toxicological/drug testing and therapeutic applications as they are pluripotent, meaning they can develop into any cell type in an embryo, and they can be passaged many times *in vitro.* ESC were first isolated from the inner cell mass of mouse blastocysts in 1981 at the University of California at San Francisco [5] and at the University of Cambridge [6]. These cells provided the first pluripotent stem cells for experimental work that were not isolated from a tumor. For the next 20 years, they were used extensively in research laboratories to study differentiation and to create knock-out mice.

Human ESC (hESC) were derived in 1998 [7], 16 years after the first mouse ESC (mESC) lines were reported. hESC are generally derived from spare blastocysts offered for research purposes by patients undergoing *in vitro* fertilization. To isolate a line of hESC, blastocysts are usually plated on a feeder layer of mouse embryonic fibroblasts and the inner cell mass (ICM) is mechanically removed and allowed to grow or alternatively the trophoblast is removed using antibodies that lyse it,

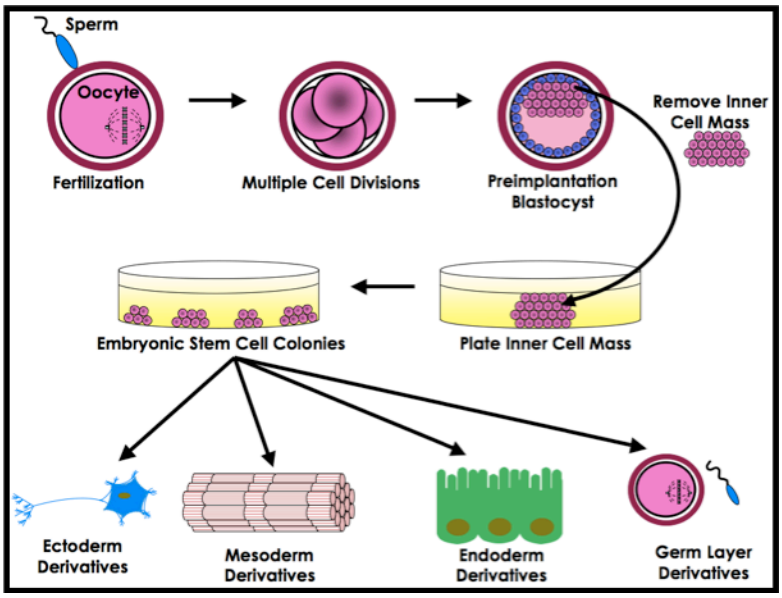

Figure 1.1: Diagram showing the relationship between human embryonic stem cells and human preimplantation embryos. Human embryonic stem cells, which are derived from the inner cell mass of preimplantation embryos, are the best model currently available for studying the pre and post-implantation stage of human development. [8]

leaving just the inner cell mass which can develop into hESC [9,10] (Fig. 1.1). Five hESC lines (H1, H7, H9, H13, and H14) originating from five separate embryos were derived by Dr. Thomson's lab at the University of Wisconsin in 1998 [7] and are currently registered with NIH. Three cell lines (H1, H13, and H14) had normal XY karyotype, and two lines (H7 and H9) had normal XX karyotype. While all of these lines are used in research labs, the H9 line has become the "gold standard" and is the most widely studied, the best characterized, and the line used in this dissertation. Before using these hESC lines, several tests were done to establish their self-renewal capability and pluripotency. Telomerase expression is highly correlated with cell immortality. Telomerase, which is a ribonucleoprotein that adds telomere repeats to the chromosome ends and helps maintain telomere length, is highly expressed in ESC. These hESC lines also have cell surface markers characteristic of undifferentiated pluripotent cells, including stage-specific embryonic antigen (SSEA)-3, SSEA-4, TRA-1-60, TRA-1-81, and alkaline phosphatase. [7]. The ESC isolated by Thomason et al (1998) were able to form derivatives of the three germ layers and also produced teratomas after injection into immunodeficient mice. Each injected mouse formed a teratoma, which included endodermal, mesodermal, and ectodermal tissues.

hESC are being widely used in basic research, translational medicine, and clinical applications [11]. hESC provide insights into developmental events that cannot be studied directly in the intact human embryo but that have important consequences in clinical areas, including birth defects and pregnancy loss.

iPSC

iPSC are a newer entry into the pluripotent stem cell research arena. iPSC were first reported in 2006 when Yamanaka's team reprogrammed adult mouse fibroblasts

into embryonic-like cells which were pluripotent [12]. A year later the same lab reported success in creating human iPSC from human dermal fibroblasts [13]. Reprogramming was accomplished by introducing viral vectors carrying the genes for Oct4, Sox-2, Klf4 and Sox2 into fully differentiated cells. After expression of these four genes in differentiated adult cells, a small percentage of cells reverted to a pluripotent state and became similar to ESC. This discovery was considered so significant that Dr. Yamanaka was awarded the Noble Prize in Physiology and Medicine in 2012 [14]. Since the publication of the two seminal papers from Dr. Yamanaka's lab, numerous studies have been reported on iPSC and improved methods for reprogramming have been developed [15]. iPSC hold great promise as they are immunologically identical/similar to the donor and therefore could provide the basis for hundreds of potential therapies that are based on the use and differentiation of pluripotent cells. While, iPSC provide the foundation for an entirely new field of research in cell reprogramming and translational medicine, there is still a fundamental need for better methods of obtaining and culturing iPSC. One purpose of my dissertation is to understand and improve methods for passaging pluripotent cells and reducing stress during culture.

Using pluripotent cells to test the toxicity of drugs and environmental chemicals:

Researchers are developing protocols to differentiate hESC into different cells or tissues with the expectation that these derivatives will eventually be able to cure or treat diseases [16,17]. Much work in the field of stem cell biology has been devoted to this goal. In addition, hESC are also being used to test new drugs and to identify chemicals that may be harmful to embryos [8,18,19].

There are several ways in which stem cells can be used to evaluate chemical toxicity (Fig. 1.2). First, chemicals can be added directly to undifferentiated ESC and their effects can be evaluated on endpoints such as maintenance of pluripotency, proliferation, apoptosis, survival, migration and growth. The endpoints can be evaluated using morphological or molecular changes and tell something about potential harmful effects that test regents may have on early stage preimplantation embryos. Secondly, ESC can be cultured in media supporting differentiation. This is often done by first making embryoid bodies and then allowing the embryoid bodies to further differentiate into a particular cell type or differentiate spontaneously. Test chemicals can be added

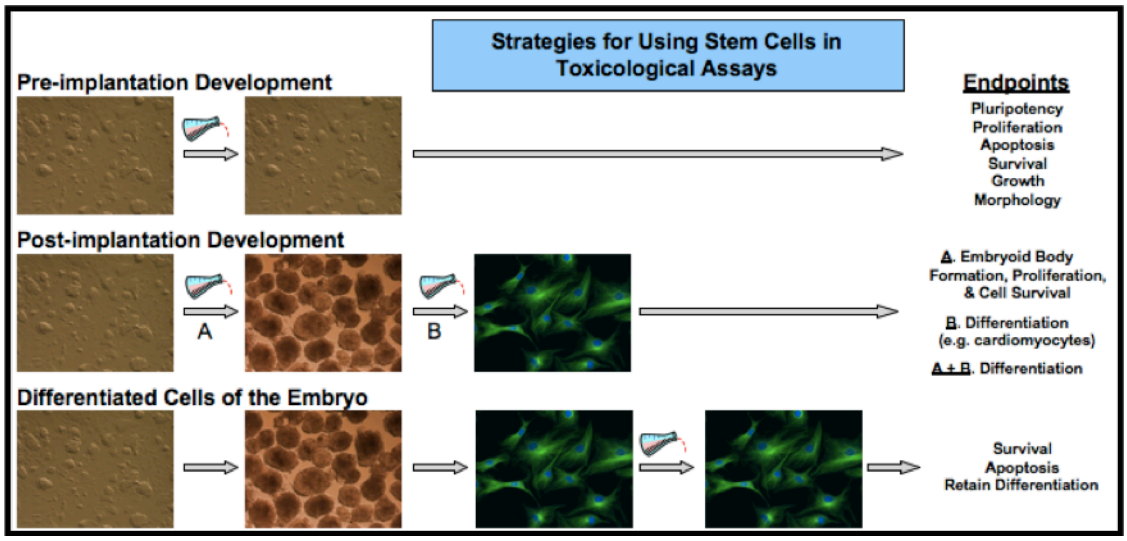

Figure 1.2: Diagram showing various strategies for using embryonic stem cells in toxicological studies. [8]

either before or after embryoid body formation. This strategy can be used to determine how chemicals affect the process of differentiation. Finally, chemicals can be added to the differentiated cells and their effects studied. The first approach identifies chemical that are embryotoxic, while the latter two approaches can identify teratogens.

Our lab has an interest in identifying environmental chemicals that adversely affect prenatal stages of human development [19]. hESC provide a uniquely powerful

technology to perform experiments that could never be done on pregnant women. Currently such experimental work is hampered by a lack of proper culture conditions. For example, during passaging, hESC must be plated as small colonies rather than single cells. This makes it difficult to quantify the number of cell being plated per well, which is necessary to perform dose response type experiments and toxicological screens. Secondly, plating efficiency is not very good, which also hinders the development of stem cell technology. Finally drugs such as the ROCK inhibitor, Y27632, which are often used to facilitate plating, may themselves have toxic effects and mask results of other toxicants [20]. Therefore, one of my goals has been to improve the passaging of single hESC and plating efficiency and to open up more research opportunities with improvement of cell culture methodology.

Visualization of hESC

Phase contrast optics: hESC are small cells that are hard to visualize with a light microscope. Phase contrast microscopy is an optical technique that is especially well suited for hESC visualization. Phase contrast microscopy can be used to resolve hESC and structures within hESC that are not visible with brightfield and other forms of light microscopy. Phase contrast microscopy, unlike interference microscopy, is also compatible with the plastic culture dishes used for culturing hESC.

Time lapse videos: Live cell imaging has been widely used in cell biology and has recently been applied to toxicological problems [19,21,22,23,24,25,26,27,28,29,30]. A number of instruments are currently marketed for collecting time-lapse videos, and the instrumentation in this field has improved enormously in the last 10 years [30]. The

BioStation IM and its newer version the BioStation IM-Q, manufactured by Nikon, are bench top instruments that house a motorized inverted microscope, an incubator with a built-in high sensitivity cooled CCD camera, and software for controlling exposures, objectives, and the type of imaging (e.g., phase contrast or fluorescence) (Fig. 1.3). The components of this instrument are fully integrated and easy to set up. In a BioStation IM, cells are easily maintained at a constant temperature (37^{o}C) and relative humidity (85%)

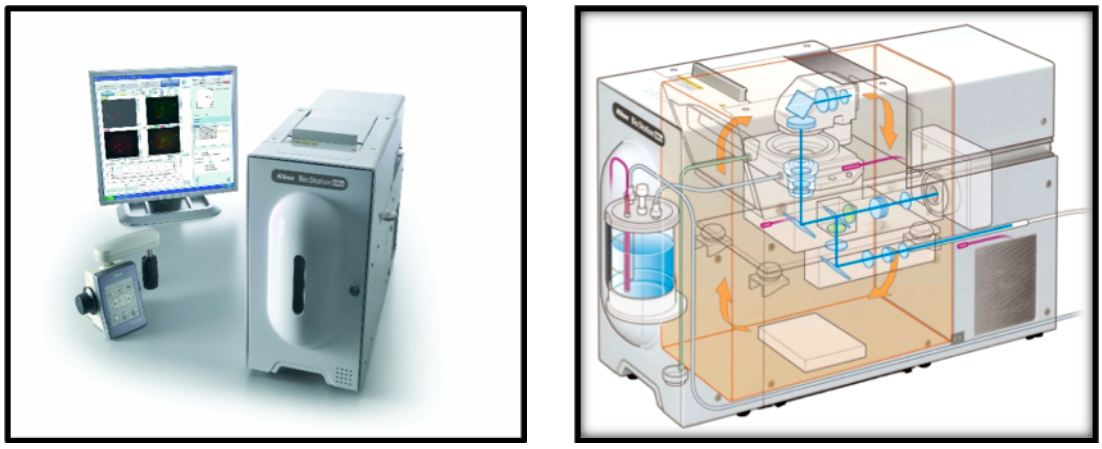

Figure 1.3: The BioStation IM, which is manufactured by Nikon, is a bench top instrument that house a motorized inverted microscope, an incubator with a built-in high sensitivity cooled CCD camera, and software for controlling exposures, objectives, and the type of imaging. [30]

in a 5% CO_2 atmosphere. The BioStation IM enables time-lapse data to be collected reliably over hours or days without focus or image drift. In time-lapse experiments, images can be collected as quickly as 12 frames/second. In a BioStation IM, imaging can be also performed in the X, Y and Z-direction. The unit comes with a well-designed software package and a GUI for controlling the instrument and all experimental parameters. The BioStation IM was used extensively in this dissertation to analyze the dynamic behavior of hESC during passaging.

ESC Culturing

Initially, researchers used mouse embryonic fibroblasts (mEF) as feeder cells to provide growth factors that help ESCs maintain their undifferentiated state and self-renew [5,6,8]. In mouse ESC cultures, the feeder layer can be replaced by addition of leukemia inhibitory factor (LIF) to the growth medium [31]. The importance of the LIF-pathway in derivation and maintenance of ESCs has been studied. In mouse ESC, LIF activates the STAT3-mediated cascade, and also induces the PI3K-pathway, which is involved in the maintenance of pluripotency [31].

In contrast to mESC, LIF does not maintain pluripotency in hESCs. This is because hESC represent a slightly later stage in embryonic development that is not responsive to LIF. Although hESC are isolated from the inner cell mass of blastocysts, once grown in culture they more closely resemble the epiblast cells of early post-implantation embryos [9,32,33]. At first, hESC culture protocols involved the use of mEF as substrates and media containing serum and animal proteins. However, the feeder layers add complexity to stem cell cultures and have the potential to introduce animal viruses and unwanted effects into the stem cell population, especially when using mouse fibroblasts for hESC culture. Newer protocols have been developed using human fibroblasts as feeder layers and using human serum instead of animal serum [35]. In 2001, the first feeder-free hESC culture system was introduced using different matrices, such as Matrigel and laminin, with medium that was conditioned by mouse embryonic fibroblasts [36].

However, using non-human elements in hESC culture is an obstacle to later clinical use of these cells. Many groups have worked on developing new protocols that use non-human components for culturing hESC. An alternative strategy was to use

serum-free media supplemented with soluble factors (e.g., basic fibroblast growth factor and noggin) [37]. However, there was still a need to develop a well-established feeder-free hESC culture system. A major improvement in hESC culture was introduced in 2001 when hESC were plated on BD Matrigel and fed with mTeSR medium, which is a fully-defined, serum-free medium for the derivation and maintenance of hESC [38,39]. mTeSR has been tested successfully on different human ESC lines, such as H1 and H9 (STEMCELL Technologies, BV, Canada), and it can support the culture of undifferentiated hESC. Many laboratories currently working with hESC are using mTeSR and Matrigel for feeder-free hESC culture.

Additional media for feeder-free culture are still being developed. A newer medium for hESC culture is TeSR-E8 which is xeno-free and contains only the 8 essential components in contrast to mTeSR1, which has more than 60 components in supplement (STEMCELL Technologies, BV, Canada). Like mTeSR1, TeSR E8 is made for feeder-free culture for hESC. In addition, TeSR 2 has recently been developed as an improved version of mTeSR1, and provides a high-quality and robust system for feeder-free maintenance of pluripotent stem cells. TeSR2 combines the advantages of a feeder-free culture system with the added value of being free of xenogenic components (STEMCELL Technologies, BV, Canada). Both TeSR-E8 and TeSR 2 can be used with different matrices such as Matrigel and vitronectin-XF. In recent years, a number of new culture media have been introduced that compete with the mTeSR products. For example, PluriQ medium, which has standard formulation for culturing human pluripotent ES and iPS cell line, is made by MTI-GlobalStem (BioCompare, CA); human embryonic stem cell growth medium, which is from Cygen, is also developed for culturing undifferentiated pluripotent stem cells. because many of the new media have been

introduced in the last year or two, few comparisons have been made with the TeSR line of products.

hESC normally require adhesion to an extracellular matrix for growth and survival, and different matrices are used for feeder-free hESC culture system. Matrigel, which contains mostly laminin, collagen IC and heparin sulfate proteoglycan is isolated from Engelbreth-Holm-Swarm mouse sarcomas, a tumor rich in ECM proteins, and is widely used with mTeSR medium [36]. There are other matrices that have been developed for hESC culture, such as Vitronectin XF, Geltrex, and Laminin-521. hESC express a1 a5, b1, b2 and r1 laminin chains [40,41], which may combine to form four different laminin isoforms (e.g., LN-511, LN-521, LN-111 and LN-121). Matrigel, which is widely used for hESC culture, contains a large amount of LN-111. Laminin-521 is the natural laminin for pluripotent stem cells and therefore reliably facilitates self-renewal of hESC and iPSC in a chemically defined feeder-free stem cell culture system. The advantage of using laminin-511 and laminin-521 is that a5 chain laminins are found in stem cell niches of blastocysts (inner cell mass) [42]. One goal of my research has been to determine if any particular substrate facilitates cell attachment, spearding, and plating efficiency during passaging of cells.

Problems with Passaging Pluripotent Stem Cells: hESC are social cells that require co-operative interactions and intimate physical contact with each other to maintain their viability and self-renewal capacity during cell culture. During passaging, it is usually necessary to dissociate hESC colonies into cellular clumps rather than into a single-cell suspension, since a high degree of cell death is correlated with a loss of cell-to-cell interactions. This makes hESC harder to culture than other cell types. Moreover, it is

also difficult for researchers to plate the same cell number every time when doing drug testing or toxicological experiments. Controlling cell number for certain experiments is extremely important. Therefore, the Rho-associated coiled-coil kinase (ROCK) inhibitor (ROCKi) is often used to help cells attach and to enable passaging of single cells. ROCKi can increase the efficiency of hESC survival in culture [43]. Several groups have addressed the mechanism by which ROCKi prevents cell dissociation-induced apoptosis, and found that ROCKi does not inhibit apoptosis directly but inhibits ROCK-dependent myosin II hyperactivation [43,44,45]. It has been demonstrated that myosin II is the predominant effector molecule downstream of Rho-Rock signaling in the regulation of cell-cell contracts in ESC [46]. Blebbistatin, which is an inhibitor of myosin II, can also be used to increase single cell survival during hESC culture and aid in attachment.

However, ROCK is involved in numerous signaling pathways and may affect many cell properties, not just attachment and spreading. In our lab, when we plate single hESC with ROCKi, which helps hESC attachment and survival, cells appear stressed and abnormal (Fig. 1.4) [47]. Both our lab and Dr. Fujumura's lab [20,47] also found that ROCKi alters the cell responses in toxicological experiments, again suggesting it is not suitable for inclusion in many types of experiments. To avoid this problem, it is important to find other ways to increase hESC plating

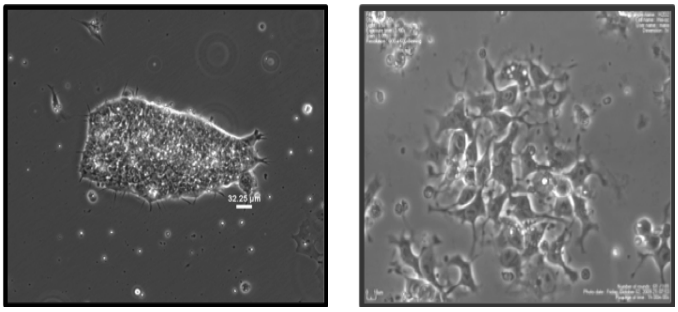

Figure 1.4: hESC, were plated with ROCKi, appear stressed and abnormal morphology. A: control hESC colony; B: ROCKi-Treated hESCs

efficiency and survival and to enhance cell attachment during normal passaging or when single hESC plating is necessary.

Dynamic and Apoptotic Blebbing

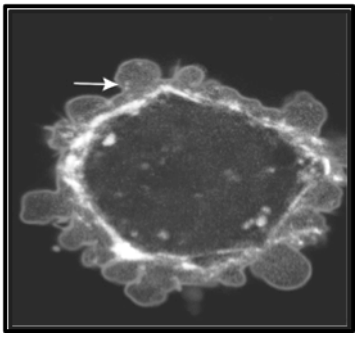

Figure 1.5: Blebs were produced in HeLa cell.

Overview: Blebs are membrane protrusions that appear and disappear from the surface of cells (Fig. 1.5) [48,49,50]. In most eukaryotic cells, the plasma membrane is bound to cortical actin. When the plasma membrane separates from the actin, cytoplasmic pressure leads to formation of blebs around the cell surface [48]. Blebbing is characteristic of the execution phase of apoptosis; however, blebs are also observed in healthy cells, for example during cytokinesis and cell migration [50,51,52]. A mechanism of blebbing has been proposed based on work done with non-hESC cell types [53,54,55]. The model subdivided blebbing into three phases: nucleation, expansion, and retraction [54,55]. During nucleation, blebs begin to form when small areas of the plasma membrane detach from cortical actin or when a local rupture of the cortical actin occurs. Once a bleb is nucleated, hydrostatic pressure in the cytoplasm drives bleb expansion causing cytosol to flow into the developing bleb [54,55]. Concomitantly, the plasma membrane detaches further from the cortex, increasing bleb size. As bleb expansion slows down, a new actin cortex reforms under the bleb membrane. Finally, the motor protein myosin II is recruited to the bleb and powers retraction (Fig. 1.6).

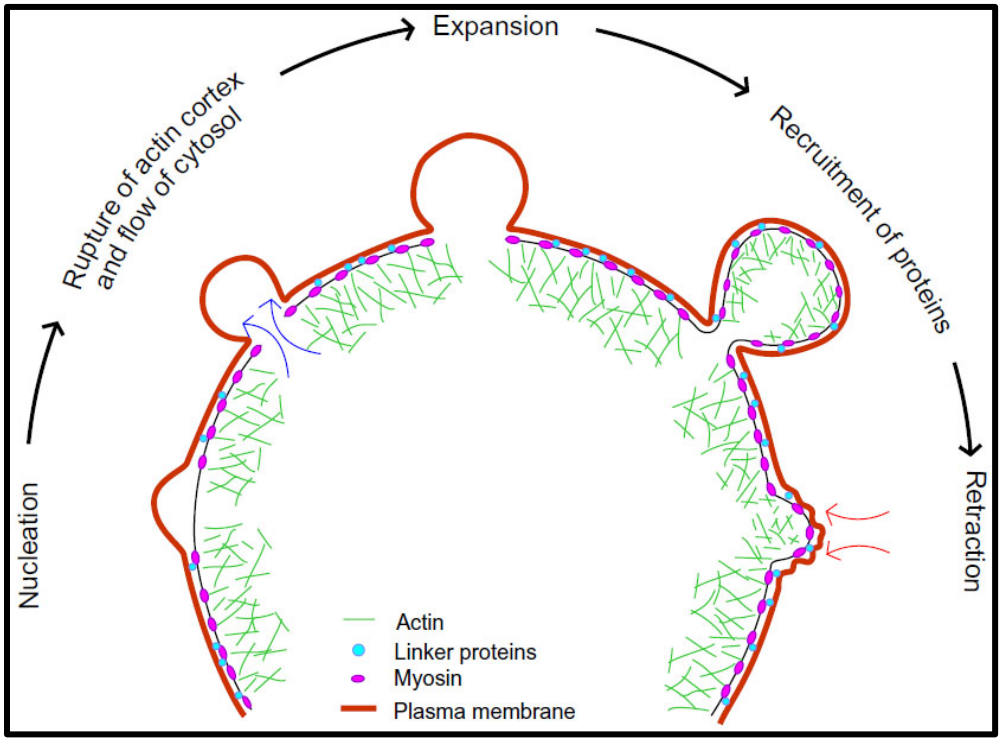

Figure 1.6: The mechanism of Blebs formation and retraction. [55]

Apoptotic Blebbing: Apoptotic blebbing has been studied in detail and is the more commonly reported example of blebbing. Apoptotic blebs contain a cortical layer of endoplasmic reticulum that often surrounds condensed chromatin. Dr. Woodman's group suggested in 2005 that microtubule motors are needed to transport endoplasmic reticulum and chromatin along microtubules and into apoptotic blebs [56]. They examined whether inclusion of endoplasmic reticulum in apoptotic blebs was sensitive to the microtubule destabilizing agent nocodazole. Surprisingly in this experiment, nocodazole markedly reduced the proportion of apoptotic cells with blebs, suggesting that apoptotic bleb formation itself is microtubule as well as actin-dependent. In the

absence of microtubules, about 50% of cells still formed apoptotic blebs that contained endoplasmic reticulum, suggesting that microtubule motors do not provide the sole means of transporting endoplasmic reticulum into blebs. It is possible that other cytoskeletal proteins drive this relocation as well [56]. This study also speculated that the lack of microtubules, which releases pressure inside the cytoplasm, might prevent the initiation of apoptotic blebbing in some cells [56]. Moreover, apoptotic bleb formation depends on actin-myosin contraction which results from the activation of myosin light chain [55, 57,58,59,60] via phosphorylation indirectly or directly by Rho-activated kinase, which in turn is cleaved into a constitutively active form by caspases in 3T3 cells and hematopoietic cell lines [61,62].

Blebbing, which is usually characterized as apoptotic, has been reported in hESC [63]. In 2010, Dr. Sasai's group showed that dissociated single hESC formed a number of blebs on their surfaces. Blebbing began immediately when colonies were dissociated into single cells and continued until cells formed apoptotic bodies; however, mESC are easy to culture and they can survive even were passaged as single cells. Two major questions regarding this problem have been raised: Why are hESC, unlike mESC, vulnerable to dissociation? And how can the death of dissociated hESC be prevented? A number of recent studies have been shown that there are multiple metastable states of pluripotency. After implantation, the ICM differentiates into two distinct cell lineages, the primitive endoderm and the epiblast. Recently, researchers recognized that there are at least two distinct types of pluripotent stem cells, the ICM-like and the epiblast-like stem cells [34,64,65,66]. mESC are more ICM-like while hESC are epiblast-like [34]. By switching culture conditions, these two states can be interconverted. When mESC are converted to mouse epilbast-like stem cells (mEpiSC), mEpiSC are similar to hESC, in

their behavior, colony morphology, growth-factor responses, and gene expressions. Moreover, mEpiSC show vulnerability to cellular dissociation, like hESC [34].

Blebbing in hESC differs qualitatively from the conventional apoptotic blebbing. In other cell types, blebbing is the terminal phase of apoptosis; however, hESC blebbing appears immediately after dissociation. Moreover, the blebbing is ROCK-dependent but not caspase-dependent even though the onset of blebbing precedes caspase activation [34,63,67].

In 2010, Dr. Sasai's group demonstrated that the ROCK-dependent hyperactivation of myosin is the direct cause of blebbing in hESC and showed that blebbing is caused by Rho/ROCK/MLC2 activation. They interpreted the blebbing to be apoptotic since ROCK treated cells attached to the substrate and survived [63], while those that were not treated failed to attach and died. ROCK inhibitor (ROCKi) has been widely used to increase the survival rate of hESC by inhibiting apoptosis during plating of cells [43,46,63,68].

Functional imaging analysis showed that Rho activation occurs, and other studies showed that Rac activity gradually decreases very early after hESC dissociation [34,63], indicating that Rho/Rac might play an important role in regulating blebbing during hESC dissociation and culture. However, the upstream regulation of the Rho/Rac pathways in dissociated hESC is not clear.

Dynamic blebbing: Dynamic blebbing, which is observed in healthy cells, often occurs in *vitro* during the first minutes after cell plating and before cell attachment and spreading on adherent substrates. Dynamic blebs are also found at the leading edge of migrating cells, where they drive cell movement [69]. Polarized blebbing is used to

generate motility in a number of cell types such as Dictyostelium, Fundulus deep cells, zebrafish germ cells, neutrophils, and tumor cells (54). Dynamic blebbing is also a normal process during cytokinesis, when blebs appear at the poles of dividing cells (50,54,70,71,72,73].

The mechanism regulating dynamic bleb formation is similar to apoptotic blebbing. There is a growing body of evidence that ROCK is involved in regulating the cytoskeleton during blebbing [55,74,75]. ROCK is one of the major downstream mediators of Rho. The GTP-bound form of Rho interacts with ROCK, inducing a conformational change in ROCK that elevates its kinase activity. This allows ROCK to inactivate myosin light chain phosphatase, thus maintaining myosin light chain in an active form. The active myosin can react with actin and drive actin filament movement. In 2007, dynamic blebbing was observed in calvarial cells from wild type, but not P2X7 knock-out mice, indicating the P2X7 receptor might regulate dynamic blebbing upstream of Rho pathway [76].

In dissociated hESC, dynamic and apoptotic blebbing have not previously been clearly distinguished [63,77,78]. Moreover, it is not clear from the Sasai et al study if dynamic or apoptotic blebbing or both were affected by ROCKi. It is also unclear what regulates dynamic blebbing upstream of Rho. In Dr. Sasai's paper, RNA interference was used to demonstrate that Active BCR-Related (Abr), a unique Rho-GEF family factor containing a functional GAP domain for Rho-class GTPase, is an upstream regulator of apoptosis and ROCK-myosin hyperactivation. It is not clear if Abr is the only upstream factor and other studies in the literature suggest multiple pathways may converge on Rho in other cell types [76,79].

Functions of dynamic blebbing in non-hESC and hESC: The function of dynamic blebbing has recently been appreciated [80,81]. Blebs are commonly observed during cell division, from the onset of anaphase until late cytokinesis [50,81,82]. Blebbing, during cytokinesis, might be a mere side-effect of tension build-up in the cortex during cell division, as it has been reported that increased tension can directly result in bleb formation [57,83,84,85]. Alternatively, blebs might represent a rapid way of generating additional cortex or membrane surface area during cytokinesis and subsequent cell spreading. Dynamic blebbing has been shown experimentally to facilitate cell movement during embryonic development in amphibian and fish embryos [86,87,88,89]. Cells dissociated from amphibian embryos can migrate using bleb-like protrusions [90,91,92]. Studies in live zebrafish have unequivocally shown that primordial germ cells use blebs to migrate [86].

Similar observations have been made in primordial germ cells from Drosophila melanogaster embryos [93]. These findings suggest that dynamic blebbing may be widely used for cell migration and further hint that dynamic blebbing may be a common mechanism for generating motility in embryonic cells.

When cultured in vitro, hESC behave like epiblast cells, a highly motile epithelialized type of embryonic cell [34]. During weeks 2 and 3 of human development, epiblast cells form a single layer of tall columnar cells that undergo extensive migration to give rise to the three germ layers of the embryo. During gastrulation, the epiblast cells move as a sheet medially and enter the primitive streak. At the base of the primitive groove, epiblast cells pinch off of the primitive groove, undergo an epithelial to mesenchymal transition, and migrate as single cells to form both the endoderm and mesoderm. During both types of migration (as sheets and as onio 1995 cell

processessingle cells), epiblast and mesenchymal cells are highly motile. Some studies have hypothesized that hyperactivity of the ROCK/myosin system enables the epiblast-stage cells to undergo rapid cell movement [63]. Recently, more evidence has shown that dynamic blebbing has an important role in cell motility. Regulating blebbing is crucial and needed for controlling hESC that will be used in clinically in stem cell therapy.

Use of blebbing and cell spreading as toxicological/cell health endpoints

Cell health validation: Live cell imaging has been widely used in our laboratory for many years to study dynamic cell processes [94,95,96,97,98] and has more recently been applied to toxicological problems [19,21,22,23,24,25,26,27,28,29,30,99]. In toxicological assays using stem cells, endpoints of interest often occur days or sometimes a month after the experiment begins [19,30,100]. There has been interest in shortening such assays, often by using molecular biomarkers to obtain endpoints more rapidly [101]. In the mouse embryonic stem cells test, endpoints can now be obtained in 7 days using biomarkers for heart development [101,102]. While this significantly reduces the time to reach an endpoint, it is still a relatively long time to obtain data on cytotoxicity. Nowadays, analysis of dynamic events, such as cell attachment, migration, division, and apoptosis, provides mechanistic insight into normal cellular processes and has been widely used in ESC research [19,30] and toxicological research (21,94,103,104].

Changes in cell behavior that depend on the cytoskeleton often indicate that cell health is being compromised by environmental conditions [19,103]. Because spreading depends on the cytoskeleton, it can be used to evaluate the effect of chemical treatments on cytoskeletal health. Cell spreading is a particularly attractive endpoint in

toxicological studies as it occurs soon after plating and does not require days or weeks of treatment to observe. Many types of cells, such as fibroblasts can attach and spread in 10-15 minutes. hESC require about 1– 2 hours to spread. Therefore, cells can be plated and data collected in 4 hours or less time depending on the experimental design.

Summary

This dissertation deals specifically with dynamic blebbing, which is robust in hESC. Dynamic blebbing, which is observed in healthy cells, often occurs in *vitro* during the first minutes after cell plating and before cell attachment and spreading on adherent substrates. Dynamic blebs are also found at the leading edge of migrating cells, where they drive cell movement. The difference between dynamic and apoptotic blebbing has not previously been distinguished in hESC. It is widely known that hESC are not easy to culture. Recently, most studies have improved hESC culture by using ROCKi. However, ROCK is involved in numerous signaling pathways and may affect many cell properties, not just attachment and spreading. In our lab, when we plate single hESC with ROCKi, which helps hESC attachment and survival, cells appear stressed and abnormal. The purposes of my dissertation were to: (1) characterize dynamic and apoptotic blebbing in hESC, (2) identify the signaling pathway that activates dynamic blebbing during passaging of hESC, (3) identify methods that reduce dynamic blebbing once it has started, and (4) identify targets that will enable further development of strategies to regulate blebbing and thereby improve hESC culture and all hESC applications.

Scope of Dissertation

Chapter 2 describes a video bioinformatics protocol that was developed to quantify cell spreading and hESC health during culture.

Chapter 3 distinguishes between apoptotic and dynamic blebbing in hESC. This chapter compares the morphology, formation, retraction, and molecular markers in dynamic and apoptotic blebbing. Methods that halt dynamic blebbing during passaging were identified, and these will enable further development of strategies to regulate blebbing during passaging, thereby leading to improved culture protocols that will be suitable for all hESC applications.

The focus of Chapter 4 is to identify the pathways that are involved in initiating dynamic blebbing in hESC. This chapter provides new insight into factors that increase dynamic blebbing, such as release of ATP from cells that die during passaging and identities new targets, such as the P2X7 receptor, that could be used to decrease dynamic blebbing and improve cell attachment and survival. These results may lead to better ways to control dynamic blebbing in cultured hESC and further show that hESC are an excellent model for studying blebbing and its role in early embryonic development.

Chapter 5 summarizes the key findings of this project.

References

1. Young HE, Black AC Jr. Adult stem cells. Ant Rec Part A Discov Mol Cell Evol Biol 2004:276(1):75-102.
2. NIH- What are adult stem cells?. In Stem Cell Information [World Wide Web site]. Bethesda, MD: National Institutes of Health, U.S. Department of Health and Human Services, 2015
3. Orth P, Rey-Rico Ana, Venkatesan JK, et al., Current perspectives in stem cell research for knee cartilage repair. Stem Cell Cloning. 2014:7:1-17.
4. Turner L, Knoepfler P. Selling Stem Cells in the USA: Assessing the Direct-to-Consumer Industry. Cell Stem Cell. 2016:S1934-5909(16)30157-6.
5. Martin GR. Isolation of a pluripotent cell line from early mouse embryos cultured in medium conditioned by teratocarcinoma stem cells. Proc. Natl Acad. Sci. USA. 1981;78:7634–7638.
6. Evans MJ, Kaufman MH. Establishment in culture of pluripotent cells from mouse embryos. Nature 1981;292:154–156.
7. Thomson JA, Itskovitz-Eldor J, Shapiro SS, et al. Embryonic stem cell lines derived from human blastocysts. Science 1998;282:1145–1147.
8. Talbot P, Lin S. Mouse and human embryonic stem cell: can they improve human health by preventing disease? Current Topics in Medicinal Chemistry. 2011:11:14:1638-52.
9. Smith KP, Luong MX, Stein GS. Pluripotency: toward a gold standard for human ES and iPS cells. J Cell Physiol 2009**:**220:21-29.
10. Stahlberg A, Bengtsson M, Hemberg M, et al. Quantitative Transcription Factor Analysis of Undifferentiated Single Human Embryonic Stem Cells. Clin Chem 2009:55(12):2162-2170
11. Shroff G, Gupta A, Barthakur JK. Therapeutic potential of human embryonic stem cell transplantation in patients with cerebral palsy. J Transl Med. 2014:12:318
12. Takahashi K, Tamanaka S. Induction of pluripotent stem cells from mouse embryonic and adult fibroblast cultures by defined factors. Cell. 2006:126(4):663-676.
13. Takahashi K, Tanabe K, Ohnuki M, et al., Induction of pluripotent stem cells from adult human fibroblasts by defined factors. Cell. 2007:131(5):861-872.
14. Nobel prize – The Nobel Prize in Physiology or Medicine 2012". Nobelprize.org. Nobel Media AB 2014. Web. 16 Jul 2016. <http://www.nobelprize.org/nobel_prizes/medicine/laureates/2012/>

15. Malik N, Rao MS. A review of method for human iPSC derivation. Methods Mol Biol. 2013:997:23-33.

16. Arno A, Smith AH, Blit PH, et al., Stem cell therapy: a new treatment for burns? Pharmaceuticals. 2011:4:1355-1380.

17. Moretti A, Laugwitz KL, Dorn T, et al., Pluropotent stem cell models of human heart disease. Cold Spring Harb Perspect Med. 2013::11:a014027.

18. Krtolica A, Ilic D, Genbacev O, et al. Human embryonic stem cells as a model for embryotoxicity screening. Regenerative Medicine. 2009:4:3:449-459.

19. Lin S, Fonteno S, Weng JH, et al., Comparison of the toxicity of smoke from conventional and harm reduction cigarettes using human embryonic stem cells. Toxicol Sci. 2010:39:1833.

20. Fujimura M, Usuki F, Kawamura M, et al. Inhibition of the RHO/ROCK pathway prevents neuronal degeneration in vitro and in vivo following methylmercury exposure. Toxicol Appl Phamacol 2011:250(1):1-9.

21. Knoll M, Shaoulian R, Magers T, et al. Ciliary beat frequency of hamster oviducts is decreased in vitro by exposure to solutions of mainstream and sidestream cigarette smoke. Biol Reprod. 1995:53(1):29-37.

22. Knoll M, Talbot P. Cigarette smoke inhibits oocyte cumulus complex pick-up by the oviduct in vitro independent of ciliary beat frequency. Reprod Toxicol. 1998:12(1):57-68.

23. Talbot P., DiCarlantonio G., Knoll M., and Gomez C. Identification of cigarette smoke components that alter functioning of hamster (Mesocricetus auratus) oviducts in vitro. Biology of Reproduction, 1998:58(4)1047-1053

24. DiCarlantonio G, Talbot P. Inhalation of mainstream and sidestream cigarette smoke retards embryo transport and slows muscle contraction in oviducts of hamsters (Mesocricetus auratus). Biol Reprod. 1999:61(3):651-656.

25. Riveles K, Iv M, Arey J, et al. Pyridines in cigarette smoke inhibit hamster oviductal functioning in picomolar doses. Reproductive Toxicology, 2003:17(2):191-202.

26. Riveles K, Roza R, Arey J, et al. (2004) Pyrazine derivatives in cigarette smoke inhibit hamster oviductal functioning. Reprod Biol Endocrinol. 2004:2(1):23.

27. Riveles K, Roza R, Talbot P. Phenols, quinolines, indoles, benzene, and 2-cyclopenten-1-ones are oviductal toxicants in cigarette smoke. Toxicol Sci. 2005:86(1):141-151.

28. Riveles K, Tran V, Roza R, et al. Smoke from traditional commercial, harm reduction and research brand cigarettes impairs oviductal functioning in hamsters (Mesocricetus auratus) in vitro. Human Reprod. 2007:22(2):346-355.

29. Gieseke C, Talbot P. Cigarette smoke inhibits hamster oocyte pickup by increasing adhesion between the oocyte cumulus complex and oviductal cilia. Biol Reprod. 2005:73(3):443-451

30. Talbot P, zur Nieden N, Lin S, et al. Use of video bioinformatics tools in stem cell toxicology. Handbook of Nanomedicine, Nanotoxicology and Stem Cell Use in Toxicology. John Wiley & Sons, Ltd, Chichester, UK. 2014:ch21.

31. Ying QL, Nichols J, Chambers I, et al., BMP induction of Id proteins suppresses differentiation and sustains embryonic stem cell self-renewal in collaboration with STAT3. Cell. 2003:115(3):281-292.

32. Pelton TA, Sharma S, Schulz TC, et al., Transient pluripotent cell populations during primitive ectoderm formation: correlation of in vivo and in vitro pluripotent cell development. J Cell Sci. 2002:115:329-339.

33. Surani MA, Hayashi K, Hajkova P. Genetic and epigenetic regulators of pluripotency. Cell. 2007:128(4):747-762

34. Ohgushi M, Sasai Y. Lonely death dance of human pluripotent stem cells: ROCKing between metastable cell states. Trends Cell Biol. 2011:(5):274-282

35. Meng MJ, Li TL, Li CY, et al. A suspended cell line from *Trichoplusia ni* (Lepidoptera): Characterization and expression of recombinant proteins. Insect Sci. 2008;15:423–428.

36. Xu C, Inokuma MS, Denham J, et al, Feeder-free growth of undifferentiated human embryonic stem cells, Nat Biotechnol, 2001:19:971.

37. Lannon C, Moody J, King D, et al. A defined, feeder-independent medium for human embryonic stem cell core. Cell Research. 2008:18:s34.

38. Ludwig TE, Levenstein ME, Jones JM, et al. Derivation of human embryonic stem cells in defined conditions. Nat Biotechnol 2006a:24(2):185-187.

39. Ludwig TE, Bergendahl V, Levenstein ME, et al. Feeder-independent culture of human embryonic stem cells. Nat Methods 2006b:3(8):627-646.

40. Rhodin S, Domogatskaya A, Strom S, et al. Long-term self-renewal of human pluripotent stem cells on human recombinant laminin-511. Nat Biotechnol. 2010:28(6)611-615.

41. Miyazaki T, Futaki S, Hasegawa K, et al. Recombinant human laminin isoforms can support the undifferentiated growth of human embryonic stem cells. Biochem Biophys Res Commun. 2008:375(1):27-32.

42. Klaffky E, Williams R, Yao CC, et al. Trophoblast-specific expression and function of the integrin alpha 7 subunit in the peri-implantation mouse embryo. Dev. Biol. 2001:239:161–175.

43. Watanabe K, Ueno M, Kamiya D, et al. A ROCK inhibitor permits survival of dissociated human embryonic stem cells. Nat. Biotechnol. 2007:25:681–686.

44. Chen G, Hou Z, Gulbranson, DR, et al. Actin-myosin contractility is responsible for the reduced viability of dissociated human embryonic stem cells. Cell Stem Cell 2010:7:240–248.

45. Chen KG, Mallon BS, Mckey RDG, et al., Human pluripotent stem cell culture: consideration for maintenance, expansion, and therapeutics. Cell Stem Cell. 2014:14(1):13-26.

46. Harb N, Archer TK, Sato N. The Rho-ROCK-Myosin signaling axis determines cell-cell integrity of self-renewing pluripotent stem cells. PLOS One 2008:3(8):e3001.

47. Weng NJH, Phandthong R, Talbot P. A video bioinformatics method to quantify cell spreading and its application to cells treated with Rho-associated protein kinase and blebbistatin. Video Bioinformatics Editors B. Bhanu and P. Talbot. Springer, 2015:ch8:151-166.

48. Charras GT. A short history of blebbing. J Microsc, 2008:231:466-478.

49. Sahai E, Marshall CJ. Differing modes of tumour cell invasion have distinct requirements for Rho/ROCK signalling and extracellular proteolysis. Nat Cell Biol. 2003;5(8):711–719.

50. Hickson GRX, Echard A, O'Farrell PH. RHO kinase controls cell shape changes during cytokinesis. Curr Biol. 2006:16(4): 359-370.

51. Tokumitsu T, Maramorosch K. Cytoplasmic protrusions in insect cells during mitosis in vitro. J Cell Biol. 1967:34(2):677-683.

52. Paluch EK, Rac E, et al., The role and regulation of blebs in cell migration. Curr Opin Cell Biol. 2013:5:582-590.

53. Charras GT, Hu CK, Coughlin M, et al. Reassembly of contractile actin cortex in cell blebs. J. Cell. Biol. 2006:175:477-490.

54. Charras GT, Paluch, E. Blebs lead the way: how to migrate without lamellipodia Nat. Rev. Mol. Cell Biol. 2008:9:730-736.

55. Julian L, Olson MF. Apoptotic membrane dynamics in health and disease. Cell Health and Cytoskeleton. 2015:7:133-142.

56. Lane JD, Allan VJ, Woodman PG, et al., Active relocation of chromatin and endoplasmic reticulum into blebs in late apoptotic cells. J Cell Sci. 2005:118(Pt17):4059-4071.

57. Mills JC, Stone NL, Erhardt J, et al., Apoptotic membrane blebbing is regulated by myosin light chain phosphorylation. J Cell Bio. 1998:140(3):627-636.

58. Cunningham CC, Gorlin JB, Kwiatkowski DJ, et al. Actin-binding protein requirement for cortical stability and efficient locomotion. Science. 1992;255(5042):325–327.

59. Cunningham CC. Actin polymerization and intracellular solvent flow in cell surface blebbing. J Cell Biol. 1995;129(6):1589–1599.

60. Tinevez JY, Schulze U, Salbreux G, Roensch J, Joanny JF, Paluch E. Role of cortical tension in bleb growth. *Proc Natl Acad Sci U S A*. 2009;106(44):18581–18586.

61. Coleman ML, Sahai EA, Yeo M, et al. Membrane blebbing during apoptosis results from caspase-mediated activation of ROCK I. Nat Cell Biol. 2001:4:339-345.

62. Sebbagh M, Renvoize C, Hamelin J, et al. (2001) Caspase-3-mediated cleavage of ROCK I induces MLC phosphorylation and apoptotic membrane blebbing. Nat. Cell Biol. 2001:3:346-352.

63. Ohgushi M, Matsumura M, Eiraku M, et al. Molecular pathway and cell state responsible for dissociation-induced apoptosis in human pluripotent stem cells. Cell Stem Cell. 2010:7(2):225-239.

64. Nichols J, Smith A. Naïve and primed pluripotent states. Cell Stem Cell. 2009:6:487-492.

65. Hanna J, Cheng AW, Saha K, et al., Human embryonic stem cells with biological and epigenetic characteristics similar to those of mouse ESCs. Porc Natl Acad Sci USA. 2010:107(20):9222-9227.

66. Buecker C, Geijsen N. Different flavors of pluripotency, molecular mechanisms, and practical implications. Cell Stem Cell. 2010:7(5):559-564.

67. Walker A, Su H, Conti MA, et al. Non-muscle myosin II regulates survival threshold of pluripotent stem cells. Nat Commun. 2010:1:71.

68. Krawetz RJ, Li X, Rancourt DE. Human embryonic stem cell: caught between a ROCK inhibitor and a hard place. BioEssays 2009:31:336-343.

69. Pollard TD, Borisy GG. Cellular motility driven by assembly and disassembly of actin filaments. Cell. 2003*:*1:12:453–465.

70. Boss J. Mitosis in cultures of newt tissues. IV. The cell surface in late anaphase and the movements of ribonucleoprotein. Exp. Cell Res. 1955:8:181–187.

71. Porter K, Prescott D, Frye J. Changes in surface morphology of Chinese hamster ovary cells during the cell cycle. J. Cell Biol. 1973:57:815–836.

72. Fishkind DJ, Cao LG, Wang YL. Microinjection of the catalytic fragment of myosin light chain kinase into dividing cells: effects on mitosis and cytokinesis. J. Cell Biol. 1991:114:967–975.

73. Boucrot E, Kirchhausen T. Endosomal recycling controls plasma membrane area during mitosis. Proc. Natl. Acad. Sci. U.S.A. 2007:104:7939–7944.

74. Maekawa M, Ishizaki T, Boku S, et al. Signaling from Rho to the actin cytoskeleton through protein kinases ROCK and LIM-kinase. Science 1999:285(5429):895-8.

75. Amano M, Nakayama M, Kalbuchi K. Rho-kinase/ROCK: A key regulator of the cytoskeleton and cell polarity. Cytoskeleton(Hoboken) 2010:67(9):545-554

76. Panupinthu N, Zhao L, Possmayer F, et al. P2X7 nucleotide receptors mediate blebbing in osteoblasts through a pathway involving lysophosphatidic acid. J Biol Chem. 2007:282(5):3403-3412.

77. Li L, Bennett SA, Wang L. Role of E-cadherin and other cell adhesion molecules in survival and differentiation of human pluripotent stem cells. Cell Adh Migr. 2012:6(1):59-70.

78. Frisca F, Crombie DE, Dottori M, et al. Rho/ROCK pathway is essential to the expansion, differentiation, and morphological rearrangements of human neural stem/progenitor cells induced by lysophosphatidic acid. J Lipid Res. 2013:54(5):1192-1206.

79. Ratz PH, Miner AS, Barbour SE. Calcium-independent phospholipase A2 participates in KCl-induced calcium sensitization of vascular smooth muscle. Cell Calcium. 2009:46(1):65-72.

80. Fackler OT, Grosse R. Cell motility through plasma membrane blebbing. J. Cell Biol. 2008:181:879-884.

81. de Lucas B, Bernal A, Perez LM, et al. Membrane blebbing is required for mesenchymal precursor migration. PLOS ONE 2016:11(3):e0150004.

82. Strangeways, T. Observations on the changes seen in living cell during growth and division. Proc. R. Soc. Lond., B, Biol. Sci. 1922:94:137-141.

83. Sahai E, Marshall CJ. Differing modes of tumour cell invasion have distinct requirements for Rho/ROCK signaling and extracellular proteolysis. Nat Cell Biol. 2003:5(8):711-719.

84. Paluch E, van der Gucht J, Sykes C. Cracking up: symmetry breaking in cellular systems. J Cell Biol. 2006:175(5)687-692.

85. Tinevez J-Y, Schulze U, Salbreux G, et al. Role of cortical tension in bleb growth. Proc Natl Acad Sci U S A. 2009:106(44):18581-18586.

86. Blaser, H. et al. Migration of zebrafish primordial germ cells: a role for myosin contraction and cytoplasmic flow. Dev. Cell. 2006:11:613-627.

87. Trinkaus, JP. Surface activity and locomotion of Fundulus deep cells during blastula and gastrula stages. Dev. Biol. 1973:30:69-103.

88. Wourms, JP. The developmental biology of annual fishes. II. Naturally occurring dispersion and reaggregation of blastomers during the development of annual fish eggs. J. Exp. Zool. 1972:182:169-200.

89. Trinkaus, JP. Ingression during early gastrulation of Fundulus. Dev. Biol. 1996:177:356-370.

90. Holtfreter, J. Properties and functions of the surface coat in amphibian embryos. J. Exp. Zool. 1943:93:251-323.

91. Kubota KY. Creeping locomotion of the endodermal cells dissociated from gastrulae of the Japanese newt, Cynops pyrrhogaster. Exp. Cell Res. 1981:133:137-148.

92. Satoh N, Kageyama T, Sirakami KT. Motility of siddociated embryonic cells in Xenopus laevis: its significance to morphogenetic movements. Dev. Growth Diff. 1976:18:55-67.

93. Jaglarz MK, and Howard KR. The active migration of Drosophila primordial germ cells. Development. 1995:121:3495-3503.

94. Talbot P. Videotape analysis of hamster ovulation in vitro. J Exp Zool. 1983:225(1):141-148.

95. Howard DR, Talbot P. In vitro contraction of lobster (Homarus) ovarian muscle: methods for assaying contraction and effects of biogenic amines. J Exp Zool, 1992:263(4):356-366.

96. Tsai KL, Talbot P. Video microscopic analysis of ionophore induced acrosome reactions of lobster (Homarus americanus) sperm. Mol Reprod Dev. 1993:36(4):454-461.

97. Dicarlantonio G, Shaoulian R, Knoll M, et al. Analysis of ciliary beat frequencies in hamster oviducal explants. J Exp Zool. 1995:272(2):142-152.

98. Talbot P, Geiske C, Knoll M. Oocyte pickup by the mammalian oviduct. Mol Biol Cell. 1999:10(1):5-8.

99. Gieseke C, Talbot P. Cigarette smoke inhibits hamster oocyte pickup by increasing adhesion between the oocyte cumulus complex and oviductal cilia. Bio Reprod. 2005:73(3):443-451.

100. Genschow E, Splelmann H, Scholz G, et al. Validation of the embryonic stem cell test in the international ECVAM validation study on three in vitro embryotoxicity tests. Altern Lab Anim. 2004:32(3):209-244.

101. Buesen R, Genschow E, Slawik B, et al. Embryonic stem cell test remastered: comparison between the validated EST and the new molecular FACS-EST for assessing developmental toxicity in vitro. Toxicol Sci. 2009:108(2):389-400.

102. Inselman AL, Nolen GT, Chang C-W, et al. Reevaluation of the embryonic stem cell test. J R S. 2013:1:1:32-49

103. Bahl V, Lin S, Xu N, et al. Comparison of electronic cigarette refill fluid cytotoxicity using embryonic and adult models. Reprod Toxicol. 2012:34(4):529-537.

104. Behar RZ, Davis B, Wang Y. et al. Identification of toxicants in cinnamon-flavored electronic cigarette refill fluids. Toxicol In Vitro. 2014:2:198-208.

Chapter 2

A Video Bioinformatics Method to Quantify Cell Spreading and Its Application to Cells Treated with Rho-Associated Protein Kinase and Blebbistatin

Nikki Jo-Hao-Weng, George Phandthong, and Prue Talbot

UCR Stem Cell Center, UCR Stem Cell Core

Cell Biology and Neuroscience Department, Cell, Molecular, Development Biology Program. Integrated Graduate Education Research and Training Program, University of California, Riverside, CA 92521

Corresponding author: Prue Talbot, PhD., Department of Cell Biology & Neuroscience, University of California, Riverside CA. 92521 951-827-3768 phone; 951-827-4207 FAX; talbot@ucr.edu

The authors have no conflicts of interest to acknowledge.

1.1 INTRODUCTION

Live cell imaging has been widely used in our laboratory for many years to study normal dynamic cell processes [1,2,3,4,5,6] and has more recently been applied to toxicological problems [7,8,9,10,11,12,13,14,15,16,17]. Analysis of dynamic events, such as cell attachment, migration, division, and apoptosis, can provide mechanistic insight in to normal cellular processes [18,19] and as well as how toxicants affect cells [1,7,20,21]. Collection of video data has recently improved and become easier to perform with the introduction of commercial incubators that have built in microscopes and cameras for collecting time-lapse data during both short and long-term experiments [19,22,23].

After videos are collected, it is important to extract quantitative data from them. A challenging but important issue until recently has been how to analyze the large complex data sets that are produced during live cell imaging. When video data analyses are done manually by humans, many hours of personnel time are usually required to complete a project, and manual analysis by humans is subject to variation in interpretation and error. Video bioinformatics software can be used to speed the analysis of large data sets collected during video imaging of cells and also can improve the accuracy and repeatability of analyses [19]. Video bioinformatics, which involves the use of computer software to mine specific data from video images, is concerned with the automated processing, analysis, understanding, visualization, and knowledge extracted from microscopic videos. Several free video bioinformatics software packages are available online such as ImageJ and Gradientech Tracking Tool (http://gradientech.se/products/gradientech-tracking-tool/). Also, some advanced video bioinformatics software packages, such as CL-Quant, Imira, and Cell IQ, are now

commercially available and can be used to generate customized protocols or libraries to analyze video data and determine quantitatively how cells behave during experimental conditions.

This chapter presents a new application of CL-Quant software to automatically analyze cell spreading in time-lapse videos of human embryonic stem cells (hESC) (WiCell, Madison, WI). While hESC are presented in this chapter, other cell types could also be used in conjunction with these protocols.

1.2 INSTRUMENTATION USED TO COLLECT LIVE CELL VIDEO DATA

BioStation IM

Data presented in this chapter were collected with a BioStation IM. The BioStation IM or its newer version the IM-Q, manufactured by Nikon, is a bench top instrument that houses a motorized inverted microscope, an incubator with a built-in high sensitivity cooled CCD camera, and software for controlling exposures, objectives, and the type of imaging (e.g., phase contrast or fluorescence). The components of this instrument are fully integrated and easy to set up. In a BioStation IM, cells are easily maintained at a constant temperature (37^{o}C) and relative humidity (85%) in a 5% CO_2 atmosphere. The BioStation IM enables time-lapse data to be collected reliably over hours or days without focus or image drift. In time-lapse experiments, images can be collected as quickly as 12 fraems/second. The fastest time interval is determined by the number of points which are selected by users. In a BioStation IM, imaging can be also performed in the X, Y and Z-direction. The unit comes with a well-designed software package and a GUI for controlling the instrument and all experimental parameters.

The BioStation IM is available in two models, the BioStation II and BioStation II-P, optimized for either glass bottom or plastic bottom culture dishes, respectively, and the magnification range is different in the two models. Both models accommodate 35mm and 60mm culture dishes. A four-chambered culture dish, the Hi-Q4 sold by Nikon, can be used for examining four different conditions of culture in the same experiment.

1.3 SOFTWARE USED FOR VIDEO BIOINFORMATICS ANALYSIS OF STEM CELL MORPHOLOGY AND DYNAMICS.

1.3.1 CL-Quant

CL-Quant (DR Vision, Seattle, WA) provides tools for developing protocols for recognition and quantitative analysis of images and video data [24]. The software is easy to learn and does not require an extensive knowledge of image-processing. CL-Quant can be used to detect, segment, measure, analyze, and discover cellular behaviors in video data. It can be used with both phase contrast and fluorescent images. Several basic protocols for cell counting, cell proliferation, wound healing, and cell migration have been created by DR Vision engineers and can be obtained when purchasing CL-Quant software. Protocols can be created by DR Vision at a user's request, or users can create their own protocols. Later in this chapter, we will describe how to create a protocol in CL-Quant, show the difference between a professional protocol and user-generated protocol, and also show an example in which CL-Quant was used to measure hESC spreading in experimental time-lapse videos.

1.3.2 ImageJ

ImageJ is a public domain Java-based image-processing program, which was developed at the National Institutes of Health. ImageJ was designed with an open architecture that provides extensibility via plugins and recordable macros. A number of tutorials are available on YouTube and are helpful for beginners learning to use this software. ImageJ is compatible with major operating systems (Linux, Mac OS X, and Windows), works with 8-bit color and grayscale, 16-bit integer, and 32-bit floating point images. It is able to read many image formats, and it supports time- or z-stacks. There are numerous plug-ins that can be added to ImageJ to help solve many imaging processing and analysis problems. ImageJ is able to perform numerous standard image-processing operations that may be useful in labs dealing with gel/image analysis and video bioinformatics. For example, researchers have used ImageJ to quantify bands in western blots and also to quantify the fluorescent intensity on the images. One of the advantages of using ImageJ is that it enables rapid conversion of images to different formats. For example, ImageJ can convert tif images to avi, it can create 3D images from z-stacks with 360 degrees rotation, and it can be used to obtain ground truth information when setting up a new video bioinformatics protocol.

1.4 PROTOCOLS FOR CELL ATTACHMENT AND SPREADING

In toxicological assays using [16,19). There has been interest in shortening such assays, often by using molecular biomarkers to obtain endpoints more rapidly [25]. In the mouse embryonic stem cells test, endpoints can now be obtained in 7 days using biomarkers for heart development. While this significantly reduces the time to reach an endpoint, it is still a relatively long time to obtain data on cytotoxicity.

Pluripotent hESC model the epiblast stage of development [26] and are accordingly a valuable resource for examining the potential effects of chemicals on an early stage of human prenatal development [27]. We are developing video assays to evaluate the health of hESC in short term cultures, and we then use these assays to identify chemicals that are cytotoxic to young embryos. One hESC based assay involves evaluation of cell spreading, a dynamic processes dependent on the cytoskeleton. When a treatment alters the cytoskeleton or its associated proteins, cells are not able to attach and spread normally. We have used two video bioinformatics protocols to analyze these parameters during 4 hours of *in vitro* culture. At the beginning of cell plating, hESC are round and unattached. Usually, hESC attach to their substrate and begin spreading within 1 hour of plating. As cells attach and start spreading, their area increases, and this can be measured in time-lapse images using video bioformatics tools, thereby providing a rapid method to evaluate a process dependent on the cytoskeleton. Two parameters can be derived from the time-lapse data: rate of cell spreading (slope) and fold increase in cell area. These two parameters were compared in control and treated groups using the linear regression and 2-way ANOVA analysis (GraphPad Prism, San Diego)

We will compare two protocols for measuring cell spreading in this chapter. Both protocols are performed using CL-Quant software. One, which we term a professional protocol, was created by DR-Vision engineers for quantifying cell proliferation. Even though the professional protocol was not created specifically for hESC spreading, we were able to use the segmentation portion of the protocol for measuring spreading (area) of hESC during attachment to Matrigel. In addition, we created our own protocol using CL-Quant for analyzing the area of hESC colonies during attachment and spreading.

Our method, which we refer to as the user-generated protocol, was created by a student with a basic background in biology and 1 month experience with CL-Quant software.

hESC were cultured using methods described in detail previously [28]. To create time-lapse videos for this project, small colonies of hESC were incubated in mTeSR medium at 37^0C and 5% CO_2 in a BioStation IM for 4 hours. Frames were captured every minute from 4-5 different fields. When applying either the professional or user-generated protocol, the first step was to segment the image so as to select mainly hESC. During segmentation, we used the DR Vision's soft matching procedure, which allowed us to identify the objects of interest. The second step was to remove noise and small particles/debris that were masked during segmentation. In the third step, the area of all cells in a field was measured in pixels. The protocol was applied to all images in time-lapse videos to obtain the area occupied by hESC when plated on Matrigel and incubated for 4 hours. Because the survival efficiency is low for single cells [29], hESC were plated as small colonies, which normally attach, spread, and survive well. Figure 1A shows phase contrast images of several small hESC colonies plated on Matrigel at different times over 4 hours. In the first frame, the cells were unattached, as indicated by the bright halo around the periphery of some cells. During 4 hours of incubation, the cells attached to the Matrigel and spread out. By the last frame, all cells in the field have started to spread. Figure 2.1A also shows the same images after segmentation, enhancement, and masking using the professional protocol supplied by DR Vision. Comparison of the phase contrast and segmented sequences shows that the masks fit each cell well.

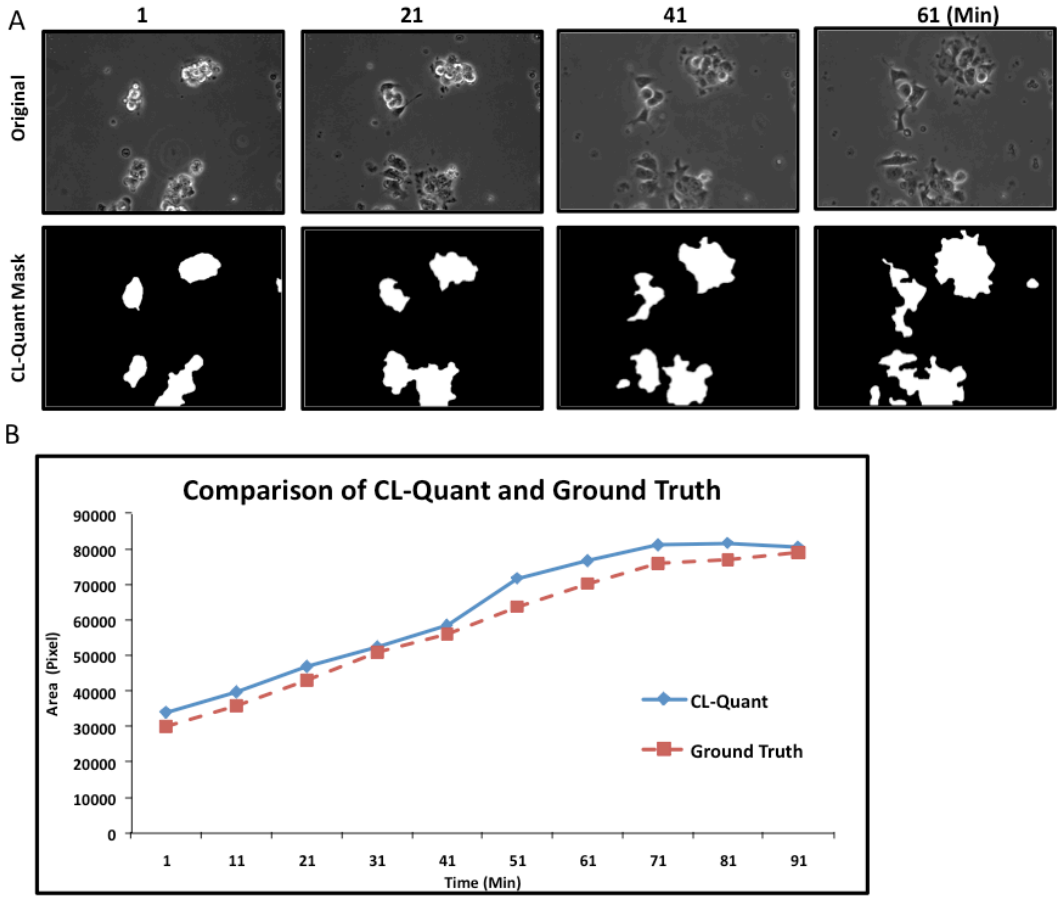

Figure 2.1: Comparison of CL-Quant segmentation protocol and ground truth. hESC were plated in mTeSR medium in a 35mm dish and incubated in a BioStation IM for 4 hours. (A) Phase contrast images modified with ImageJ to remove text labels and the same images with masks applied using the professional CL-Quant protocol. (B) Graph showing cell area (spreading) in pixels for CL-Quant derived-data and the ground truth. The areas obtained from the two methods were in good agreement.

To determine if the measurement data obtained from the professional CL-Quant protocol were accurate, ground truth was obtained by tracing each hESC in all of the video images using the freehand selection tool in ImageJ, and then measuring the pixel area for each frame. The ground truth (dotted line) and CL Quant derived area were very similar for hESC grown in control conditions (mTeSR medium) (Fig. 2.1 B). For most

times, CL Quant slightly overestimated the area of the cells due to difficulty in fitting a perfect mask to each cell.

1.5 APPLICATION OF VIDEO BIOINFORMATICS PROTOCOLS TO hESC CELL SPREADING IN THE PRESENCE OF ROCK INHIBITORS AND BLEBBISTATIN

In 2007, ROCK inhibitor (Y27632) was shown to increase the efficiency of hESC survival in culture [29]. However, ROCK is involved in numerous signaling pathways, and therefore may affect many cell properties [30]. ROCK inhibitors decrease non-muscle myosin II activity, and this decrease helps attachment of hESC. However, when single hESC are plated with ROCK inhibitor, they do not adhere to each other due to down regulation of e-cadherin [31]. In addition, hESC treated with Y27632, a potent ROCK inhibitor, appeared stressed and not as healthy as untreated controls [32]. Finally, the use of ROCK inhibitor (Y27632) in a toxicological study with methyl mercury decreased the IC_{50} [33]. Blebbistatin, an inhibitor of myosin II which is downstream of ROCK, can also be used to increase attachment of hESC and thereby improve plating efficiency [31] and may also alter cell morphology [34].

In this study, time-lapse data were collected on hESC treated with different ROCK inhibitors or blebbistatin, and two CL- Quant protocols were used to quantitatively compare spreading of treated cells to controls. H9 hESC were seeded on Hi-Q4 dishes coated with Matrigel and incubated using different treatment conditions. Cells were then placed in a BioStation IM and cultured as described above for 4 hours during which time images were taken at three or four different fields in each treatment/control group at 1-minute intervals.

The protocols described in section 1.4 for quantifying hESC area were used to compare spreading of cells subjected to different ROCK inhibitors (Y27632, H1152) or to blebbistatin. First, the written data that was stamped on each image by the BioStation software was removed using the remove outlier's feature in ImageJ. The professional CL-Quant protocol was applied to the resulting time-lapse videos. Examples of phase contrast and masked images are shown in Figure 2.2 for treatment with the two ROCK inhibitors and blebbistatin. Cells in each group were masked accurately by the segmentation protocol, and even thin surface cell projections were masked with reasonable accuracy. The measurement protocol was then applied to each frame to determine the area (pixels) of the masked cells. To establish the accuracy of this protocol, the ground truth for control and treated groups was determined using ImageJ in two separate experiments (Fig. 2.3A, B). Each point in Figure 2.3 is the mean of 3 or 4 videos. As shown in Figure 2.3, the ground truth and the CL-Quant derived data were in good agreement for all groups in both experiments.

In the first experiment, the fold increase in spread area was elevated by Y27632 and blebbistatin relative to the control ($p<0.0001$ for Y27632 and $p<0.05$ for blebbistatin 2-way ANOVA, Graphpad Prism), while H1152 was not significantly different than the control ($p>0.05$). The rate of spreading, as determined by the slope for each group, was greater in the three treated groups than in the control; however, only the slope for Y27632 was significantly different than the control ($p<0.0001$) (slopes = 0.124 control; 0.135 H1152; 0.142 blebbistatin; 0.245 Y27632). In this experiment, the Y27632 group was distinct from all other groups in both its rate of spreading and fold increase in spread area. The morphology of the control cells was normal; cells had smooth surfaces with

relatively few projections. In contrast, all treated cells had irregular shapes and more projections than the controls (Fig. 2.3 A).

In the second experiment, the three treated groups spread faster and more extensively than the control group. All three treated groups were significantly different than the control with respect to fold change in spread area (by 2-way ANOVA $p < 0.05$ for Y27632 and H1152; $p < 0.0001$ for blebbistatin). In contrast to the first experiment, the Y27632 group was similar to the other two treatments (Fig. 2.3 D). The rate of spreading was greater in the three treated groups than in the control (slope = 0.084 control; 0.117 H1152; 0.150 blebbistatin; 0.136 Y27632), and both Y27632 ($p<0.01$) and blebbistatin ($p<0.001$) were significantly different than the control. As see in the first experiment, all treated cells were morphologically distinct from the controls. Treated cells appeared attenuated and had long thin projections extending from their surfaces, while control cells were compact and had smooth surfaces (Figs. 2.3 C). It is possible that CL-Quant underestimated the area of the Y27632 inhibitor treated cells in the second experiment due to the attenuation of the surface projections, which were more extensive than in the first experiment and were difficult to mask accurately.

Video showing the effect of ROCK inhibitors and blebbistatin on hESC spreading can be viewed by scanning the bar code.

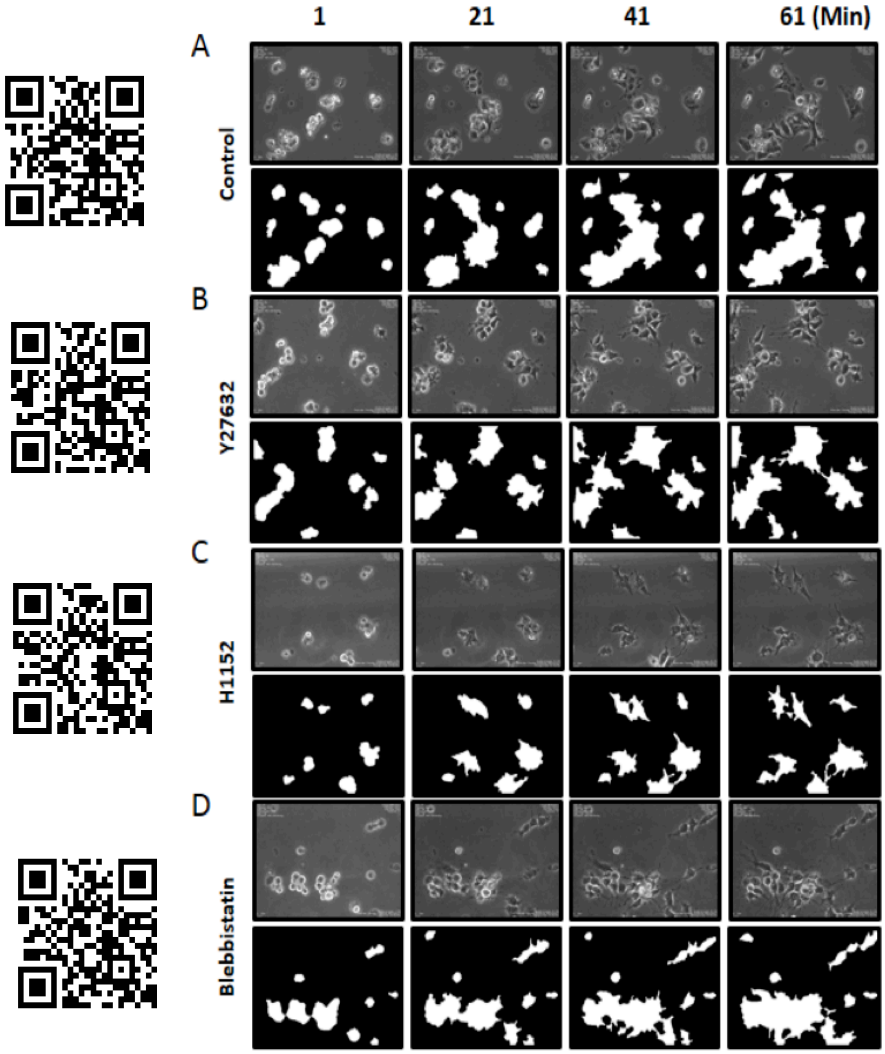

Figure 2.2: Cell area (spreading) was successfully masked by the professional CL-Quant protocol in different experimental conditions. hESC were treated with ROCK inhibitors (Y27632 and H1152) or blebbistatin, incubated in a BioStation IM for 4 hours, and imaged at 1 minute intervals. Phase contrast images and the corresponding masked images are shown for hESC treated with: (A) control medium, (B) Y27632, (C) H1152, and (D) blebbistatin

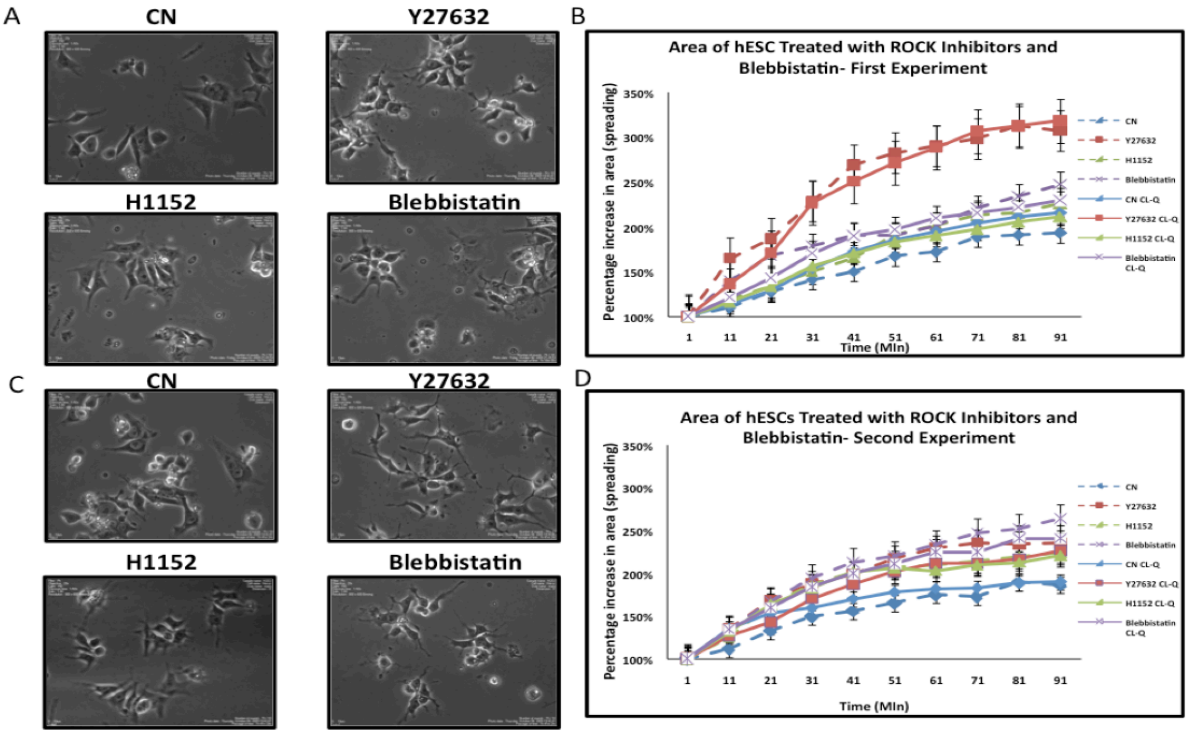

Figure 2.3: The morphology and spreading of hESC was affected by treatment with ROCK inhibitors (Y27632 and H1152) and blebbistatin in two experiments. Spreading was measured using the professional CL-Quant protocol. (A) Phase contrast images from the first experiment showed that treated cells were morphologically different than the control. (B) The rate of spreading and the fold increase in spread area was greater in Y27632 and blebbistatin treated cells than in controls. (C) Phase contrast images of control and treated cells in the second experiment showed morphological changes in the treated groups. (D) The fold increase in spread area was greater in the treated cells than in the controls in the second experiment; however, the effect of Y27632 was not as great as previously seen. Data in B and D are plotted as a percentage of the area in the first frame. Each point is the mean ± the SEM.

1.6 COMPARISON OF PROFESSIONAL AND USER-GENERATED PROTOCOLS

We also compared the professional and user-generated protocols to each other. The cells in both the control and treated groups were well masked by the professional protocol, and the mask included the thin surface projections characteristic of the treated group (Fig. 4A). To validate the quantitative data obtained with the professional protocol, ground truth was determined using ImageJ (Figs. 4B). Both the control and treated groups were in good agreement with the ground truth (Fig.4B).

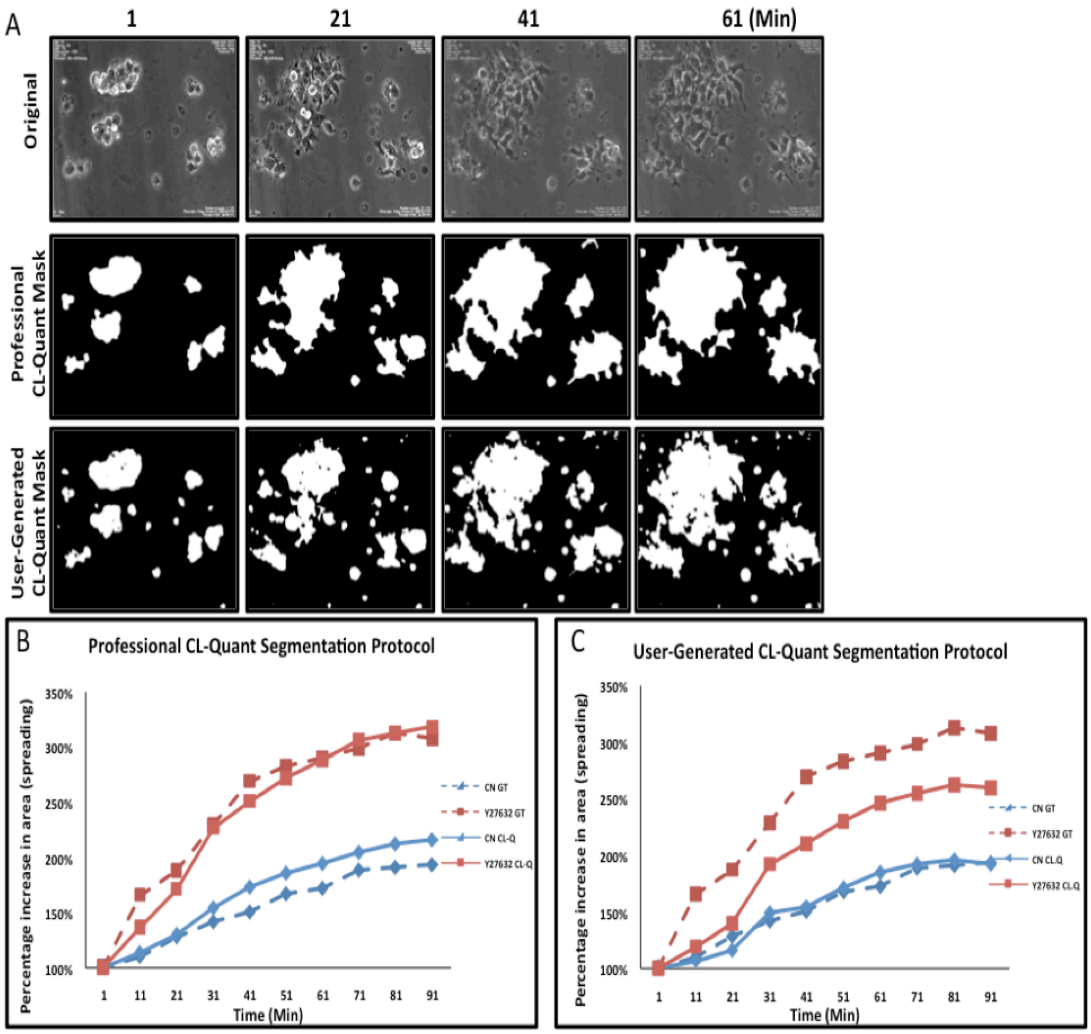

Figure 2.4: Comparison of the professional and user-generated cell spreading protocols. (A) Phase contrast micrographs of hESC treated with Y27632 and the corresponding masks created with the professional and user–generated protocols. (B) Comparison of ground truth to area (spreading) data obtained with the professional protocol in control and treated groups (C) Comparison of ground truth to area (spreading) data obtained with the user-generated protocol in control and treated groups.

An advantage CL-Quant is that users can generate their own protocols without a programming background. Our user-generated protocol, which was created by a student with 1 month of experience using CL-Quant, was applied to the control and treated groups. The resulting masks did not cover the surface projections of the treated group as well as the professional protocol; however, the user-generated protocol did include

single cells, some of which were filtered out by the professional protocol (Fig. 2.4 A). The user-generated protocol did not filter out the small debris as well as the professional protocol (Fig. 2.4 A). The data obtained with the user-generated protocol were close to ground truth for the control group, but not for the treated group (Fig. 2.4 C). Phase contrast images showed that the cells treated with Y27632 had many more attenuated surface projections than the control cells (Figs. 2.5 A, D). Our user-generated protocol and the professional protocol were able to mask the control cells well (Fig. 2.5 B, C). However the user-generated protocol was not able to mask the thin projections on treated cells as well as the professional protocol (Figs. 2.5 E, F). Neither protocol recognized gaps between cells in the treated group. Overall, the professional protocol was more similar to the ground truth than the user-generated protocol in this experiment; however, with more experience, the user could improve the protocol to include surface projections more accurately.

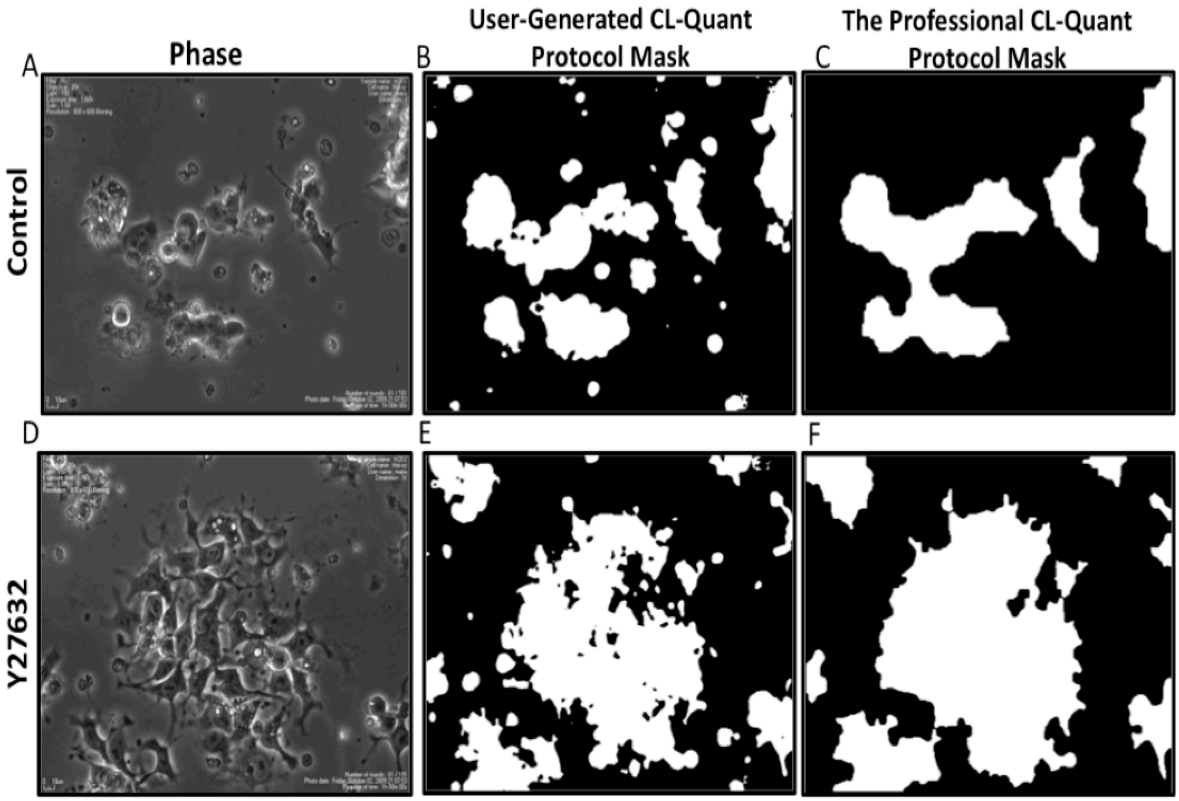

Figure 2.5: Differences in cell morphology showing why treated hESC are more difficult to segment than control cells. (A) Phase contrast image of hESC colonies taken at 60 minutes of incubation. Segmentation of the image in "A" created with the user-generated protocol (B) and the professional protocol (C). (D) Phase contrast image of hESC colonies treated with Y27632 for 60 minutes. The cells have many thin surface projections not present on controls. Segmentation of the image in "C" with the user-generated protocol (E) and the professional protocol (F).

1.7 DISCUSSION:

In this chapter, we introduced a video bioinformatics protocol to quantify cell spreading in time- lapses videos using CL-Quant image analysis software, and we validated it against ground truth. A professionally developed version of the protocol was then compared to a protocol developed by a novice user of CL-Quant. We also applied

this protocol to hESC treated with blebbistatin and ROCK inhibitors, which are commonly used during *in vitro* passaging of hESC [29].

Most evaluations of cells in culture have involved processes such as cell division, confluency and motility, but not spreading. Cell attachment and spreading depend on the interaction between cells and the extracellular matrix to which they attach. When cells are plated on a substrate, they first attach, then flatten and spread. At the molecular level, spreading depends on the interaction of membrane-based integrins with their extracellular matrix and the engagement of the cytoskeleton, which initiates a complex cascade of signaling events [35]. This in turn leads to the morphological changes observed during spreading and enables cultured cells to flatten out and migrate to form colonies [36,37].

Changes in cell behavior that depend on the cytoskeleton often indicate that cell health is being compromised by environmental conditions [16,20]. Because spreading depends on the cytoskeleton, it can be used to evaluate the effect of chemical treatments on cytoskeletal health. Cell spreading is a particularly attractive endpoint in toxicological studies as it occurs soon after plating and does not require days or weeks of treatment to observe. Many types of cells, such as fibroblasts can attach and spread in 10-15 minutes. hESC require about 1– 2 hours to spread, and therefore can be plated and data collected in 4 hours or less time depending on the experimental design.

The application of the spreading protocol to hESC enables chemical treatments to be studied using cells that model a very early stage of post-implantation development. hESC are derived by isolating and culturing inner cell mass cells from human blastocysts. As these cells adapt to culture, they take on the characteristics of epiblast cells which are found in young post-implantation embryos [26]. Embryonic cells are often

more sensitive to environmental chemicals than differentiated adult cells, and it has been argued that risk assessment of environmental chemicals should be based on their effects on embryonic cells, as these represent the most vulnerable stage of the life cycle [38]. The sensitivity of hESC to environmental toxicants may be due to mitochondrial priming which occurs in hESC and makes them more prone to apoptosis than their differentiated counterparts [39].

A major advantage of the cell spreading assay is that it requires relatively little time to perform. A complete spreading assay can be done in as little as 4 hours, while other endpoints such as cell division and differentiation require days or weeks to evaluate. The rapidity of the spreading assay makes it valuable in basic research on the cytoskeleton or in toxicological studies involving drugs or environmental chemicals. Moreover, this tool could be used in the future as a quality control check when evaluating stem cell health for clinical applications.

The cell spreading assay introduced in this chapter provides a rapid method for evaluating cell health and assessing the quality of cells. Using bioinformatics tools to analyze the video data significantly reduces the time for data analysis [40,41,42,43]. If an experiment is done for 4 hours with 1 min intervals between frames, 240 frames would be collected for each video by the end of the experiment. Each group could have 4-10 different videos. Before we used bioinformatics tools to analyze our data, cell spreading was analyzed by measuring cell area manually. ImageJ was used to calculate cell area for each frame. The total time for cell spreading analysis for each video was about 24 hours. The CL-Quant bioinformatics protocol, which we introduced in this chapter, greatly reduces this time. In general, it takes about 30~60 minutes to create a protocol for a specific purpose. Once the protocol is created, it takes 5 minutes to run the

protocol using CL-Quant. The protocol can be batch run on multiple videos without requiring users to tie up valuable time performing analysis of spreading.

Our data show that the professionally developed protocol performed better than the one developed by the novice user. However, the novice was able to rapidly learn to use CL-Quant software, and he obtained accurate control data as shown by comparison to the ground truth. It was clear that the novice had difficulty masking the fine projections on the hESC surfaces, but with additional training, he would likely be able to create a better segmentation protocol and achieve more accurate masking of the treated group data.

We also examined the effect of ROCK inhibitors and blebbistatin on hESC spreading. The ROCK inhibitors and blebbistatin improved cell attachment and spreading, as reported by others [29,31]. However, those hESC treated with ROCK inhibitors or blebbistatin appeared stressed, had thin attenuated projections off their surfaces, and did not seem as healthy as control cells. ROCK inhibitor or blebbistatin are often used to improve cell survival, especially when plating single cells. ROCK inhibitor and blebbistatin allow cells to be counted and accurate numbers can be plated. Cell survival is also improved by the efficient attachment observed when these ROCK inhibitors and blebbistatin are used. Cells are stressed during nucleofection, so ROCK inhibitors are often used to improve cell survival when nucleofected cells are ready to plate. ROCK inhibitors and blebbistatin inhibit ROCK protein and downregulate myosin II activity which accelerates cell attachment and cell spreading [29]. Our analysis shows that both ROCK inhibitors and blebbistatin alter the morphology of spreading cells. Moreover, Y27632 and blebbistatin significantly increased the rate of spreading and the fold change in spread area when compared to untreated controls, which may be a factor

in why they are more commonly used than H1152. While the full significance of the above changes in cell morphology and behavior are not yet known, these inhibitors do either indirectly or directly decrease myosin II activity, which may lead to the stressed appearance of the treated cells. It has not yet been established why decreasing myosin II activity leads to more rapid and extensive spreading of hESC. .

Use of ROCK inhibitors is not recommended in toxicological applications of hESC as they can alter IC_{50}s [33]. A spectrophotometer method has been established to determine cell number when hESC are in small colonies [44]. This method enables an accurate number of cells to be plated without the use of ROCK inhibitors. This method may generally be applicable to hESC culture and would avoid the morphological stress observed in ROCK inhibitor treated cells.

The protocols reported in this chapter can be used to quantify two parameters of cell spreading, rate and fold change. The use of spreading as an assay for cell health is attractive as it takes relatively little time to collect data and with the application of video bioformatics tools relatively little time is required to analyze data. In the future, the segmentation and filtering aspects of these protocols may be improved to better gather data on the challenging cell surface projections, but these protocols in their current form can be reliably applied to spreading of hESC colonies.

1.9 REFERENCES:

1. Talbot P. Videotape analysis of hamster ovulation in vitro. Journal of Experimental Zoology, 1983:225(1):141-148

2. Howard, D.R. and Talbot P. In vitro contraction of lobster (Homarus) ovarian muscle: methods for assaying contraction and effects of biogenic amines. Journal of Experimental Zoology, 1992:263(4): 356-366.

3. Tsai KL and Talbot P. Video microscopic analysis of ionophore induced acrosome reactions of lobster (Homarus americanus) sperm. Molecular Reproduction and Development, 1993:36(4):454-461

4. DiCarlantonio G, Shaoulian R, Knoll M, Magerts T, and Talbot P. (1995) Analysis of ciliary beat frequencies in hamster oviducal explants. Journal of Experimental Zoology, 1995:272(2):142-152

5. Huang, S., N. Driessen, M. Knoll, and P. Talbot. In vitro analysis of oocyte cumulus complex pick-up rate in the hamster Mesocricetus auratus. Molec Reprod Develop, 1997:47:312-322.

6. Talbot P., Geiske C., and Knoll M. Oocyte pickup by the mammalian oviduct. Molecular Biology of the Cell, 1999:10(1):5-8

7. Knoll, M., Shaoulian, R., Magers, T., and Talbot, P. Ciliary beat frequency of hamster oviducts is decreased in vitro by exposure to solutions of mainstream and sidestream cigarette smoke. Biology of Reproduction, 1995:53(1):29-37.

8. Knoll M. and Talbot P. Cigarette smoke inhibits oocyte cumulus complex pick-up by the oviduct in vitro independent of ciliary beat frequency. Reproductive Toxicology, 1998:12(1):57-68.

9. Talbot P., DiCarlantonio G., Knoll M., and Gomez C. Identification of cigarette smoke components that alter functioning of hamster (Mesocricetus auratus) oviducts in vitro. Biology of Reproduction, 1998:58(4):1047-1053

10. DiCarlantonio G. and Talbot P. Inhalation of mainstream and sidestream cigarette smoke retards embryo transport and slows muscle contraction in oviducts of hamsters (Mesocricetus auratus). Biology of Reproduction, 1999:61(3):651-656.

11. Riveles K.,Iv M., Arey J., and Talbot P. Pyridines in cigarette smoke inhibit hamster oviductal functioning in picomolar doses. Reproductive Toxicology, 2003:17(2):191-202

12. Riveles K., Roza R., Arey J., and Talbot P. Pyrazine derivatives in cigarette smoke inhibit hamster oviductal functioning. Reprod Biol Endocrinol, 2004:2(1):23

13. Riveles K., Roza R., and Talbot P. Phenols, quinolines, indoles, benzene, and 2-cyclopenten-1-ones are oviductal toxicants in cigarette smoke. Toxicological Sciences, 2005:86(1):141-151

14. Riveles K., Tran V., Roza R., Kwan D., and Talbot P. Smoke from traditional commercial, harm reduction and research brand cigarettes impairs oviductal functioning in hamsters (Mesocricetus auratus) in vitro. Human Reproduction, 2007:22(2):346-355

15. Gieseke C. and Talbot P. Cigarette smoke inhibits hamster oocyte pickup by increasing adhesion between the oocyte cumulus complex and oviductal cilia. Biology of Reproduction, 2005:73(3):443-451

16. Lin, S., Fonteno S., Weng J-H., and Talbot P. Comparison of the toxicity of smoke from conventional and harm reduction cigarettes using human embryonic stem cells. Toxicological Sciences, 2010a:118:202-212.

17. Talbot, P. and Lin, S. Cigarette smoke's effect on fertilization and pre-implantation development: assessment using animal models, clinical data, and stem cells. Journal of Biological Research, 2010:44:189-194.

18. Lin, S., Fonteno S., Satish S., Bhanu B., and Talbot P. Video Bioinformatics Analysis of Human Embryonic Stem Cell Colony Growth. Journal of Visualized Experiments, 2010b: http://www.jove.com/index/details.stp?id=1933.

19. Talbot, P., zur Nieden, N., Lin, S., Martinez, I., Guan, B., Bhanu, B. Use of video bioinformatics tools in stem cell toxicology. Handbook of Nanomedicine, Nanotoxicology and Stem Cell Use in Toxicology, 2014, in press.

20. Bahl, V., Lin, S., Xu, N., Davis, B., Wang, Y., & Talbot, P. Comparison of electronic cigarette refill fluid cytotoxicity using embryonic and adult models. Reproductive Toxicology, 2012:34(4):529-537.

21. Behar, R. Z., Davis, B., Wang, Y., Bahl, V., Lin, S., and Talbot, P. Identification of toxicants in cinnamon-flavored electronic cigarette refill fluids. Toxicology In Vitro, 2013:10:006.

22. Cervinka, M., Cervinkova, Z., and Rudolf, E. (2008). The role of time-lapse fluorescent microscopy in the characterization of toxic effects in cell populations cultivated in vitro. Toxicol. In Vitro, 2008:22(5): 1382-138.

23. Lin, Sabrina C., Yip, Henry, Phandthong, George, Davis, Barbara and Prue Talbot. Evaluation of cell behavior and health using video bioinformatics tools. Video Bioinformatics, Eds B. Bhanu and P. Talbot, Springer, 2014.

24. Alworth, S. V., Watanabe, H., and Lee, J. S. Teachable, high-content analytics for live-cell, phase contrast movies. J. Biomol. Screen 2010:15(8):968-77.

25. Buesen, Roland Genschow, Elke Slawik, Birgitta, Visan, Anke, Spielmann, Horst, Luch, Andreas and Seiler, Andrea. Embryonic Stem Cell Test Remastered: Comparison between the validated EST and the new molecular

FACS-EST for assessing developmental toxicity in vitro. Toxicological Sciences, 2009:108(2):389–400.

26. Nichols J, Smith A. Naïve and primed pluripotent states. Cell Stem Cell, 2009:4(6):487-492

27. Talbot P., and Lin S. Mouse and human embryonic stem cells: can they improve human health by preventing disease? Current Topics in Medicinal Chemistry, 2011:11:1638-52.

28. Lin, Sabrina and P. Talbot. Methods for culturing mouse and human embryonic stem cells. Embryonic Stem Cell Therapy for Osteodegenerative Disease, Humana Press, 2010:31-56.

29. Watanabe K., Ueno M., Kamiyq D., Nishiyama A., Matsumura M., Wataya T., Takahashi JB., Nishikawa S., Muguruma K., Sasai Y. A ROCK inhibitor permits survival of dissociated human embryonic stem cells. Nature Biotechnology, 2007:25(6):681-686

30. Liao JK., Seto M., and Noma K. Rho Kinase (ROCK) inhibitors. J Cardiovasc Pharmacol, 2007:50(1):17-24.

31. Harb N., Archer TK., and Sato N. The Rho-ROCK-Myosin signaling axis determines cell-cell integrity of self-renewing pluripotent stem cells. PLos One, 2008:3(8):e3001.

32. Behar, R.Z., Bahl, V., Wang, Y., Weng, J., Lin, S.C., Talbot, P. Adaptation of stem cells to 96-well plate assays: use of human embryonic and mouse neural stem cells in the MTT assay. Current Protocols Stem Cell Biol. 2012a:Chapter 1:Unit1C 13.

33. Fujimura M, Usuki F., Kawamura M., and Izumo S. Inhibition of the Rho/ROCK pathway prevents neuronal degeneration in vitro and in vivo following methylmercury exposure. Toxicol Appl Pharmacol, 2011:250(1):1-9.

34. Holm, F., Nikdin H., Kjartansdottir K., et al (2013) Passaging techniques and ROCK inhibitor exert reversible effects on morphology and pluripotency marker gene expression of human embryonic stem cell lines. Stems Cells and Development 2013:22:1883-1892.

35. Cuvelier D., Thery M., Chu YS., Thiery JP., Bornens M., Nassory P., Mahadevan L. The universal dynamics of cell spreading. Current Biology, 2007:17(8):694-699

36. Lauffenburger D.A., and Horwitz A.F. Cell migration: a physically integrated molecular process. Cell, 1996:84:359-369.

37. Woodhouse E.X., Chuaqui R.F., and Liotta L.A. General mechanisms of metastasis. Cancer, 1997:80:1529-1537.

38. Grandjean, P., Bellinger, D., Bergman, A., Cordier, S., et al. The Faroes statement: human health effects of developmental exposure to chemicals in our environment. Basic Clin. Pharmacol, 2007:102:73–75.

39. Liu JC., Guan X., Ryan JA., Rivera AG., Mock C., Agarwal V., Letai A, Lerou PH., Lahav G. High mitochondrial priming sensitizes hESCs to DNA-damage-induced apoptosis. Cell Stem Cell, 2013:13(4):483-491.

40. Guan, B. X., Bhanu, B., Thakoor, N., Talbot P., and Lin S. Human embryonic stem cell detection by spatial information and mixture of Gaussians. IEEE First International Conference on Healthcare Informatics, Imaging and Systems Biology, 2011:307-314.

41. Guan, B. X., Bhanu B.,Talbot P., and Lin S. Detection of non-dynamic blebbing single unattached human embryonic stem cells. IEEE International Conference on Image Processing, 2012a:2293-2296.

42. Guan, BX., Bhanu, B., Talbot, P., and S Lin. Automated human embryonic stem cell detection.
IEEE Second International Conference on Healthcare Informatics, Imaging and Systems Biology, (HISB). 2012b

43. Guan, B. X., Bhanu, B., Thakoor, N., Talbot P., and Lin S. Automatic cell region detection by K-means with weighted entropy. International Symposium on Biomedical Imaging: From Nano to Macro, San Francisco, CA , 2013.

44. Behar, R. Z., Bahl, V., Wang, Y., Lin, S., Xu, N., Davis, B., & Talbot, P. A method for rapid dose-response screening of environmental chemicals using human embryonic stem cells. J Pharmacological and Toxicological Methods, 2012b:66:238-245.

Chapter 3

Improving Culture of Human Embryonic Stem Cells by Regulating Dynamic Blebbing Through Laminin-Integrin Signaling

Nikki Jo-Hao Weng[1,2], Cindy Cheung[1], and Prue Talbot[1,2]

1. Department of Cell Biology and Neuroscience, University of California, Riverside, California, 92521

2. Cell Molecular and Developmental Biology Graduate Program, University of California, Riverside, California, 92521

Authors contributions:

NW: Concept and design, collection and assembly of data, data analysis and interpretation, manuscript writing

CC: Collection of data, data analysis and interpretation

PT: Concept and design, assembly of data, data analysis and interpretation, manuscript writing, financial support, final approval of manuscript

Corresponding author: Prue Talbot, PhD., Department of Cell Biology & Neuroscience, University of California, Riverside CA. 92521 951-827-3768 phone; 951-827-4207 FAX; talbot@ucr.edu

The authors have no conflicts of interest to acknowledge.

Grant support: This work was supported by the California Institute for Regenerative Medicine Core Grant #CL1-00508, an NSF IGERT grant on Video Bioinformatics # DGE-093667, and grants from the Academic Senate.

ABSTRACT

Improvements in methods to culture human embryonic stem cells (hESC) are needed for future translation and clinical application of stem cell therapies. Live cell imaging was used to show that during passaging, hESC undergo extensive dynamic blebbing, which inhibits cell attachment and eventually leads to apoptotic blebbing and cell death. The goals of this study were to characterize dynamic blebbing and develop improved culture methods to increase plating efficiency and cell survival by reducing dynamic blebbing. Manipulations of the cytoskeleton by depolymerizing microtubules extended dynamic blebbing, while drugs that depolymerized actin filaments or blocked myosin II inhibited blebbing. Plating single cells at low density on recombinant laminin-521 dramatically decreased dynamic blebbing and improved cell attachment and survival. A similar positive effect on attachment and survival was observed when laminin-111 was added to Matrigel. When cell attachment was prevented with a function blocking antibody to integrin α6, a laminin receptor, blebbing continued. Additionally, inhibition of focal adhesion kinase, which is activated by binding of integrins to laminin, prolonged dynamic blebbing and inhibited attachment. These data are consistent with the idea that hESC bind rapidly to laminins (especially to laminin-521) through a cell surface integrin, which activates a focal adhesion kinase that in turn downregulates dynamic blebbing. Addition of laminin to Matrigel or use of recombinant laminin-521 enables hESC to rapidly attach during passaging, improves plating efficiency, enables passaging of single pluripotent stem cells, and avoids use of inhibitors that may have non-specific, unknown, or unwanted effects.

SIGNIFICANCE

Passaging of human embryonic stem cells (hESC) is usually done using small colonies and plating efficiency can be low due to failure of cells to attach to the culture plate. This study shows that failure to attach is due to dynamic blebbing and when attachment does not occur, cells eventually undergo apoptosis. Following plating of hESC, dynamic and apoptotic blebbing differed in time of occurrence, bleb retraction rate, mitochondrial membrane potential, and caspase 3&7 activation. Dynamic blebbing can be prevented by regulating the cytoskeleton with drugs that inhibit myosin II; however, these may not be desirable in clinical applications of stem cells. We show that laminin-521 and addition of laminin-111 to Matrigel provides a safe method to drastically decrease dynamic blebbing and improve cell attachment with proteins normally found in the inner cell mass. These data provide a strategy for improving hESC culture with single cells using biologically safe recombinant human proteins rather than drugs, which can have unwanted effects.

INTRODUCTION

Human embryonic stem cells (hESC) were derived in 1998 [1], 16 years after their first mouse counterparts were reported [2,3]. hESC are generally derived from spare blastocysts offered for research purposes by patients undergoing *in vitro* fertilization [1]. Originally, hESC were cultured on mouse embryonic fibroblasts. However, many groups have worked on developing new protocols that do not need non-human components for hESC culture [4,5]. Two major improvements in hESC culture were the replacement of feeder layers with Matrigel, a hESC-qualified matrix, and the introduction of better defined, feeder-free maintenance culture media, such as mTeSR [5,6,7]. In spite of these improvements, hESC do not readily attach to substrates and cannot easily be plated as single cells.

Cell blebs can be either dynamic (non-apoptotic) or apoptotic. Apoptotic blebs occur on the surfaces of cells during death and have been reported in numerous studies [8,9,10]. Dynamic blebs are membrane protrusions that appear and disappear from the surface of healthy cells [11]. Dynamic blebbing occurs in three phases: nucleation, expansion, and retraction [12]. During nucleation, blebs begin to form when small areas of the plasma membrane detach from the cortical actin or when a local rupture occurs in the cortical actin. Once a bleb is nucleated, hydrostatic pressure in the cytoplasm drives bleb expansion causing cytosol to flow into the developing bleb [12]. During expansion, the plasma membrane detaches further from the cortex, increasing bleb size. As bleb expansion slows, a new actin cortex reforms under the bleb membrane, and the motor protein myosin II is recruited to the bleb to power retraction. Dynamic blebbing is a normal process during cytokinesis, when blebs appear at the poles of dividing cells [13,14,15,16,17,18], and in some cells, dynamic blebbing is the driving force that

enables cell migration [19]. Therefore, dynamic blebbing appears to be an important physiological process in certain circumstances. Dynamic blebbing also plays a role in certain diseases. For example, blebbing provides the motive force for invasion of tissue by *Entamoeba histyltica* and migration of breast cancer cells during metastasis [20].

Like many other cell types, dissociated single hESCs form a number of blebs on their surfaces during passaging [21,22,23,24,25]. Blebbing of hESC begins when colonies are dissociated into single cells or small colonies during passaging. hESC that are undergoing vigorous dynamic blebbing do not attach well to Matrigel-coated dishes. Because hESC that fail to attach eventually undergo apoptosis, blebbing of hESC is sometimes considered to be apoptotic [26]. Understanding and controlling blebbing in hESC is important as it decreases plating efficiency and hinders bulk production of hESC that would be needed in stem cell clinics for therapeutic applications. It also precludes plating of single cells for applications that require knowledge of cell numbers, such as toxicological studies or drug testing.

To circumvent plating inefficiencies due to blebbing, Rho-associated protein kinase (ROCK) inhibitor (Y27632) is often used in hESC culture medium to facilitate attachment [21,27,28,29]. ROCK inhibitor suppresses blebbing by inhibiting ROCK which in turn inhibits non-muscle myosin II. However, Y27632 stresses cells, which appear morphologically abnormal during ROCK inhibitor treatment [22] and may not be acceptable for culturing cells that are eventually used for therapeutic purposes. Inclusion of ROCK inhibitor in hESC culture medium also alters IC_{50} values in toxicological studies [30], raising further concern about its use in quantitative applications.

The goals of this study were to characterize the types of blebbing that occur during plating of hESC, to identify methods that reduce dynamic blebbing during passaging, and to identify targets that will enable further development of strategies to regulate blebbing during passaging, thereby leading to improved culture protocols that will be suitable for all hESC applications.

MATERIALS AND METHODS

Inhibitors and Depolymerizers

Nocodazole and cytochalasin D were purchased from Sigma Aldrich (St Louis, MO), and latrunculin A and swinholide A were gifts from Dr. Leah Haimo. Blebbistatin and ROCK inhibitors (Y27632 and H1152) were from Tocris Bioscience (Minnesota, USA). FAK inhibitor 14 was purchased from Sigma Aldrich (St Louis, MO) and Integrin α6/CD49f antibody was purchased from R&D systems (Minneapolis, MN).

Cell Culture

Experiments were done using H9 hESCs purchased from WiCell (Madison, WI). Before setting up experiments, hESCs were expanded by plating on Matrigel-coated 6-well plates. Cultures were maintained in mTeSR medium (Stem Cell Technologies, Inc. Vancouver, Canada) in 5% CO_2 at 37 °C and 95% relative humidity as described in detail previously [31,32,33]. When colonies reached 70%-80% confluency (about 1 to 1.5 million cells), hESC were used in experiments. For single cell experiments, cells were detached with Accutase (eBioscience, San Diego, CA) for 3 minutes. A 1 ml pipette was used to rinse cells off the plate by pipetting the Accutase repeatedly. Once the cells detached from the plate, Accutase was neutralized using mTeSR medium. To separate colonies into single cells, they were passed through an 18-gauge syringe needle and 150,000 cells were plated in 35 mm high culture dishes for live cell imaging (Ibidi, Wisconsin, USA). Dynamically blebbing cells were studied immediately after plating on Matrigel (Corning, NY) or laminin-521 (Biolamina, Sweden) coated-dishes, while apoptotically blebbing cells were studied after 1.5 hours of incubation on non-coated dishes, which prevent attachment.

Mouse embryonic fibroblasts (mEF) were derived from 12.5-day to 13.5-day pregnant mouse using the ATCC protocol and then frozen in liquid nitrogen [31,32, 33]. mEF were expanded by plating on 0.1% gelatin (Sigma 128-K-0066, St Louis MO.) in T-25 flasks. Cultures were maintained in MEF Medium (450 ml DMEM, 50ml FCS, 5ml 1X L-glutamine, 5 ml 1X non-essential amino acids, and 5 ml 1X sodium pyruvate) in 5% CO_2 at 37 °C. When MEFs were 90% confluent, they were used in experiments. MEFs were detached from flasks with 0.25% trypsin for 1.5 minutes. MEF medium was used to inactivate the trypsin. Cells were centrifuged at 1,200 rpm for 3 minutes, resuspended in MEF medium, and cells were plated in Ibidi culture dish for live-cell imaging.

D3 mouse embryonic stem cells (mESC) were purchased from ATCC (#CRL-11632, Manassas, VA) and used as described previously [34]. All experiments were done with passages 9-24. D3 mESC were plated on mitotically inactivated mEFs in stem cell medium containing 81.5% DMEM, 15% FBS, 0.98% L-glutamine, 0.98% sodium pyruvate, 0.98% non-essential amino acids, 0.5% penicillin/streptomycin, 0.00065% beta-mercaptoethanol and 0.00025% leukemia Inhibitory factor (LIF). The medium was changed daily. Cells were used for experiments at 70-75% confluency.

The prostate cancer cells were a gift from Dr. Manuela Martins-Green (UCR) and were provided for a one-time use in their standard culture medium [35].

Use of live cell-imaging to compare dynamic blebbing in four cell types

A Nikon BioStation IM, which combines an incubator, microscope, and cooled CCD camera, was used to collect time-lapse video data [22,36,37]. To create time-lapse videos, human prostate cancer cells, mEF, mESC, and hESC were plated on 35 mm culture dishes and incubated in a BioStation IM. Frames were captured every 3 minutes

for 6 hours from 10-12 different fields. To quantify blebbing and cell attachment during the first 100 minutes of incubation, cells in videos were classified as blebbing or attached based on their morphology. The percentage of blebbing and attached cells were counted every 20 minutes for 100 minutes. To determine the number of blebs/cell, cells were randomly picked from five videos in three different experiments. More than 50 cells were analyzed in each group. The number of blebs produced by the cells was counted manually. In some experiments, the intensity of dynamic and apoptotic blebs was analyzed using Image J.

Verification that Live Cells Were Healthy and Dying Cells Were Undergoing Apoptosis

MitoTracker Red CMXRos (ThermoFisher Scientific, Waltham, MA) and the Magic Red Caspase 3&7 Assay Kit (ImmunoChemistry, Bloomington, MN) were used to evaluate cell health and apoptosis. Mitotracker is a red-fluorescent dye that enters the mitochondria in live cells; its accumulation is dependent on the mitochondrial membrane potential. The Magic Red kit measures apoptosis by detecting active forms of caspase 3 and 7 in living cells. H9 hESCs were loaded with 250 nM of Mitotracker or Magic Red during plating on a 35mm dish in a BioStation IM. Phase contrast and fluorescent images were captured at 40X magnification every 10 minutes for 12 hours from 10 different fields in each experiment. A total of 3 experiments was performed.

Comparison of the Rate of Bleb Formation and Retraction in Dynamic and Apoptotic Cells

Single hESCs were incubated on non-coated 35 mm dishes in a BioStation IM. Real time videos (30 fps) were collected from the BioStation monitor using a Canon 1080p HD Video Camcorder (Melville, NY). The rates of bleb formation and retraction were analyzed between 0 and 1 hour and between 1.5 and 2.5 hours for dynamic and apoptotic blebbing, respectively. Videos were analyzed manually to determine the time required for bleb formation and retraction for both dynamic and apoptotic blebs. Bleb size was followed from the time a bleb was produced until it fully retracted. Formation time was then calculated from the beginning frame to the frame when bleb size was the largest. The retraction time was calculated from the frame of the largest bleb size to the frame when the bleb was fully retracted back to the cell body.

Cytoskeleton Distribution During Dynamic and Apoptotic Blebbing

Dynamically blebbing cells were studied immediately after plating on Matrigel coated dishes, while apoptotically blebbing cells were studied after 1.5 hours of incubation on non-coated dishes, which do not enable attachment. After incubation, dynamic and apoptotic blebbing cells were collected and centrifuged at 1100 rpm for 3 minutes. Both types of cells were resuspended and fixed in 4% paraformaldehyde/PBS for 15 minutes. After washing the pellet with PBS, cells were incubated with blocking solution containing 10% normal serum (from the same species as secondary antibody) in PBS and 0.1% Triton X-100 for 30 minutes at room temperature. Cells were washed with PBS and incubated with 1%BSA/PBS for 20 minutes at room temperature. Cells were incubated with phalloidin-Alexa 488 (Life Technologies, Grand Island, NY) or anti-tubulin- Alexa

555 (Cell Signaling Technology, Danvers, MA) for 20 minutes at room temperature. After washing all groups with PBS, nuclei were stained with 4' 6-diamidino-2-phenylindole (DAPI), and cells were imaged with a Nikon Eclipse T1 microscope equipped with Elements software. For unconjugated primary antibodies, cells were incubated with rabbit anti-ezrin antibody (Epitomics, Burlingame, CA) or rabbit anti-non-muscle myosin antibody (Sigma-Aldrich, St Louis, MO) at 4°C overnight, then washed two times the next day, and incubated with secondary antibodies conjugated with Alexa Fluorophore (goat anti-rabbit IgG secondary antibody, Alexa Fluor 594 conjugate, Sigma-Aldrich, St Louis, MO) at room temperature for 1 hour. After washing with PBS, nuclei were stained with DAPI, and cells were imaged with a Nikon Eclipse T1 with Elements deconvolution software.

Experimental Evaluation of the Cytoskeleton in Dynamic and Apoptotic Blebbing

To examine the role of the cytoskeleton in blebbing cells, single hESC, prepared as described above, were replated on Matrigel-coated 35 mm dishes containing complete mTeSR medium or drug treatments. Dishes containing dynamically blebbing single cells were immediately placed in the BioStation IM and cells were treated with either cytochalasin D (0.5 and 2μg/ml), latrunculin A (6.25 μM), swinholide A (100nM), nocodazole (1μg/ml), or blebbistatin (10μM), then incubated for live cell imaging where blebbing and attachment were followed for 4 hours at 1.5 minute intervals.

For experiments with dynamic and apoptotic cells, five fields were picked for each control and treatment group, and each experiment was repeated three times. To quantify the blebbing and attached cells during first 100 minutes of incubation in control and treated groups, cells were classified as blebbing or attached based on their

morphology and dynamic behavior. The percentage of blebbing and attached cells was counted every 20 minutes for 100 minutes. 3 or 4 videos were analyzed for each treatment and control group.

Experimental Evaluation of Different Matrixes in hESC Culture

To examine how different matrices affect dynamic blebbing and cell attachment in hESC culture. Single hESC, prepared as described above with 5,000 cell/35 mm dish, were replated on Matrigel, laminin-521 (BioLamina, Sweden, NR.) or Matrigel with laminin-111 (Sigma-Aldrich, St Louis, MO) coated 35 mm dishes containing complete mTeSR medium. Dishes containing suspended dynamically blebbing single cells were immediately placed in the BioStation IM for 4 hours and images were collected at 3 minute intervals. To quantify the blebbing and attached cells during first 60 minutes of incubation on different matrixes, cells were classified as blebbing or attached based on their morphology and dynamic behavior. The percentage of blebbing and attached cells was counted every 12 minutes for 60 minutes. 3 or 4 videos were analyzed for each group.

To determine if integrin and focal adhesion kinase (FAK) play roles in dynamic blebbing and attachment, hESC were treated with an α6 integrin function blocking antibody or FAK inhibitor 14. Cells were pre-incubated with the antibody or FAK inhibitor 14 for 1 hour, taken off their plate with Accutase, then incubated in mTeSR medium with the α6-integrin function blocking antibody or FAK inhibitor 14 in the BioStation IM where blebbing and attachment to Matrigel were imaged for 6 hours. The percentages of blebbing and attached cells were counted every 3 minutes for 60 minutes. 3 videos were analyzed in each of three independent experiments.

Statistical Analysis

GraphPad Prism (GraphPad, San Diego, CA, USA) was used for all statistical analyses. One-way analysis of variance (ANOVA) was used to find significant differences in Figure 1E insert. The percentage of dynamically blebbing and attached cells was calculated for the video data. The means and standard deviations of three experiments were compared to find significant differences. Statistical significance was evaluated using a two-way ANOVA in Figure 1F, 1G, 7A-F, 8A-B, 8F-I. Unpaired T-tests were used in Figure 2C, 3C and 8E.

RESULTS

hESCs Produced More Dynamic Blebs and Blebbed Longer than Other Cell Types

Human prostate cancer cells, mEF, mESC, and hESC were dissociated from their culture dishes, transferred to new dishes, and followed for 100 minutes in a BioStation IM. In time-lapse videos, all four types of cells underwent blebbing before attachment to their substrates (Figs. 3.1 A-D, Supplemental Movies 1-4). This was interpreted to be dynamic blebbing since cells blebbed, attached, and survived. In two-dimensional images, hESCs produced 4-11 large blebs/cell at all times before attachment, while only 1-5 large blebs/cell were observed in the other three cell types (Fig. 3.1 E). When the average number of blebs/cell was compared over all frames in each group, hESCs had significantly more blebs/cell (6/cell) than the other three cell types (1-2/cell) ($p < 0.001$) (Fig. 3.1 E insert).

The percentage of blebbing and attached cells was counted every 20 minutes for 100 minutes after plating cells on their substrates. Initially, 70% of the hESCs underwent dynamic blebbing before attachment, which was significantly more than the 10-30% observed for the other cell types ($p < 0.001$) (Fig. 3.1 F). Not only did a higher percentage of hESCs bleb initially, but hESCs continued to bleb longer than the other cells. When cells stopped blebbing, they attached and spread on their substrates (Fig. 3.1 G). hESCs were slower to attach than the other cell types, and by 100 minutes significantly fewer hESCs had attached ($p<0.001$).

Figure 3.1: Comparison of dynamic blebbing in four different cell types. All cell types produced dynamic blebs: (A) human prostate cancer cell (HU145), (B) mouse embryonic fibroblast (mEF), (C) mouse embryonic stem cell (mESC), and (D) human embryonic stem cell (hESC). (E) Number of blebs/cell in different cell types in each frame before attachment. One of three independent experiments is shown. The insert shows the number of blebs/cell averaged over all frames in all three experiments. The number of blebs/cell was significantly higher in hESC than in the other cell types by one-way ANOVA. (F, G) The percentage of blebbing cells (F) and attached cells (G) for the four cell types over 100 minutes. Videos were collected using a BioStation IM with 62 second intervals for hESC, 60 second intervals for prostate cancer cells and mEF, and 120 second intervals for mESC. The percentage of blebbing and attached cells were significantly different for hESC than for the other cell types. F and G were analyzed by two-way ANOVA. *** = $p<0.001$. (H, I) Morphological and temporal comparisons of four patterns of blebbing behavior in hESC. (H) Phase contrast images of hESC at various times in culture showing the four patterns of behavior (DB = dynamic blebbing; A = attached; AB = apoptotic blebbing; R = rounding). Dynamic blebs appear dense, while apoptotic blebs are bright. (I) Percentage of cells in each of the behavior groups shown in H over 225 minutes of incubation. Each group is based on a count of 25 cells. The average time to attachment, rounding, or apoptotic blebbing ± the standard deviation is shown. The percentage of cells in each group is given on the Y axis. (J) Gray means of dynamic blebs and apoptotic blebs were analyzed using ImageJ followed by a t-test. *** $p< 0.001$.

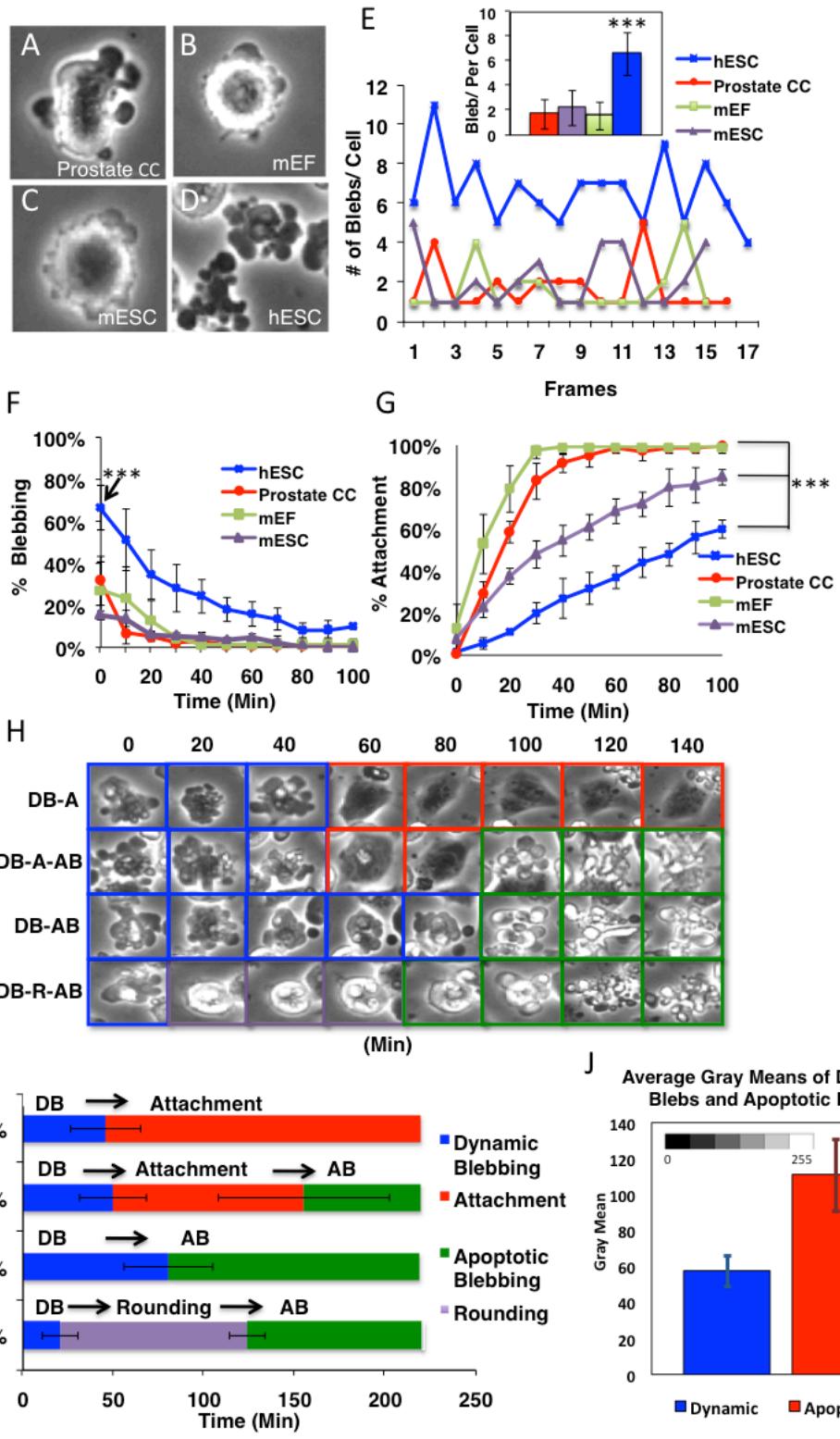
A
Prostate CC
B
mEF
C
mESC
D
hESC
E
Bleb/ Per Cell
***
hESC
Prostate CC
mEF
mESC
# of Blebs/ Cell
Frames
F
% Blebbing
***
Time (Min)
G
% Attachment
***
Time (Min)
H
DB-A
DB-A-AB
DB-AB
DB-R-AB
(Min)
I
Percentage of Cell/ Group
DB → Attachment
DB → Attachment → AB
DB → AB
DB → Rounding → AB
Dynamic Blebbing
Attachment
Apoptotic Blebbing
Rounding
Time (Min)
J
Average Gray Means of Dynamic Blebs and Apoptotic Blebs
Gray Mean
***
Dynamic
Apoptotic

Dynamic Blebbing and Apoptotic Blebbing were Morphologically and Temporally Distinct

Time-lapse videos of hESCs were collected during the first 240 minutes after plating on Matrigel (Figs. 3.1 H, I). Single hESCs exhibited four different patterns of behavior following plating. Most hESCs (70%) underwent dynamic blebbing (Fig. 3.1 H, I DB-A 0-40), then attached (Fig. 1 H, I DB-A 60-140), and remained attached for the duration of the 240-minute incubation. Some hESC (12%) underwent dynamic blebbing (Fig. 3.1 H, I DB-A-AB 0-40), attached (Fig. 3.1 H, I DB-A-AB 60-80), then detached from the substrate, and underwent apoptotic blebbing (Fig. 3.1 H, I DB-A-AB 100-140). In the third category, cells (12%) underwent dynamic blebbing (Fig. 3.1 H, I DB-AB 0-60) followed directly by apoptotic blebbing without attaching (Fig. 3.1 H, I DB-AB 80-140). In the final group, cells (5%) underwent a brief period of dynamic blebbing (Fig. 3.1 H, I DB-R-AB 0) followed by rounding (DB-R-AB 20-60), and then underwent apoptotic blebbing (DB-R-AB 80-140). In all cases, dynamic and apoptotic blebbing were well separated in time and could be distinguished morphologically. Dynamic blebbing was observed during the first hour after plating, while apoptotic blebbing, if it occurred, was observed at least 90 minutes after plating (Fig. 3.1 I). When viewed with phase contrast microscopy, dynamic blebs were generally dark, while apoptotic blebs were bright. Bleb brightness was quantified using Image J, and dynamic blebs were quantitatively darker than apoptotic blebs (Fig. 3.1 J).

To confirm the above interpretations, hESC labeled with either Mitotracker Red, which fluoresces in healthy mitochondria (Figs. 3.2 A-H) or with Magic Red, which fluoresces when caspases 3&7 are activated (Figs. 3.2 I-T). During the dynamic blebbing interval (0 - 150 minutes in Fig. 3.1 A-C), Mitotracker Red was highly

fluorescent and localized in cell bodies, not in blebs, indicating cells were healthy and that mitochondria had an intact membrane potential (Figs. 3.2 A-C and E-G). However, by 2 hours, the same cells showed diminished fluorescence, indicating damage to the mitochondria and probable loss of mitochondrial membrane potential (Figs. 3.2 D, K), which is characteristic of apoptotic cells [38]. Dynamically blebbing cells did not fluoresce when incubated with Magic Red (Figs 3.2 I-K and O-Q); however, after these cells had incubated 288 min in dishes that did not permit attachment, activated caspases 3&7 were detected, and subsequently apoptotic blebs appeared (Figs. 3.2 L-N and R-T). The data with Mitotracker Red and Magic Red confirmed that dynamically blebbing cells were not undergoing apoptosis and that cells blebbing late in the incubation interval were indeed apoptotic.

Rate of Retraction and Size Differ in Dynamic and Apoptotic Blebs

The rates of formation and retraction of dynamic and apoptotic blebs were analyzed using real time videos of cells that were freshly plated on Matrigel (dynamic blebbing) and cells that had incubated on uncoated dishes for 1.5 hours (apoptotic blebbing) (Figs. 3.2 U-W and Supplemental Movies 5 and 6). The average time for dynamic (8 seconds for 80 cells) and apoptotic (7 seconds for 69 cells) bleb formation was similar (Fig. 3.2 U). However, apoptotic blebs took significantly longer to retract (average = 64 seconds for 69 cells) than dynamic blebs (average = 22 seconds for 80 cells) (Figs. 3.2 V), and therefore the overall duration of dynamic and apoptotic blebbing was significantly different ($p < 0.0001$) (Fig. 3.2 W). In some apoptotic cells, retraction had not occurred by 6 minutes (not shown). More than 100 randomly chosen blebs were analyzed for area (microns) using ImageJ. Dynamic and apoptotic bleb size differed with dynamic blebs being generally larger than apoptotic blebs (Figs. 3. 2 X).

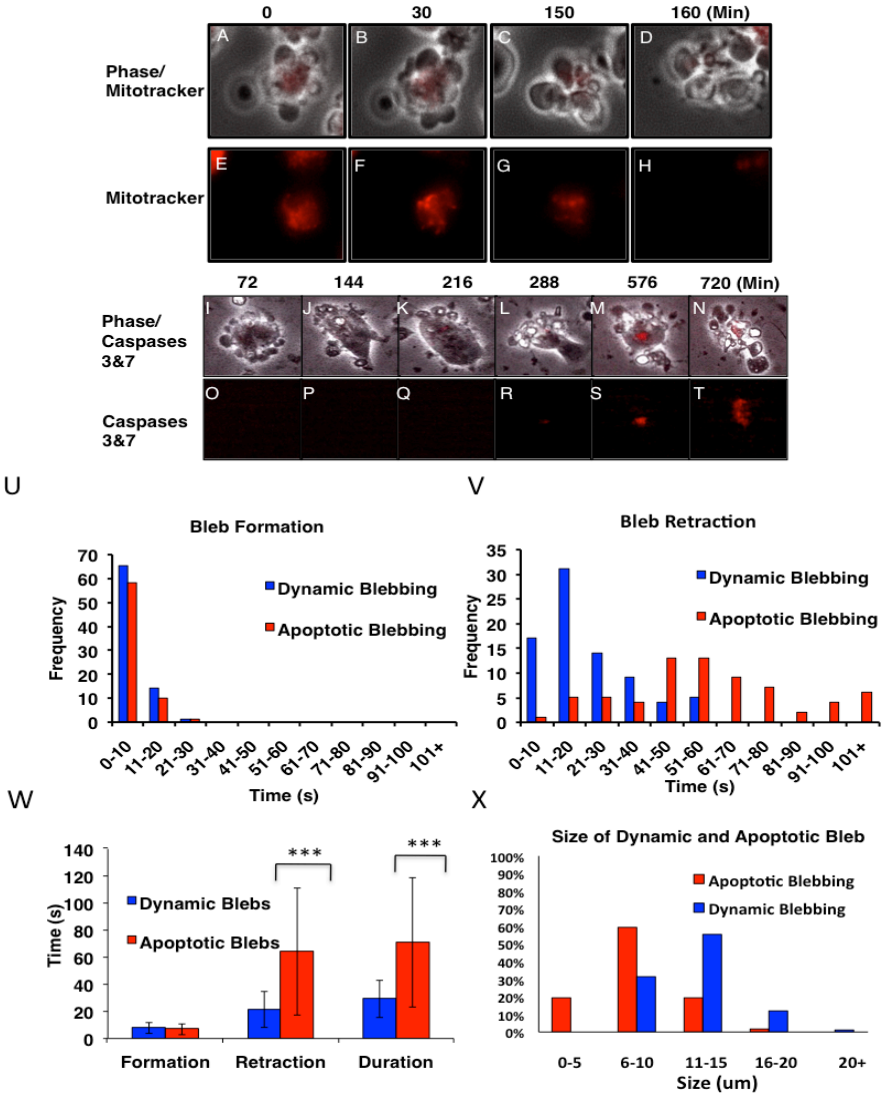

Figure 3.2: Verification of cell death and comparison of expansion and retraction times. (A-H) Phase contrast (A-D) and fluorescence images (E-H) at various times in culture showing that dynamically blebbing cells (E-G) have a strong fluorescence which is lost in apoptotic cells (H). (I-T) Phase contrast (I-N) and fluorescence images (O-T) at various times in culture showing cells preloaded with Magic Red. Dynamically blebbing and attached cells (I-J and O-P) do not show fluorescence. Cells undergoing apoptosis (L-N and R-T) have red fluorescence indicative of activation of caspase 3 & 7. (U) The frequency of dynamic and apoptotic blebs in various time intervals of bleb formation. (V) The frequency of dynamic and apoptotic blebs in various time intervals of retraction. Both frequency graphs are based on 80 dynamic and 69 apoptotic cells from three experiments. (W) Comparison of the time for formation, retraction and formation plus retraction (duration) for dynamic and apoptotic blebs. Each bar is the mean ± the standard deviation of three experiments. Groups were compared using a t-test. *** = $p < 0.001$. (X) Size comparison of dynamic and apoptotic blebs. Graph is based on 100 apoptotic and 100 dynamic cells from three different experiments.

Distribution of the Cytoskeleton During Dynamic and Apoptotic Blebbing

During formation of dynamic blebs, microtubules formed a continuous thick uninterrupted band around the cell periphery and did not extend into the blebs (Figs. 3.3 A, B). In contrast, apoptotically blebbing cells with fragmented nuclei contained depolymerized tubulin (Figs. 3.3 C, D). In dynamically blebbing cells, a cortical actin ring was present but interrupted by ruptures (arrowheads) beneath the blebs (Figs. 3.3 E, F). In contrast, most actin in the apoptotically blebbing cells was concentrated in several hot spots (arrowheads), and a cortical band of actin was not present (Figs. 3.3 G, H).

The relationship between actin and ezrin, an integral membrane protein that attaches actin filaments to the plasma membrane [39], was evaluated during bleb formation (Figs. 3.3 I - K). Ezrin was associated with the plasma membrane in non-blebbing cells (data not shown) and was localized in the plasma membrane of both dynamic and apoptotic blebs (Fig. 3.3 M, O). Expanding dynamic bleb membranes either lacked associated actin (Fig. 3.3 N arrowhead 1) or had a continuous band of actin subjacent to the bleb membrane (Fig. 3.3 N arrowhead 2). A similar distribution of actin was seen in apoptotic blebs. Some apoptotic cells lacked actin beneath the bleb membranes (Fig. 3.3 P arrowhead 1), while others had actin associated with blebs (Fig. 3.3 P arrowhead 2). These data suggest that actin moves into the blebs and reassembles into filaments after expansion.

During retraction, actin and myosin localization differed in dynamic and apoptotically blebbing cells (Figs. 3.4 A-L). In dynamically blebbing cells, small retracting blebs had intense actin labeling adjacent to the bleb membrane (Figs. 3.4 A, B). In apoptotically blebbing cells, actin was sometimes observed adjacent to bleb membranes, but was often fragmented and formed hot spots (Figs. 3.4 C, D). In dynamic

blebs, myosin was diffuse in forming blebs (Figs. 3.4 E, F, I, J), but was reassembled with actin under membranes in small retracting blebs (Figs. 3.4 B, I, J). In late stages of apoptosis when nuclei were highly fragmented, cells had little myosin staining (Figs. 3.4 G, H, K, L).

The preceding data demonstrate that dynamic and apoptotic blebbing are two distinct processes that occur during plating of hESC. These types of blebbing were further investigated in the following experiments using drugs that affect the cytoskeleton.

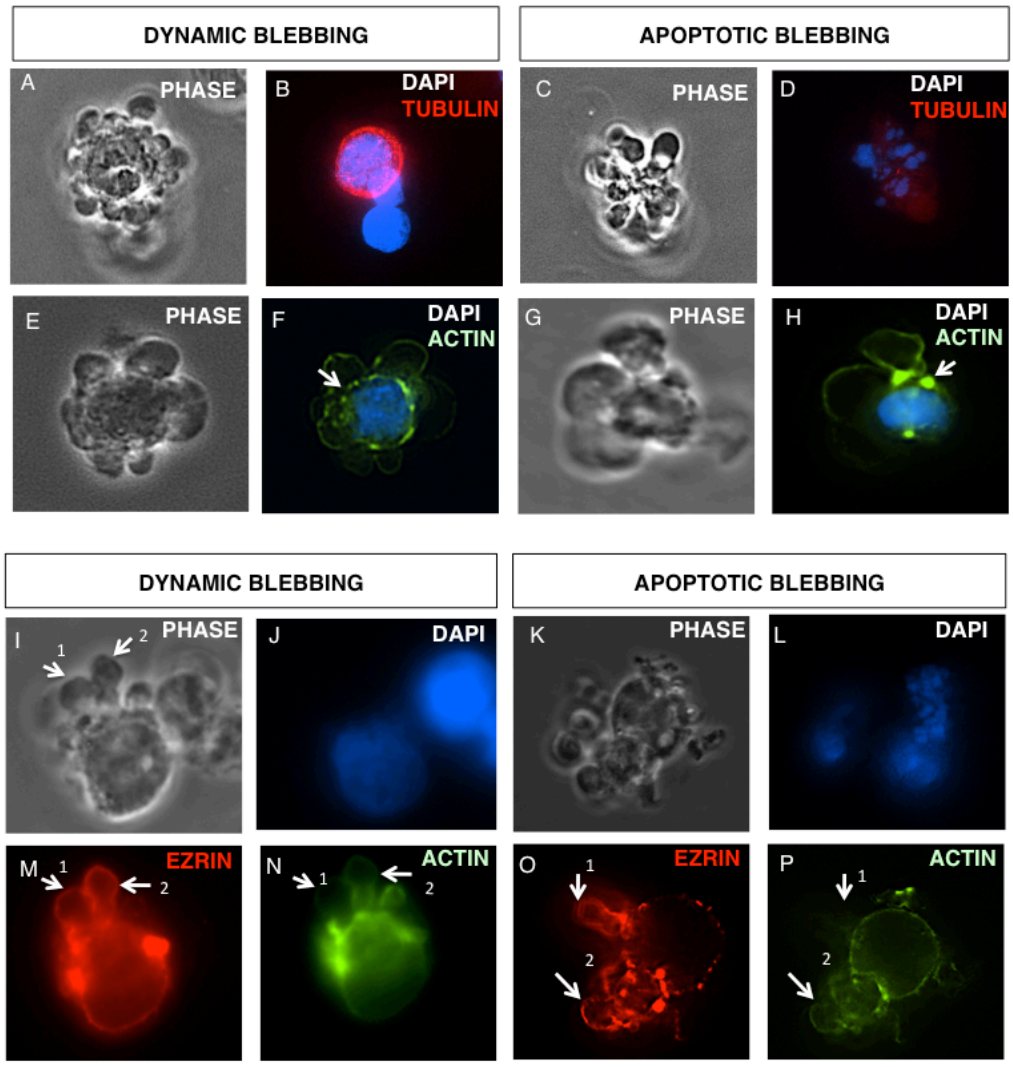

Figure 3.3: Distribution of the tubulin, actin and ezrin during bleb formation in dynamic and apoptotically blebbing cells. (A-D) Phase and fluorescent micrographs showing the distribution of microtubules in dynamic (A, B) and apoptotic blebs (C, D). (E-H) Phase and fluorescence micrographs showing the distribution of actin filaments in dynamic (E, F) or apoptotic blebs (G, H) during bleb formation. Arrows indicate breaks in the cortical actin ring of dynamically blebbing cells (F) or hot spots of depolymerized actin filaments in apoptotically blebbing cells (H). (I-P) Phase and fluorescent micrographs showing the localization of ezrin and actin in expanding dynamic blebs (I, J, M, N) and apoptotic blebs (K, L, O, P).

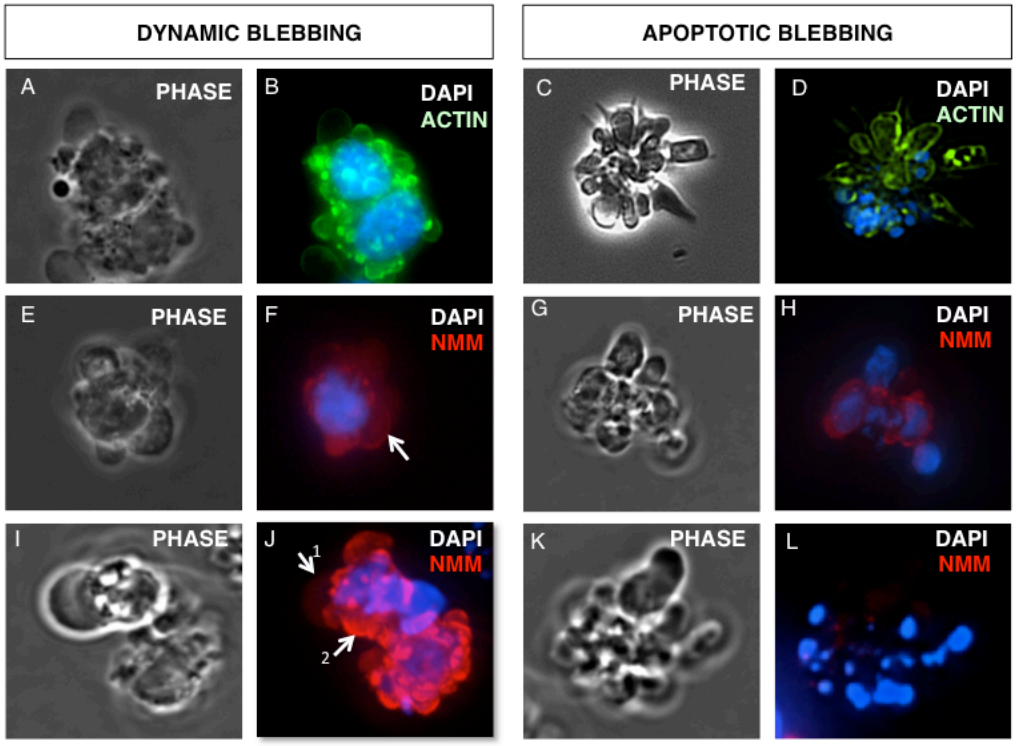

Figure 3.4: Distribution of the actin and non-muscle myosin in dynamic and apoptotically blebbing cells. (A, B) Phase and fluorescent micrographs showing the distribution of actin in retracting dynamic blebs. (C, D) Phase and fluorescent micrographs showing the distribution of actin in late apoptotic blebs. (E, F, I, J) Phase and fluorescent micrographs showing the distribution of non-muscle myosin II in non-retracting dynamic blebs (E, F) or retracting blebs (I, J). (G, H, K, L) Phase and fluorescent micrographs showing the distribution of non-muscle myosin II in early (G, H) and late apoptotic blebs (K, L).

Nocodazole Prolonged Dynamic Blebbing and Inhibited Attachment

To determine if microtubules played a role in dynamic blebbing and attachment, cells were treated with 1μg/ml of nocodazole, which depolymerized microtubules (Supplemental Fig. 1 A-L). BioStation time-lapse video data showed that blebbing control cells began attaching by 20 minutes of incubation, while nocodazole treated cells were still dynamically blebbing by 60 minutes (Fig. 3.5 A, B). In quantified video data, there were significantly more ($p < 0.001$) dynamically blebbing cells in the nocodazole

treated group than in the control at 20 minutes of incubation (Fig. 3.5 A). In addition, blebbing was prolonged by nocodazole, and by 180 minutes most treated cells were still dynamically blebbing ($p < 0.001$ for control vs. treated at 180 minutes) (Fig. 3.5 A). Dynamically blebbing cells failed to attach to the Matrigel substrate (Fig. 3.5 B).

Cytochalasin D and Blebbistatin Inhibited Dynamic Blebbing in hESC

To determine if fragmentation of actin filaments affected dynamic blebbing, cells were treated with cytochalasin D (2μg/ml) (Fig 3.5 C), latrunculin A (6.25 μM) or swinholide A (100 nM) (Supplemental Figs. 3.1 E-L), then incubated in a BioStation IM where blebbing and attachment to Matrigel were imaged for 6 hours. Cytochalasin D (2 μg/ml), latrunculin A, and swinholide A depolymerized actin filaments, resulting in numerous actin hot spots (Supplemental Figs. 1 E-L). Dynamic blebbing was completely inhibited by cytochalasin D; cells remained round with few or no blebs and did not attach (Fig. 3.5 D). Quantification of the video data showed that cytochalasin D inhibited both dynamic bleb formation and cell attachment (Figs. 3.5 C-D). Inhibition of bleb formation by cytochalasin D was dose dependent (Supplemental Fig. 3.2 G). 0.5μg/ml of cytochalasin D enabled some cells to form blebs, which did not retract, while 2μg/ml completely inhibited bleb formation (Supplemental Fig. 3.2 G). Attachment was also completely inhibited by the higher dose, and partially inhibited by 0.5μg/ml of cytochalasin D.

To determine if myosin was likewise involved in dynamic blebbing, cells were treated with blebbistatin, a myosin II inhibitor (Figs. 3.5 E, F). None of the cells underwent dynamic blebbing after treatment with blebbistatin, and cells attached to the substrate soon after plating (Figs. 3.5 E, F).

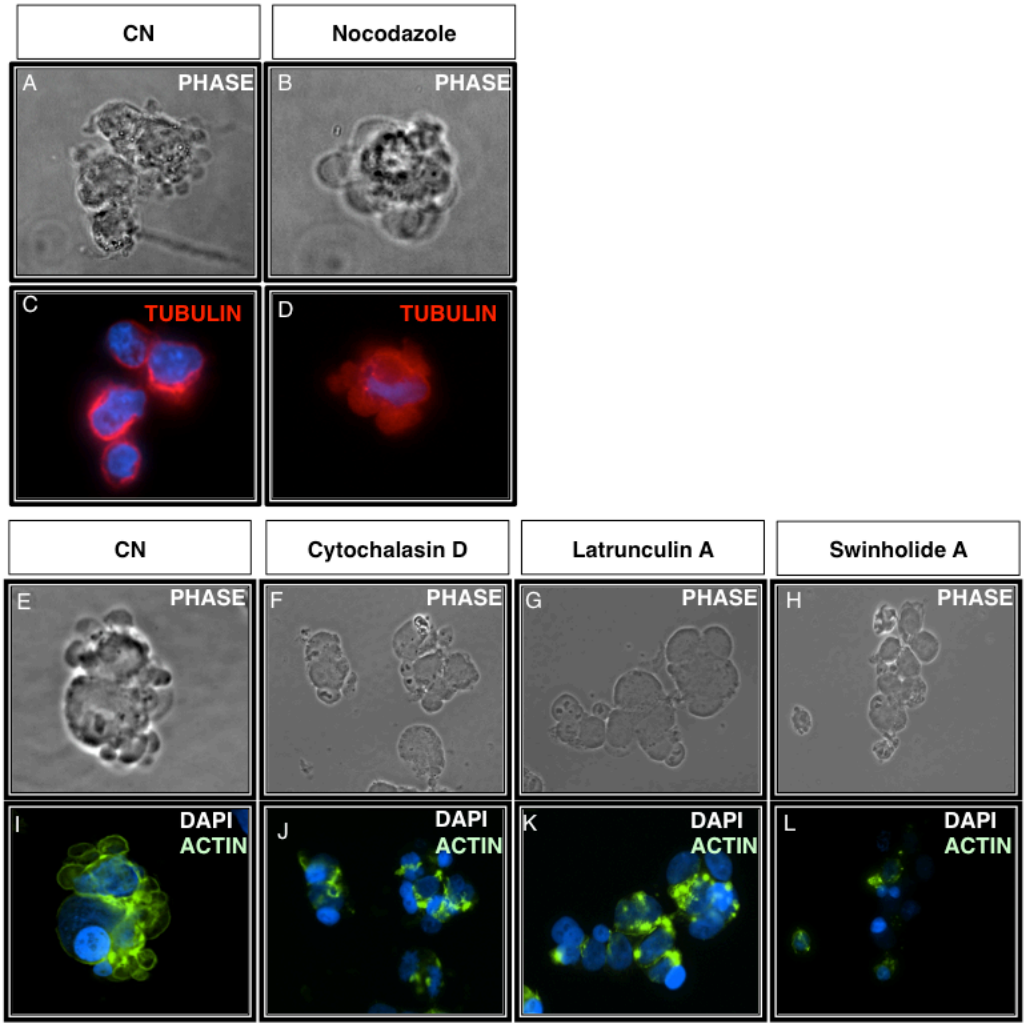

Supplemental Figure 3.1: Data showing that cytoskeletal drugs were effective. : (A-D) Phase contrast (A-B) and fluorescent images (C-D) of hESC showing that 1μg/ml nocodazole depolymerizes microtubules. (E-L) Phase contrast (E-H) and fluorescent images (I-L) of hESC showing that different actin filament depolymerizers were effective. (E, I) Control, (F, J) 1μg/ml cytochalasin D, (G, K) latrunculin A, and (H, L) swinholide A).

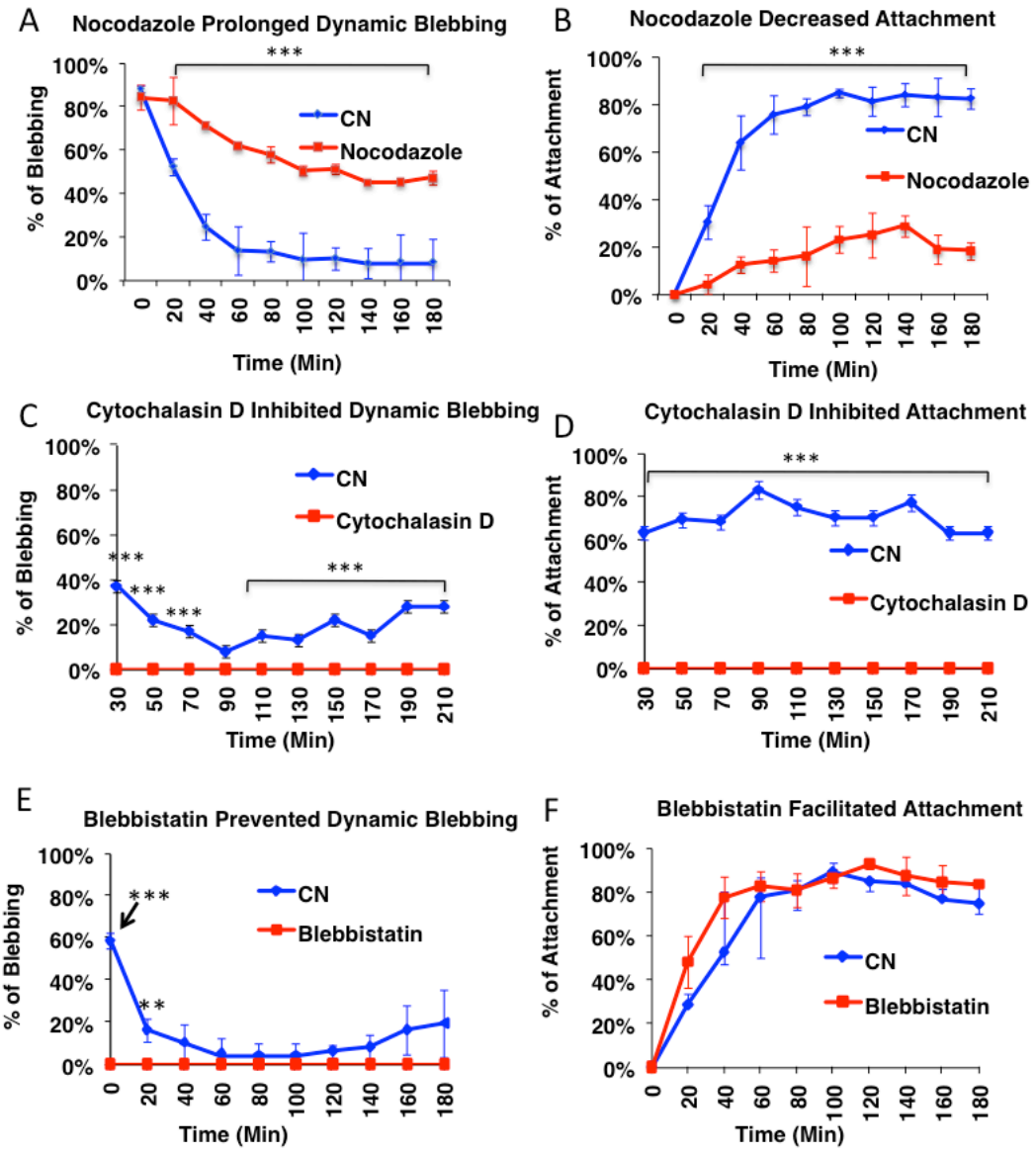

Figure 3.5: The effect of cytoskeletal drugs on dynamically blebbing cells: (A, B) 1μg/ml nocodazole prolonged dynamic blebbing (A) and inhibited attachment (B) in hESC. (C, D) 2μg/ml Cytochalasin D inhibited both dynamic blebbing (C) and attachment (D) in hESC. (E, F) 10μM blebbistatin inhibited dynamic blebbing (E) and accelerated attachment (F) in hESC. Each point is the mean of three experiments ± the standard deviation of three experiments. All data were analyzed by a 2-way ANOVA. * $p < 0.05$; *** $p < 0.001$.

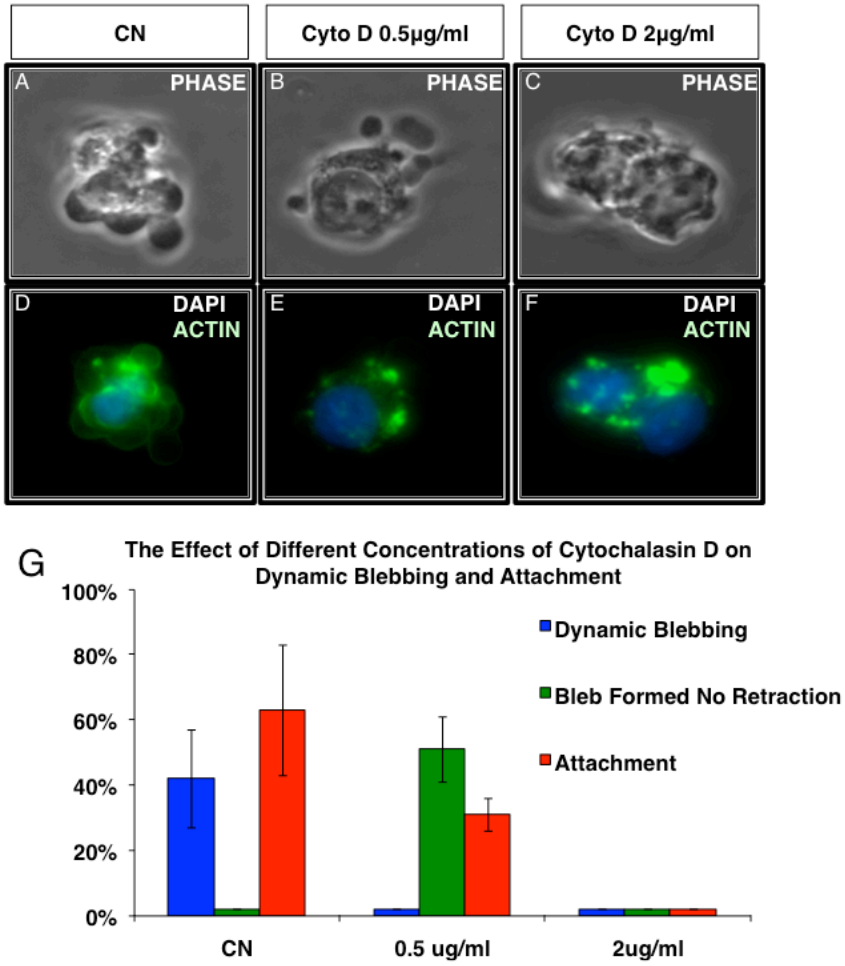

Supplemental Figure 3.2: hESC treated with 0.5μg/ml and 2μg/ml of cytochalasin D. (A-F) Phase contrast (A-C) and fluorescent images showing actin and DAPI staining (D-F). (G) Cells treated with 0.5μg/ml and 2μg/ml of cytochalasin D then imaged in a BioStation IM. Three endpoints were analyzed in the videos: dynamically blebbing cells, attached cells, and cells with non-retracting blebs.

Laminin-521 Inhibited Dynamic Blebbing, Accelerated Cell Attachment, and Reduced Apoptosis

To improve plating efficiency and hESC survival, we sought a safe non-invasive method that did not rely on xenobiotics or inhibitors to diminish or reverse dynamic

blebbing and promote cell attachment. To do this, we evaluated dynamic blebbing and attachment on different matrices that are used for hESC culture. Dynamic blebbing was significantly inhibited and cell attachment was accelerated when cells were plated on recombinant laminin-521 (Figs. 3.6 A, B). Because Matrigel contains laminin-111 [40], we also tested cells plated on Matrigel over-coated with additional laminin-111. The combination of laminin-111 and Matrigel also significantly reduced dynamic blebbing and accelerated attachment, although this combination was not as efficient as laminin-521 alone (Figs. 3.6 A, B). Individual cells were monitored in the videos, and apoptotic cells were identified and counted based on their morphology (Figs. 3.6 C, D). Apoptotically dying cells have bright blebs with slow retraction times. Cells plated on laminin-521 had significantly fewer apoptotic cells than the group plated on Matrigel (Fig. 3.6 E).

We next investigated the hypothesis that binding of hESC to laminin activates signaling through an integrin and FAK which shuts down dynamic blebbing. Cells were pre-incubated with an α6-integrin function blocking antibody for 1 hour, taken off the plate with Accutase, then incubated in media containing the α6 integrin-function blocking antibody and imaged in BioStation IM for 6 hours. Dynamic blebbing was not significantly affected by the integrin α6-function blocking antibody (Fig. 3.6 F). However, cell attachment was significantly inhibited (Fig. 3.6 G) and 56% of cells were rounded after 1 hour in α6-integrin-function blocking antibody (Supplemental Fig. 3.3).

To determine if integrin signaled through a FAK, cells were pre-incubated with a FAK inhibitor for 1 hour, taken off the plate with Accutase, and incubated with the inhibitor in the BioStation IM where blebbing and attachment to Matrigel were imaged for 6 hours. Quantification of the video data showed that FAK inhibitor prolonged dynamic bleb and slowed cell attachment (Figs. 3.6 H, I).

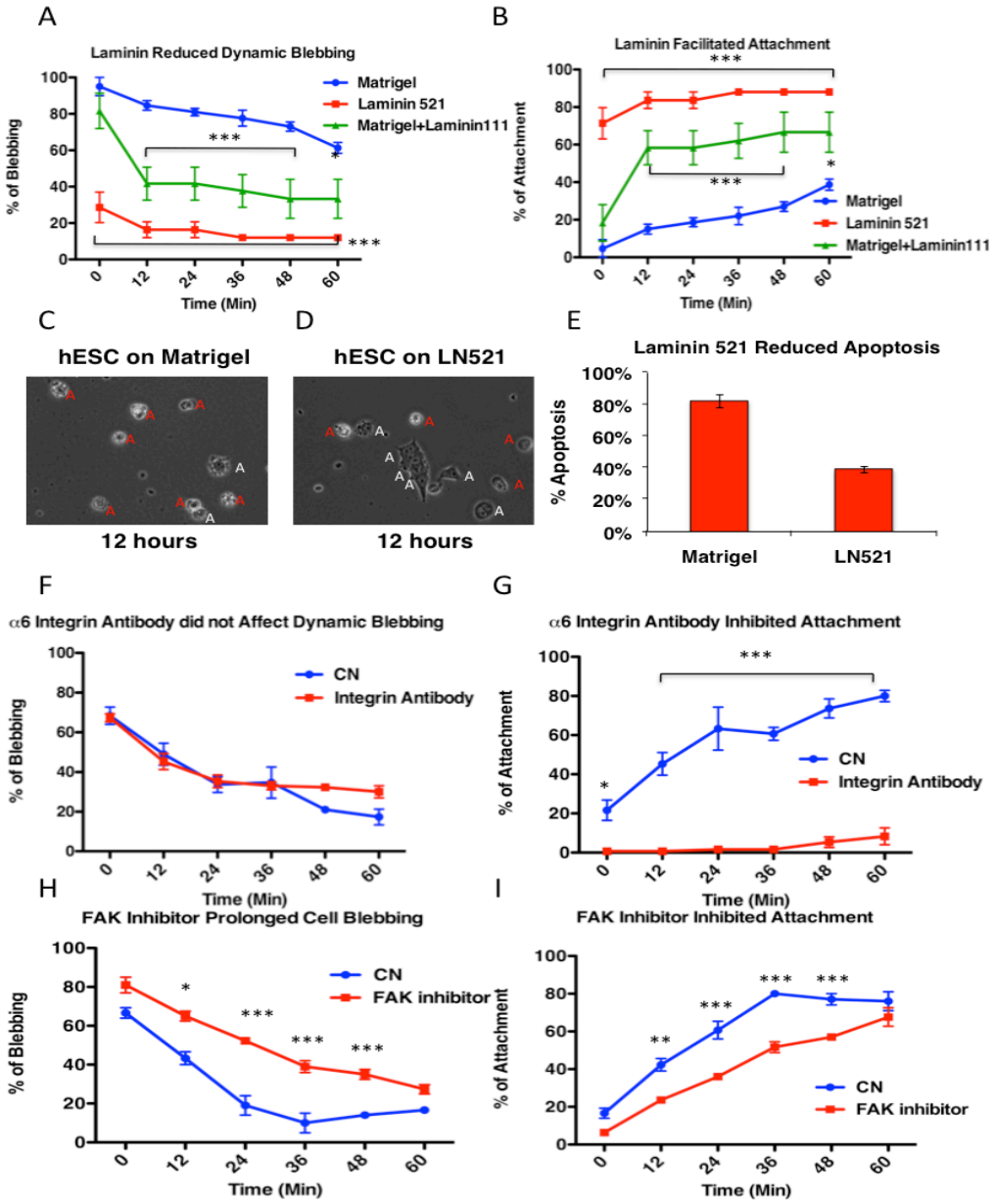

Figure 3.6: Laminin, integrin, and FAK signaling reduces dynamic blebbing and increases cell attachment/survival. (A, B) Laminin-521 and Matrigel with laminin-111 inhibited dynamic blebbing (A) and accelerated attachment (B) in hESC. (C, D) Phase images of hESC on Matrigel (C) and laminin 521 (D). Red "A"s show apoptotic blebbing/apoptotic cells; white "A"s show attached cells. (E) Quantitative data from the videos showed the percentage of apoptotic cells on Matrigel and laminin-521. Each bar is the mean of three experiments ± the standard deviation. (F, G) α6- Integrin antibody did not affect dynamic blebbing (F) but inhibited attachment (G) in hESC. (H, I) FAK inhibitor prolonged dynamic blebbing (H) and inhibited attachment (I) in hESC. Graphical data were analyzed by 2-way ANOVA. Each point is the mean ± standard deviation of three experiments. * $p < 0.05$; ** $p < 0.01$; *** $p < 0.001$.

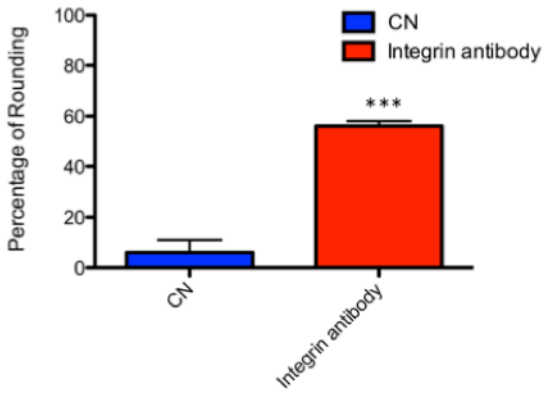

Supplemental Figure 3.3: Function blocking antibody to α6 integrin prevents cell attachment and leads to rounding of most cells. Mean and standard deviation of three experiments. Data were compared using at-test. *** $p < 0.001$

DISCUSSION

A distinction between dynamic and apoptotic blebbing has not been made previously in freshly plated hESC. Dynamic and apoptotic blebbing were well separated in time, and also differed in their rates of retraction, bleb intensity, assembly of cytoskeletal proteins, distribution of organelles during blebbing, and their response to chemicals that affect the cytoskeleton. During passaging onto Matrigel, hESC underwent prolonged dynamic blebbing that inhibited attachment and spreading and appeared to stress the cells. Typically, dynamic blebbing subsided within an hour of plating allowing cell attachment and spreading to occur. hESC that failed to attach, eventually underwent apoptotic blebbing and died. These data demonstrate that dynamic blebbing is a critical factor that decreases efficient passaging hESC and

precludes passaging of single cells. Gaining control of dynamic blebbing would be useful in hESC research and in the application of hESC therapies to patients.

Figure 3.7 summarizes our data comparing dynamic and apoptotic blebbing in freshly plated hESC. When bundles of cortical actin became thin, the plasma membrane detached from the actin and blebs formed. During bleb expansion, ezrin remained associated with the bleb membrane, and actin was not attached to ezrin at this time. As the bleb expanded, actin moved into the bleb, attached to ezrin, and reassembled under the bleb membrane. In dynamic blebbing, myosin reassembled with actin in the bleb, and their contraction causes bleb retraction. In apoptotic blebs, actin and myosin were fragmented, less abundant, or absent, which may account for their slower retraction. Depolymerizing microtubules prolonged dynamic blebbing and inhibited attachment. Use of blebbistatin or plating on laminin 521 or 111 decreased dynamic blebbing and facilitated cell attachment.

The preceding observations raise two questions about dynamic blebbing. What is the significance of dynamic blebbing and why does it occur so vigorously in hESC? Cells dissociated from amphibian embryos can migrate using bleb-like protrusions [41,42,43], and live zebrafish have primordial germ cells that use blebs to migrate [44,45,46,47]. Similar observations have been made in primordial germ cells from Drosophila melanogaster embryos [48]. These findings suggest that dynamic blebbing is widely used for cell migration and further suggest that dynamic blebbing may be a common mechanism for generating motility in embryonic cells.

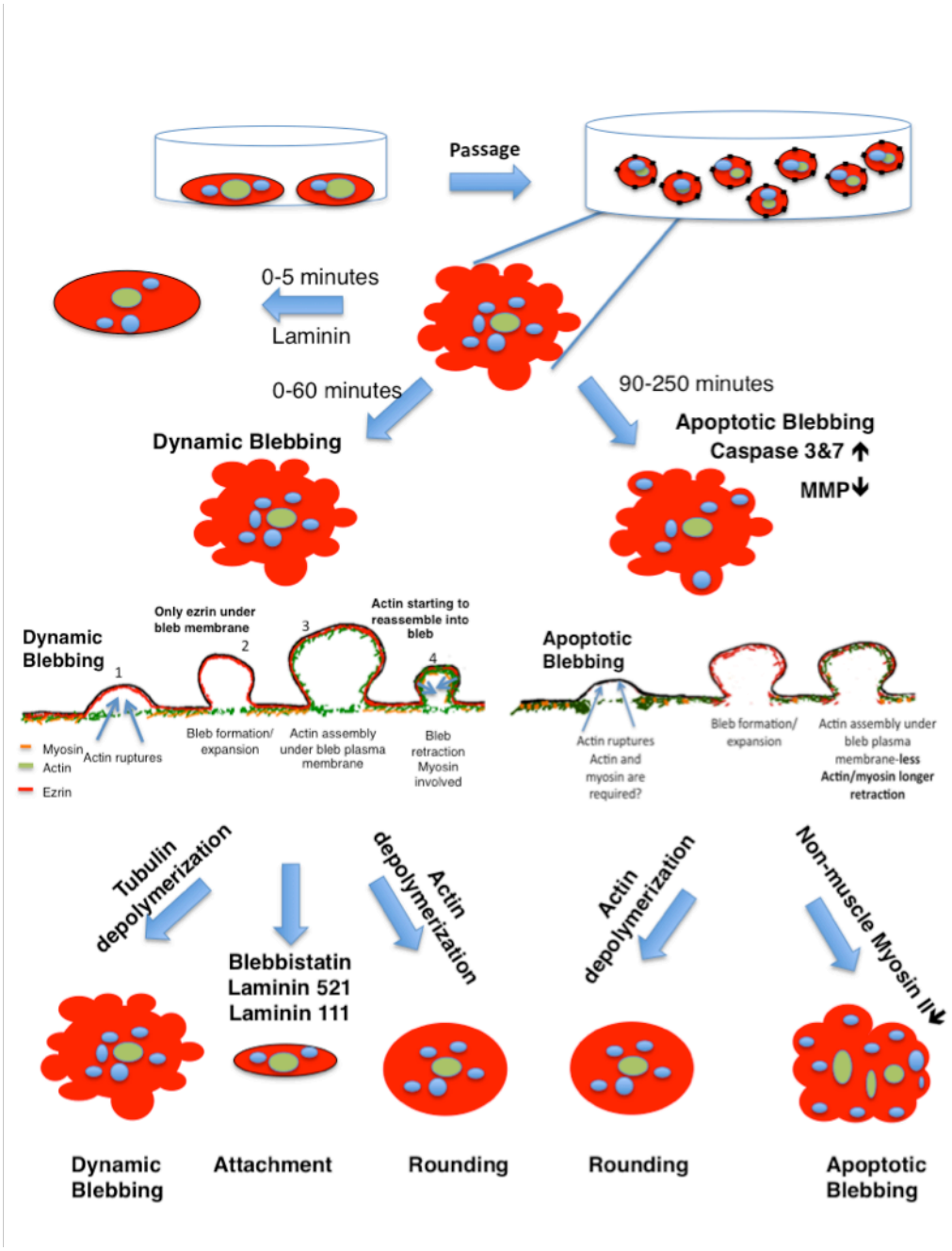

Figure 3.7: Schematic summarizing data**.** Diagram comparing dynamic and apoptotic blebbing in hESC and summarizing the main findings of the study.

Many cells undergo dynamic blebbing during plating, but hESCs are unusual in producing more blebs for a longer time than the other cell types we tested. When cultured *in vitro*, hESC behave like epiblast cells, a highly motile epithelialized type of embryonic cell [26,49]. During weeks 2 and 3 of human development, sheets of epiblast cells undergo extensive migration, and during gastrulation, they enter the primitive streak, pinch off of the groove, and migrate as single cells to form both the endoderm and mesoderm [50]. It has been suggested that hESC blebbing is driven by hyperactivity of the ROCK/myosin system [21,26]. It is possible that in embryos dynamic blebbing provides motility to epiblast cells during gastrulation. In contrast, mESC, which resemble the inner cell mass, did not undergo extensive blebbing (Fig 1A), indicating that earlier stages in development have a less active cytoskeleton.

Dynamic blebbing has important consequences for cultured hESC. First, cells that are dynamically blebbing cannot attach to their matrix until blebbing stops. Secondly, cells that are dynamically blebbing appear stressed and often shed part of their cytoplasm. Therefore, factors that reduce dynamic blebbing and accelerate attachment would benefit hESC culture. ROCKi (Y27632) is often used to help hESC attach and spread rapidly; however, ROCKi treated cells often appear stringy and stressed [22]. Furthermore, 20μM ROCKi can promote the differentiation of mESC into motor and sensory neurons [51]. ROCKi may produce other unwanted off-target effects that are not desirable when cells are being prepared for research, translational, or clinical use. Blebbistatin is also used to accelerate attachment by inhibiting myosin II, but again it is not a normal additive to culture media, and it may affect processes in addition to blebbing, such as cytokinesis [52]. We showed that plating hESC on laminin-521, a biological molecule found in the inner cell mass [53], signals through an integrin-FAK

pathway to stop dynamic blebbing and accelerate attachment. For hESC culture, plating on laminin-521 or Matrigel with laminin-111 improves cell attachment and survival by reducing dynamic blebbing and enables efficient plating of single cells, while concurrently incubating in conditions that resemble the cells' natural *in vivo* environment without inhibitors that may have unwanted effects.

REFERENCES

1. Thomson JA, Itskovitz-Eldor J, Shapiro SS, et al. Embryonic stem cell lines derived from human blastocysts. Science 1998;282:1145–1147.

2. Martin GR. Isolation of a pluripotent cell line from early mouse embryos cultured in medium conditioned by teratocarcinoma stem cells. Proc. Natl Acad. Sci. USA. 1981;78:7634–7638.

3. Evans MJ, Kaufman MH. Establishment in culture of pluripotent cells from mouse embryos. Nature 1981;292:154–156.

4. Xu C, Inokuma MS, Denham J, et al, Feeder-free growth of undifferentiated human embryonic stem cells, Nat Biotechnol, 2001:19:971.

5. Ludwig TE, Levenstein ME, Jones JM, et al. Derivation of human embryonic stem cells in defined conditions. Nat Biotechnol 2006:24(2):185-187.

6. Ludwig TE, Bergendahl V, Levenstein ME, et al. Feeder-independent culture of human embryonic stem cells. Nat Methods 2006:3(8):627-646.

7. McElroy SL, Reijo Pera RA, Culturing human embryonic stem cells in feeder-free conditions. Cold Spring Harbor Protocols 2008.

8. Coleman ML, Sahai EA, Yeo M, et al. Membrane blebbing during apoptosis results from caspase-mediated activation of ROCK i. Nature cell biology 2011:3(4):339-345.

9. Cocca BA, Cline AM, Radic MZ. Blebs and apoptotic bodies are B cell autoantigens. J Immunol 2002:169:159-166.

10. Barros LF, Kanaseki T, Sabirov R, et al. Apoptotic and necrotic blebs in epithelial cells display similar neck diameters but different kinase dependency. Cell Death Differ 2003:10(6):687-697.

11. Charras GT and Paluch, E. Blebs lead the way: how to migrate without lamellipodia Nat. Rev. Mol. Cell Biol. 2008:9:730-736.

12. Charras GT. A short history of blebbing. Journal of Microscopy, 2008:231:466-478.

13. Boss J. Mitosis in cultures of newt tissues. IV. The cell surface in late anaphase and the movements of ribonucleoprotein. Exp. Cell Res. 1955: 8:181–187.

14. Porter K, Prescott D, Frye J. Changes in surface morphology of Chinese hamster ovary cells during the cell cycle. J. Cell Biol. 1973:57:815–836.

15. Fishkind DJ, Cao LG, Wang YL. Microinjection of the catalytic fragment of myosin light chain kinase into dividing cells: effects on mitosis and cytokinesis. J. Cell Biol. 1991:114:967–975.

16. Boucrot E, Kirchhausen T. Endosomal recycling controls plasma membrane area during mitosis. Proc. Natl. Acad. Sci. U.S.A. 2007:104:7939–7944.

17. Hickson GRX. Echard A. O'Farrell PH. RHO kinase controls cell shape changes during cytokinesis. Curr Biol. 2006:16(4): 359-370.

18. Charras GT, Hu CK, Coughlin M, et al. Reassembly of contractile actin cortex in cell blebs. J. Cell. Biol. 2006:175:477-490.

19. Tokumitsu T. Maramorosch K. Cytoplasmic protrusions in insect cells during mitosis in vitro. J Cell Biol. 1967:34(2):677-683.

20. Khajah MA and Luqmani YA. Involvement of membrane blebbing in immunological disorders and cancer. Medical Principles and Practice 2015:25 Supplement 2: 1-10.

21. Ohgushi M, Matsumura M, Eiraku M, et al. Molecular Pathway and Cell State Responsible for Dissociation-Induced Apoptosis in Human Pluripotent Stem Cells, Cell Stem Cell 2010:6:7(2):225-239.

22. Weng N J-H, Phandthong R, Talbot P. A video bioinformatics method to quantify cell spreading and its application to cells treated with Rho-associated protein kinase and blebbistatin. Video Bioinformatics Editors B. Bhanu and P. Talbot. Springer, 2015.

23. Guan BX, Bhanu B, Thakoor NS, et al. Automatic cell region detection by k-means with weighted entropy. 10th International Symposium Biomedical Imaging (ISBI) 2013:418-421.

24. Guan BX, Bhanu B, Talbot P, et al. Extraction of blebs in human embryonic stem cell videos. IEEE Transactions on Computational Biology and Bioinformatics 2015a:99.

25. Guan B, Bhanu B, Talbot P, et al. Bio-inspired segmentation and detection methods for human embryonic stem cells. In: Video Bioinformatics: From Live Imaging to Knowledge. Eds B. Bhanu and P. Talbot, Springer International Publishing Switzerland 2015b:7:135-150.

26. Ohgushi M, Sasai Y. Lonely death dance of human pluripotent stem cells: ROCKing between metastable cell states. Trends Cell Bio. 2011:21(5):274-282.

27. Watanabe K, Ueno M, Kamiya D, et al. A ROCK inhibitor permits survival of dissociated human embryonic stem cells. Nat Biotechnol 2007:25(6):681-6.

28. Harb N, Archer TL, Sato N. The Rho-Rock-Myosin signaling axis determines cell-cell integrity of self-renewing pluripotent stem cells. PLOS ONE 2008:3: e3001.

29. Krawetz RJ, Li X, Rancourt DE. Human embryonic stem cell: caught between a ROCK inhibitor and a hard place. BioEssays 2009:31:336-343.

30. Fujimura M, Usuki F, Kawamura M, et al. Inhibition of the RHO/ROCK pathway prevents neuronal degeneration in vitro and in vivo following methylmercury exposure. Toxicol Appl Phamacol 2011:250(1):1-9.

31. Lin S. and Talbot P. Methods for culturing mouse and human embryonic stem cells. Methods Mol Biol 2011;690:31-56.

32. Behar RZ, Bahl V, Wang Y, et al. A method for rapid dose-response screening of environmental chemicals using human embryonic stem cells. J. Pharmacological Toxicological Methods. 2012a:66(3):238-45.

33. Behar RZ, Bahl V, Wang Y, et al. Adaptation of Stem Cells to 96-Well Plate Assays: Use of Human Embryonic and Mouse Neural Stem Cells in the MTT Assay. Current Protocols in Stem Cell Biology 2012b:1:1C.13.

34. Lin S, Tran V, Talbot P. Comparison of Toxicity of Smoke from Traditional and Harm Reduction Cigarettes Using Mouse Embryonic Stem Cells as a Novel Model for Preimplantation Development. Hu Rep. 2009:24(2): 386-397.

35. Wang Lei, Alcon A, Yuan H, et al. Cellular and Molecular Mechanisms of Pomegranate Juice-Induced Anti-Metastatic Effect on Prostate Cancer Cells. Integrative Biology 2011:3: 742-754.

36. Talbot P, zur Nieden N, Lin S, et al. Use of video bioinformatics tools in stem cell biology. In: Handbook of Nanotoxicology, Nanomedicine and Stem Cell Use in

Toxicology, Eds: S. Sahu and D. Casciano, John Wiley, West Sussex, United Kingdom. 2014:379-402.

37. Lin S, Yip H, Phandthong R, et al. Evaluation of cell behavior and health using video bioinformatics tools. In: Video Bioinformatics: From Live Imaging to Knowledge. Eds B. Bhanu and P. Talbot Springer International Publishing Switzerland 2015:9:167-186.

38. Gottlieb E, Armour SM, Harris MH, et al. Mitochondrial membrane potential regulates matrix configuration and cytochrome c release during apoptosis. Cell Death and Differentiation 2003:10:709-717.

39. Solinet S, Mahmud K, Stewman SF, et al., The actin-binding ERM protein moesin binds to and stabilizes microtubules at the cell cortex. The Journal of Cell Biology 2013:22:202(2):251-260.

40. Hughes CS, Postovit LM, Lajoie GA. "Matrigel: a complex protein mixture required for optimal growth of cell culture". Proteomics 2010:10(9):1886–90.

41. Holtfreter J. Properties and functions of the surface coat in amphibian embryos. J. Exp. Zool. 1943:93:251-323.

42. Kubota KY. Creeping locomotion of the endodermal cells dissociated from gastrulae of the Japanese newt, Cynops pyrrhogaster. Exp. Cell Res. 1981:133:137-148.

43. Satoh N, Kageyama T, Sirakami KT. Motility of siddociated embryonic cells in Xenopus laevis: its significance to morphogenetic movements. Dev. Growth Diff. 1976:18:55-67.

44. Blaser H, Reichman-Fried M, Castanon I, et al. Migration of zebrafish primordial germ cells: a role for myosin contraction and cytoplasmic flow. Dev. Cell 2006:11:613-627.

45. Trinkaus JP. Surface activity and locomotion of *Fundulus* deep cells during blastula and gastrula stages. Dev. Biol. 1972:30:69-103.

46. Wourms JP. The developmental biology of annual fishes. II. Naturally occurring dispersion and reaggregation of blastomers during the development of annual fish eggs. J. Exp. 1972:182:169-200.

47. Trinkaus JP. Ingression during early gastrulation of Fundulus. Dev. Biol. 1996:177:356-370.

48. Jaglarz MK, Howard KR. The active migration of Drosophila primordial germ cells. Dev. 1995:121:3495-3503.

49. Nichols J, Smith A. Pluripotency in the embryo and in culture. Cold Spring Harbor Perspectives in Biology 2012:4:a008128.

50. Moore KL. The Developing Human, 10th Edition Clinically Oriented Embryology Elsevier 2016.

51. Kamishibahara Y, Kawaguchi H, Shimizu N. Promotion of mouse embryonic stem cell differentiation by Rho kinase inhibitor Y-27632. Neurosci Lett. 2014:579:58-63.

52. Guha M, Zhou M, Wang Y-L. Cortical actin turnover during cytokinesis requires myosin II. Current Biology 2005:15:8:732-736.

53. Schilperoort-Haun KR, Menino AR Jr. Evaluation of extracellular matrix proteins and tissue inhibitor of matrix metalloproteinase's-2 on bovine inner cell mass outgrowth in vitro. In Vitro Cell Dev Biol Anim 2002:28(1):41-47.

Chapter 4

The P2X7 Receptor Is an Upstream Regulator of Dynamic Blebbing and a Pluripoteny Marker in Human Embryonic Stem Cells

Nikki Jo-Hao Weng[a,b] and Prue Talbot[a,b]

[a]Department of Cell Biology and Neuroscience, University of California, Riverside, California, USA 92521

[b]Cell Molecular and Developmental Biology Graduate Program, University of California, Riverside, California, USA 92521

Authors contributions:

NW: Concept and design, collection and assembly of data, data analysis and interpretation, manuscript writing

PT: Concept and design, assembly of data, data analysis and interpretation, manuscript writing, financial support, final approval of manuscript

Corresponding author: Prue Talbot, PhD., Department of Cell Biology & Neuroscience, University of California, Riverside CA. 92521 951-827-3768 phone; 951-827-4207 FAX; talbot@ucr.edu

The authors have no conflicts of interest to acknowledge.

Grant support: This work was supported by the California Institute for Regenerative Medicine Core Grant #CL1-00508, an NSF IGERT grant on Video Bioinformatics # DGE-093667, and grants from the Academic Senate.

Running title: P2X7 regulates blebbing in hESC

Abstract

Dynamic blebbing occurs during passaging of pluripotent stem cells and inhibits cell attachment and survival. New methods are needed to reduce blebbing during passaging. Our purpose was to test the hypotheses that the P2X7 receptor, which is activated by extracellular ATP during passaging, initiates dynamic blebbing. The P2X7 receptor was found in human embryonic stem cells (hESC) using PCR and immunocytochemistry, but not in differentiating cells. Extracellular ATP concentrations were 14 x higher in medium during passaging. Addition of ATP to culture medium prolonged dynamic blebbing and inhibited attachment. Inhibition of P2X7 by specific drugs or by siRNA greatly reduced dynamic blebbing and improved cell attachment. Because P2X7 is a calcium channel, cells were incubated in calcium chelators (EGTA or BAPTA) and blebbing was reduced and attachment improved. Calcium influx was observed using Fura-4 when ATP was added to culture medium and inhibited in the presence of the P2X7 inhibitor. ROCK inhibitors, which we found inhibit dynamic blebbing, are widely used to help cell attachment during passaging. Because Rac often counteracts the ROCK pathway, we examined activated Rac and Rho in dynamically blebbing and attached cells. Rac activity decreased in dynamic blebbing cells. Over-expressing activated Rac in hESC reduced blebbing and promoted cell attachment. Results were validated with a Rac inhibitor which also prolonged dynamic blebbing and reduced cell attachment. These data identified a pathway involving P2X7 that initiates and prolongs dynamic blebbing during hESC passaging. This pathway provides new insight into factors that increase dynamic blebbing, such as release of ATP from cell that die during passaging and identities new targets, such as P2X7, that could be used to decrease dynamic blebbing and improve cell attachment and survival. These results may lead to better ways to

control dynamic blebbing in cultured hESC and further show that hESC are an excellent model for studying blebbing and its role in early embryonic development.

Key words: Stem cells, P2X7 receptor, Blebbing, Cell culture, ATP signaling, Rac/Rho

Introduction

In many cells, the plasma membrane and underlying actin filaments interact dynamically with each other to produce cell surface blebs, which may be either dynamic (non-apoptotic) or apoptotic (Chapter 3) [1,2,3,4,5,6]. Dynamic blebbing occurs in three phases: nucleation, expansion, and retraction [1]. When the actin cortex separates from the overlying plasma membrane, pressure within the cell pushes a bleb through the ruptured actin. The bleb expands to full size until actin reassembles beneath the bleb membrane and with myosin eventually retracts the bleb into the cell.

Dynamic blebbing occurs in a variety of cell types including fibroblasts, endothelial and mesenchymal cells, cancer cells, immune cells, germ cells, amoeba, parasites, bacteria [7], and human embryonic stem cells (Chapter 3) [8,9]. Dynamic blebbing has become a topic of recent interest because of its wide spread distribution in cells and its role in physiological and disease-related processes. Dynamic blebbing occurs as a normal process during cytokinesis [1,10,11,12,13], and in some cells, dynamic blebbing is the driving force that enables cell migration [14,15,16]. For example, in amphibian and fish embryos, dynamic blebbing facilitates cell movement during embryonic development [17,18,19,20], and cells dissociated from amphibian embryos can migrate using bleb-like protrusions [21,22,23]. Inverse blebs were recently shown to play a role in lumen formation during angiogenesis [24]. In addition the role of blebbing in normal cells, dynamic blebbing is a factor in some types of disease. For example, *Entamoeba histolytica* cells invade organs, such as the liver, using bleb-driven motility [25] and blebbing has been reported to enhance the motility, migration, and invasion of breast cancer cells [26].

Human embryonic stem cells (hESC) undergo vigorous dynamic blebbing when they are freshly plated on Matrigel-coated dishes (Chapter 3) [8,9]. hESC bleb longer and produce more blebs that other cell types during passaging. Dynamic blebbing slows cell attachment, and cells that fail to attach eventually undergo apoptotic blebbing and die. We have previously shown that in freshly passaged hESC, dynamic and apoptotic blebbing are separated temporally and are mechanistically distinct (Chapter 3). Because dynamic blebbing interferes with cell attachment, Rock inhibitors (such as Y27632) or blebbistatin, a myosin II inhibitor, are often added to culture media to block activation of myosin II, which in turn stops dynamic blebbing and facilitates cell attachment and survival [27,28,29,30]. However, these inhibitors are not entirely specific and seem to cause excess spreading and stressing of cells during treatment [31]. For therapeutic application of pluripotent stem cells, potent inhibitors of the ROCK pathway may not be suitable for use in expanding and culturing hESC and iPSC. Ideally, dynamic blebbing could be controlled by alternate methods that are not stressful to cells and which do not have off-target effects.

While the downstream effectors of dynamic blebbing have been characterized [27,28,29,30,32,33], little is known about what initiates dynamic blebbing in hESC upstream of Rho. P2X7 receptors are ATP-gated ion channels that upon activation lead to an influx of extracellular calcium. Binding of ATP to P2X7 induces opening of a channel selective for small cations, and with time the pore becomes larger allowing molecules up to 900 kD to enter [34]. P2X7 activity can be found in a number of cell types where it mediates the influx of Ca^{2+} and Na^{+}. In 2007, dynamic blebbing was observed in calvarial cells from wild type, but not P2X7 knock-out mice, suggesting the P2X7 receptor might regulate dynamic blebbing in these cells [35]. P2X7 receptors were

coupled to activation of phospholipase D and A_2, and inhibition of these phospholipases suppressed ATP induced dynamic blebbing in osteoblasts [35]. ATP induced dynamic blebbing in several other cell types, including hepatocytes [36], thymocytes [37], and macrophage cell lines [38]. These data prompted us to look for P2X7 receptors in undifferentiated hESC and to examine their role in dynamic blebbing.

The specific purpose of this study was to test the hypothesis that dynamic blebbing is induced during passaging of hESC by activation of P2X7 receptors that respond to increased extracellular ATP released during cell passaging. Activation of P2X7 enables calcium influx which in turn initiates dynamic blebbing. By characterizing the initiation phase of dynamic blebbing in hESC, we expect to identify new targets and strategies to facilitate cell attachment during passaging, to improve plating efficiency and methods of hESC culture, reduce stress during culture, and to better understand the behavior and motility of cells representative of the epiblast in early post-implantation embryos.

Materials and Methods

Antibodies and chemicals

Mouse anti-P2X7 antibody was purchased from Proteintech Group (Chicago, IL). Rabbit Oct4 antibody was purchased from Abcam (Cambridge, MA). Goat anti-mouse antibody IgG secondary antibody conjugated to Alexa Fluor 594 was purchased from Sigma-Aldrich (St Louis, MO) and goat anti-rabbit IgG secondary antibody conjugated to Alexa Fluor 488 were purchased from Invitrogen (Carlsbad, CA). Apyrase, 1,2-Bis(2-aminophenoxy)ethane-N,N,N′,N′-tetraacetic acid tetrakis(acetoxymethyl ester) (BAPTA), and ethylene glycol tetraacetic acid (EGTA) were purchased from Sigma-Aldrich (St. Louis, MO). The P2X7 inhibitors, AZ11645373 and KN-62, were purchased from Tocris

Bioscience (Minneapolis, MN). Vectashield antifade mounting medium with 4' 6-diamidino-2-phenylindole (DAPI) was purchased from Vector Laboratories (Burlingame, CA).

Cell Culture

Experiments were done using H9 hESC purchased from WiCell (Madison, WI) as frozen vials then expanded and frozen down in our lab as described in detail previously [39,40]. Before setting up experiments, hESC were expanded by plating on Matrigel-coated 6-well plates (Thermo Fisher Scientific, Waltham, MA). Cultures were maintained in mTeSR medium (Stem Cell Technologies, Inc Vancouver, Canada.) in 5% CO_2 at 37°C. When colonies reached 70%-80% confluency (equal to about 1 - 1.5 million cells), hESC were used in experiments. For single cell experiments, hESC were detached by treatment with Accutase (Affymetrix eBioscience, San Diego, CA) for 3 minutes. A 1 ml pipette was used to rinse cells off the plate by pipetting the Accutase solution repeatedly inside the well. Once the cells detached from the plate, Accutase was neutralized using mTeSR medium. To ensure that cells were single, they were passed through an 18-gauge syringe needle (0.33X12.7mm) (BD, Franklin Lakes, NJ) before plating on a new culture dish. Dynamically blebbing cells were studied immediately after plating on Matrigel-coated dishes, while apoptotically blebbing cells were studied after 1.5 hours of incubation on non-coated 35 mm high dishes, (Ibidi, Madison, WI), which do not enable attachment.

RT-PCR

Total RNA was extracted from cultured hESC using an RNeasy Mini Kit (Qiagen, Valenica, Ca) and RNA was checked for purity and degradation using the Agilent 2100

Bioanalyzer as described previously [41]. Only samples with a RIN (RNA integrity number) of 7 were used for experiments. cDNA was prepared using a Qiagen RT2 First Strand Kit (Qiagen, Valencia, CA) from 400 ng RNA. cDNA was amplified with PCR using GAPDH and actin primers to verify that the cDNA synthesis reaction worked. Qiagen HotStarTaq Master Mix (Qiagen, Valencia, CA) and the BioRad Thermal Cycler (BioRad, Hercules, CA) were used for the PCR reaction. Primers used in this paper as follows: P2X7: 5'-TAT CCC TGG TGC AAG TGC TGT- (forward), 5'-AGC TGT GAG GTG GTG ATG CAG- (reverse), Actin: 5'-ATC TGG CAC CAC ACC TTC TAC-(forward), 5'CGT CAT ACT CCT GCT TGC TGA-(reverse). GAPDH: 5'-GGA GCC AAA AGG GTC ATC ATC-(forward). 5'-AGT GAT GGC ATG GAC TGT GGT-(reverse). Lonza DNA FlashGels were used to run the PCR products which were imaged using a Lonza FlashGel imaging system (Lonza, Walkersville, MD)

Immunostaining

hESCs were plated in 6-well plates at 20% confluency. When cells reached 70% confluency, they were washed with PBS and fixed in 4% paraformaldehyde/PBS at room temperature for 15 minutes using procedures described in detail previously (Chpater 3). After washing with PBS, cells were incubated with blocking solution (10% normal serum from the same species as the secondary antibody in PBS and 0.1% Triton X-100) for 30 minutes at room temperature. Cells were then washed with PBS and incubated with 1%BSA/PBS for 20 minutes at room temperature. Cells were incubated with mouse anti-P2X7 antibodies and rabbit anti-OCT4 antibodies at 4°C overnight, then washed with PBS two times the next day, and incubated at room temperature for 1 hour with goat anti-mouse secondary antibodies conjugated to Alexa 594 and goat anti-rabbit

secondary antibodies conjugated to Alexa 488. Cells were washed with PBS and mounted with Vectashield containing 4' 6-diamidino-2-phenylindole (DAPI) for nuclear staining, and examined with a Nikon Eclipse T1 inverted microscope equipped with Elements deconvolution software.

In some experiments, embryoid bodies that had begun to differentiate were labelled with the P2X7 antibody. Embryoid bodies were prepared by incubating small clumps of hESCs in hESC medium (400 ml Knockout DMEM, 100 ml fetal bovine serum, 5 ml 10 mM non-essential amino acid, 5 ml 200 mM L-glutamine, and 5 ml 100X Beta-mercaptoethanol) without bFGF on bacterial-grade Petri dishes. Embryoid bodies were formed in suspension and fed every 2-3 days depending upon density and size. After 5 days, embryoid bodies were plated on Matrigel-coated dishes for another 3-4 days and then labeled with the antibody to P2X7 and OCT4 as described above.

Extracellular ATP concentration

The concentration of ATP in the culture medium was compared at 0, 1, and 24 hours after incubation began. The 24 hour sample was collected 24 hours after cells were plated on 6-well plates For other times points, cells were treated with Accutase for 3 minutes, neutralized with a 2X volume of mTeSR, then centrifuged at 800 rpm for 3 minutes. After pellets were broken with fresh mTeSR, cells were re-plated in 6-well plates. Medium was collected from the plates either immediately (0 hours) or 1 hour after plating. Fresh mTeSR was used for the control. ATP concentrations in these samples were determined using the ViaLight Plus Sample Kit (Lonza, Allendale, NJ.) according to the manufacturer's instructions.

Effect of Extracellular ATP on dynamic blebbing and attachment of hESC

The effect of extracellular ATP on dynamic blebbing and attachment was examined using time-lapse images collected in a Nikon BioStation IM (Nikon, Tokyo, Japan), which combines an incubator, microscope, and cooled CCD camera [31,42]. Single hESCs were prepared following the protocol described above (cell culture). Single hESCs were incubated in mTeSR containing 3 mM ATP in the BioStation IM, and time-lapse data were collected every 1.5 minutes for 4 hours. Videos were examined and manually counted every 20 minutes for 160 minutes to quantify the percentage of blebbing and attached cells [31]. To determine if removing extracellular ATP affected dynamic blebbing and attachment, ATP was hydrolyzed with 1 mM apyrase prior to and during plating. Time-lapse data were collected and analyzed for blebbing and attaching cells every 12 minutes for 60 minutes.

Effect of P2X7 antagonists on dynamic blebbing and attachment

To determine if antagonists to P2X7 blocked dynamic blebbing and accelerated attachment, single hESCs were incubated with 100 nM AZ11645373 or 5 μM KN-62 and imaged every 4 minutes in a BioStation IM for 4 hours. Untreated single cells were used as the negative control group in all experiments. Data were examined and analyzed for both dynamic blebbing and attached cells. Videos were counted manually every 4 (AZ11645373) or 12 (KN-62) minutes for 40 (AZ11645373) or 60 (KN-62) minutes.

P2X7 knockdown by siRNA Nucleofection

H9 hESC OCT4-GFP, which constitutively express GFP, were cultured using the same protocol as described for H9 hESC. Delivering GFP siRNA into hESC OCT4-GFP cells

served as a positive control for determining the efficiency of nucleofection and RNA interference. Prior to nucleofection, hESC OCT4-GFP were treated with 10μM Rho-associated protein kinase (ROCK) inhibitor for 1 hour. Cells were then dislodged from plates into small clumps consisting of triplets of cells using 0.25% trypsin. Nucleofection (Lonza, Allendale, NJ) was used to deliver siRNA by mixing plasmid DNA with nucleofection stem cell solution containing supplement. GFP siRNA and P2X7 siRNA were nucleofected into separate batches of single hESC OCT4-GFP to knockdown GFP or P2X7 mRNA. Nucleofection was done using the B-16 program on the Amaxa Nucleofector 2b device (Lonza, Allendale, NJ), which gives high efficiency and low cell death when used with H9 hESC. Additional controls included cells that did not undergo nucleofection and cells that underwent nucleofection without siRNA.

Both GFP siRNA and P2X7 siRNA nucleofected cells were plated on mouse embryonic fibroblasts (mEFs) with 10 μM ROCK inhibitor for 3 days and without ROCK inhibitor for another 2 days in 5% CO_2 at 37°C. After 5 days of incubation, one batch of cells was used to determine if dynamic blebbing was inhibited by knockdown. Nucleofected cells were evaluated in time-lapse videos collected in the BioStation IM. The percentage of blebbing and non-blebbing cells were analyzed in at least 3 videos in both control and P2X7 siRNA treatment groups. A second batch of hESCs was taken off the mEFs and followed to determine the efficiency of GFP and P2X7 mRNA knockdown and to determine if dynamic blebbing was inhibited by P2X7 knock-down. Efficiency of knock-down was determined by qPCR.

Calcium and Blebbing

To determine if extracellular or intracellular calcium plays a role in dynamic blebbing, single hESCs were incubated with 10 mM EGTA or 10 mM BAPTA, and time-lapse images were collected every 3 minutes in the BioStation IM for 4 hours. Untreated single cells were used as the negative control group in all experiments. Cells treated with BAPTA were pre-incubated with BAPTA for 4 hour prior to passaging. Blebbing and non-blebbing cells were examined by following all cells individually.

Calcium influx on Blebbing Cell

Cells were removed from incubator and washed with PBS. Cells were then incubated with 5 μM Fluo4 (Invitrogen, Carlsbad, CA) for 45 minutes at room temperature. After 45 minutes of incubation, cells were washed with PBS and incubated with mTeSR for 30 minutes at 37°C. Cells, which were pre-loaded with Fluo4, were then incubated with Accutase, Accutase+ 3mM ATP, or Accutase+ 5 μM KN62. Images were taken with a Nikon Eclipse T1 inverted microscope equipped with 480nm excitation wavelength. Images were analyzed with Image J to determine the fluorescence intensity.

Effect of Rac and ROCK inhibitors on Blebbing

To determine if Rac and ROCK were involved in dynamic blebbing in hESC, cells were treated with 50 μM Rac inhibitor (NSC23766) (R&D Systems, Minneapolis, MN) or ROCK inhibitor (Y27632) (Tocris Bioscience, MN), and time-lapse images were collected every 3 minutes in the BioStation IM for 4 hours. Untreated single cells were used as the negative control in all experiments. Cells treated with NSC23766 were pre-incubated

with NSC23766 for 4 hour prior to passaging. Blebbing and non-blebbing cells were examined by following all cells individually.

Rac1 and Rho Pull-Down and Detection

To quantify the expression of Rac-GTP and Rho-GTP in attached and blebbing cells, the active Rac1 and Rho Pull-Down and Detection Kits (Thermo Scientific, Carlsbad, CA) were used. Blebbing cells were removed from plates with Accutase (3 minutes), which was neutralized using mTeSR medium. Cells were centrifuged at 1,200 rpm for 3 minutes, then plated on non-coated dishes for 1 hour at 37°C. Lysates of attached and blebbing cells were collected and went through the pull-down assay to monitor Rac1 and Rho activation using the protocol in the manufacturer's instructions.

Results

Dynamic blebbing and attachment of hESC during plating

hESC undergo dynamic blebbing, which is distinct from apoptotic blebbing, when passaged and plated *in vitro* (Chapter 3)[8,9]. Dynamic blebbing interferes with cell attachment, and hESC that fail to attach eventually undergo apoptosis. Blebs in various states of initiation, expansion, and retraction appear on the cell surface.Figure 4.1a shows a film strip of a dynamically blebbing hESC, and the expansion of a single segmented bleb is shown in Figure 4.1b. Blebbing likely stresses cells and occasionally blebs are shed from the cell surface. Formation of dynamic blebs takes an average of 8 seconds, while retraction requires 22 seconds. When cultured with our standard protocol, freshly plated cells normally undergo dynamic blebbing for 60 to 90 minutes, after which time they attach and spread on the substrate (Fig. 4.1c). Dynamic blebbing is controlled by actin and myosin II and is also affected by the polymerization state of tubulin (Chapter 3).

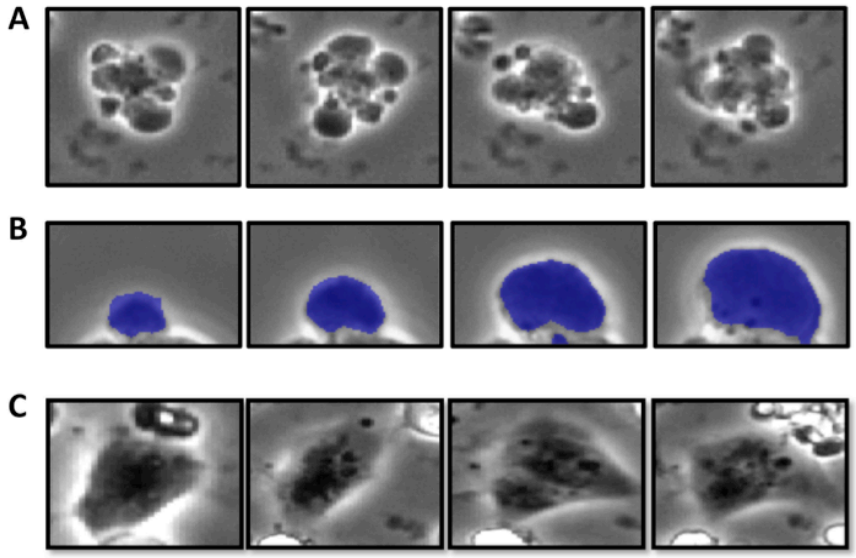

Figure 4.1: Time lapse images of dynamically blebbing and attached hESC in culture. (A) Phase images of a single hESC undergoing dynamic blebbing. (B) A single bleb, masked with blue, expanding from the cell surface. (C) A cell that has stopped blebbing and attached and spread on Matrigel.

P2X7, an ATP-gated ion channel, is present in pluripotent hESCs but not in differentiating hESCs

We hypothesized that dynamic blebbing is activated through P2X7 channels present on pluripotent hESC. PCR was used to show that H9 hESC express *P2X7* (Fig. 4.2 a). Translation of the *P2X7* mRNA in pluripotent hESC was demonstrated using an anti-P2X7 antibody (Figs. 4.2 b-e). hESC showed strong immunofluorescent labeling with antibodies to both OCT4, indicating pluripotency, and P2X7. The P2X7 labeling was concentrated at the cell periphery consistent with localization in the plasma membrane (Fig. 4.2 e). The center of embryoid bodies had strong OCT4 and P2X7 labeling; however, differentiating cells that had begun migrating away from the body did not label for either OCT4 or P2X7 (Figs. 4.2 f-i).

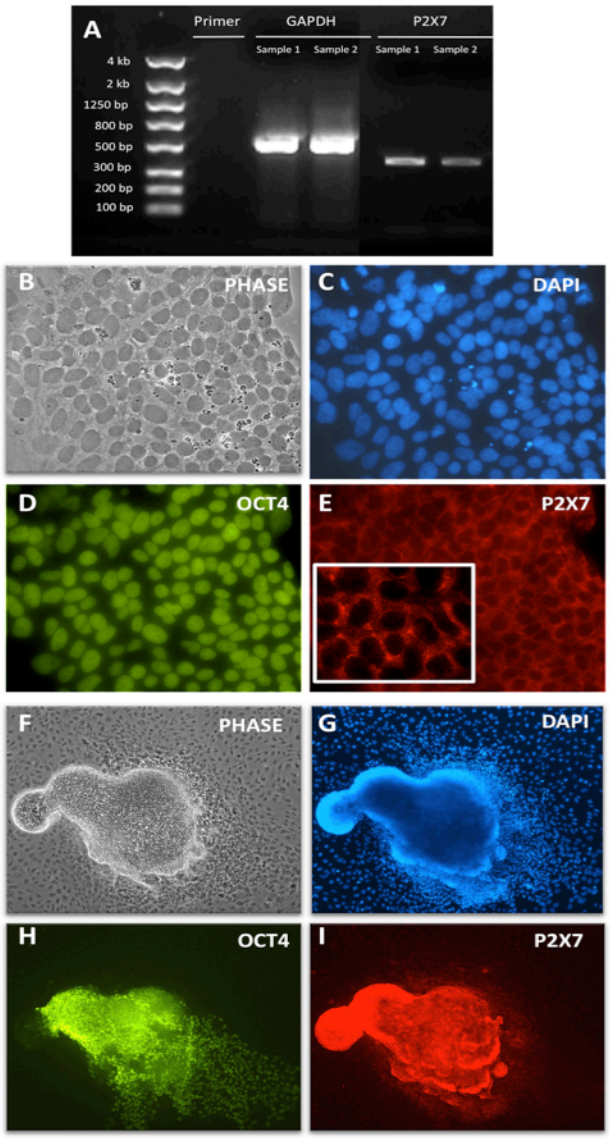

Figure 4.2: Pluripotent hESC express P2X7. (A) RT-PCR gel of hESC showing P2X7 was expressed in pluripotent cells. (B-E) Phase contrast image and immunofluorescent labeling of hESC with antibodies to OCT4 (green) and P2X7 (red). The nucleus was localized using DAPI (blue). P2X7 labeling is shown at higher magnification in the insert in E. (F-I) Phase contrast image of EBs that were labeled with antibodies to OCT4 (green) and P2X7 (red). The nucleus was localized using DAPI (blue). Differentiating cells that had moved away from the center of the EB did not label with OCT4 or P2X7.

Extracellular ATP increased during passaging

Since P2X7 receptors are activated by extracellular ATP, we hypothesized that ATP was released from cells during passaging, when some cell damage and death occurs. To determine if extracellular ATP plays a role in dynamic blebbing, we first measured ATP

concentrations in the culture medium at different times before and after plating hESC (Fig. 4.3 a). ATP concentrations were low in the mTeSR control (medium only). Before removing cells that had been growing 24 hours for passaging, ATP concentrations were also low in the extracellular medium (Fig. 4.3a 24 hour sample). However, ATP concentration in the 0-hour medium sample taken immediately after removing cells from the plate was about 14-fold higher than in the 24-hour sample taken before passaging. This indicated that significant amounts of ATP were released from cells during passaging, probably due to damage and lysis of cells. By 1-hour after plating, the levels of extracellular ATP in the culture medium decreased significantly compared to the 0 hour sample. These results show that ATP levels are very high during passaging but return to near control levels by about 1 hour after plating, which coincides with the approximate time that blebbing ceases and cells attach to the substrate [31]. These observations support our hypothesis that extracellular ATP is released during passaging of hESC.

Extracellular ATP plays a role in dynamic blebbing

We next determined if extracellular ATP plays a role in dynamic blebbing of hESC by adding ATP to culture medium during plating (Fig. 4.3 b-c). Cells were plated in control medium or in medium containing 3 μM ATP, time-lapse live cell images were collected, and blebbing and cell attachment were quantified at various times during incubation. As shown in Figures 3 b and c, the presence of 3 μM ATP caused a significant increase in the percentage of the cells undergoing dynamic blebbing over a 140 minute interval and at the same time inhibited efficient attachment of cells to their substrate.

When apyrase, which degrades ATP, was added to control culture medium before and during passaging, the percentage of cells undergoing dynamic blebbing was significantly

reduced at the early time points after plating, and this was accompanied by an increase in the number of attached cells (Figs. 4.3 d and e). These data support the idea that extracellular ATP, released during passaging, increases and extends dynamic blebbing and inhibits attachment of hESC.

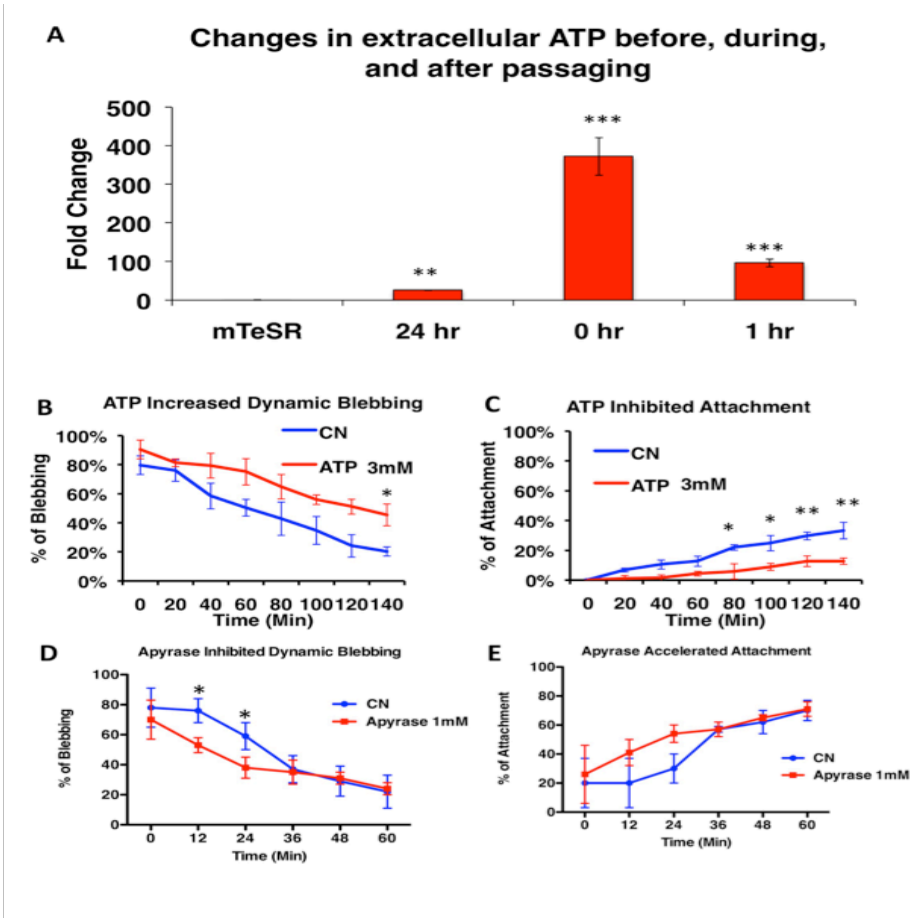

Figure 4.3: Extracellular ATP plays a role in dynamic blebbing. (A) The viaLight Plus Sample Kit was used to quantify extracellular ATP in media collected before, during and after passaging. Extracellular ATP increased during passaging (0 hour) when blebbing occurred. ATP decreased by 1 hour after plating, when blebbing subsided and attachment occurred. (B, C) ATP added to the culture medium increased dynamic blebbing and inhibited attachment. (D, E) Apyrase, which degrades ATP, inhibited dynamic blebbing and accelerated attachment. Analyses were done by counting the percentage of blebbing and attached cells in three different BioStation videos at 20 minute intervals (ATP) or 12 minute intervals (apyrase) in three independent experiments. Data are plotted as the means ± the standard deviations of three experiments. * = $p < 0.05$, ** = $p < 0.01$

Dynamic blebbing was decreased by P2X7 inhibitors and by knocking down P2X7 expression.

To test the hypothesis that the ATP receptor P2X7 is involved in dynamic blebbing of hESC, the effects of two P2X7 inhibitors, AZ11645373 and KN-62, on blebbing and attachment were tested during passaging of single cells. hESC were plated with either mTeSR alone (control) or mTeSR containing 100 nM of AZ11645373 or 5 uM of KN-62 (Figs. 4.4 a-d). Video data were collected in a BioStation IM and analyzed to determine the effect of the inhibitors on dynamic blebbing and cell attachment. Both AZ11645373 and KN-64 significantly inhibited dynamic blebbing and accelerated hESC attachment (Figs. 4.4 a-d).

We further tested the role of P2X7 in blebbing and attachment of hESC by knocking down the expression of P2X7 using siRNA. OCT4-GFP hESC were used to determine the nucleofection efficiency for this experiment. OCT4-GFP hESC were nucleofected with either GFP siRNA or P2X7 siRNA. The cells, which were nucleofected with GFP siRNA, were used as a control. siRNA successfully decreased expression of P2X7 in OCT4-GFP hESC (Fig. 4.4 e). We also incubated the OCT4-GFP hESC, which were nucleofected with P2X7 inhibitor, in a BioStation IM to determine if dynamic blebbing was affected. We followed individual cells and determined if the cells blebbed or not. As we found in the P2X7 inhibitor experiments, P2X7 siRNA successfully decreased dynamic blebbing during passaging (Fig. 4.4 f). The inhibitor and siRNA knockdowns support the idea that the ATP receptor, P2X7, plays a role in dynamic blebbing of hESC.

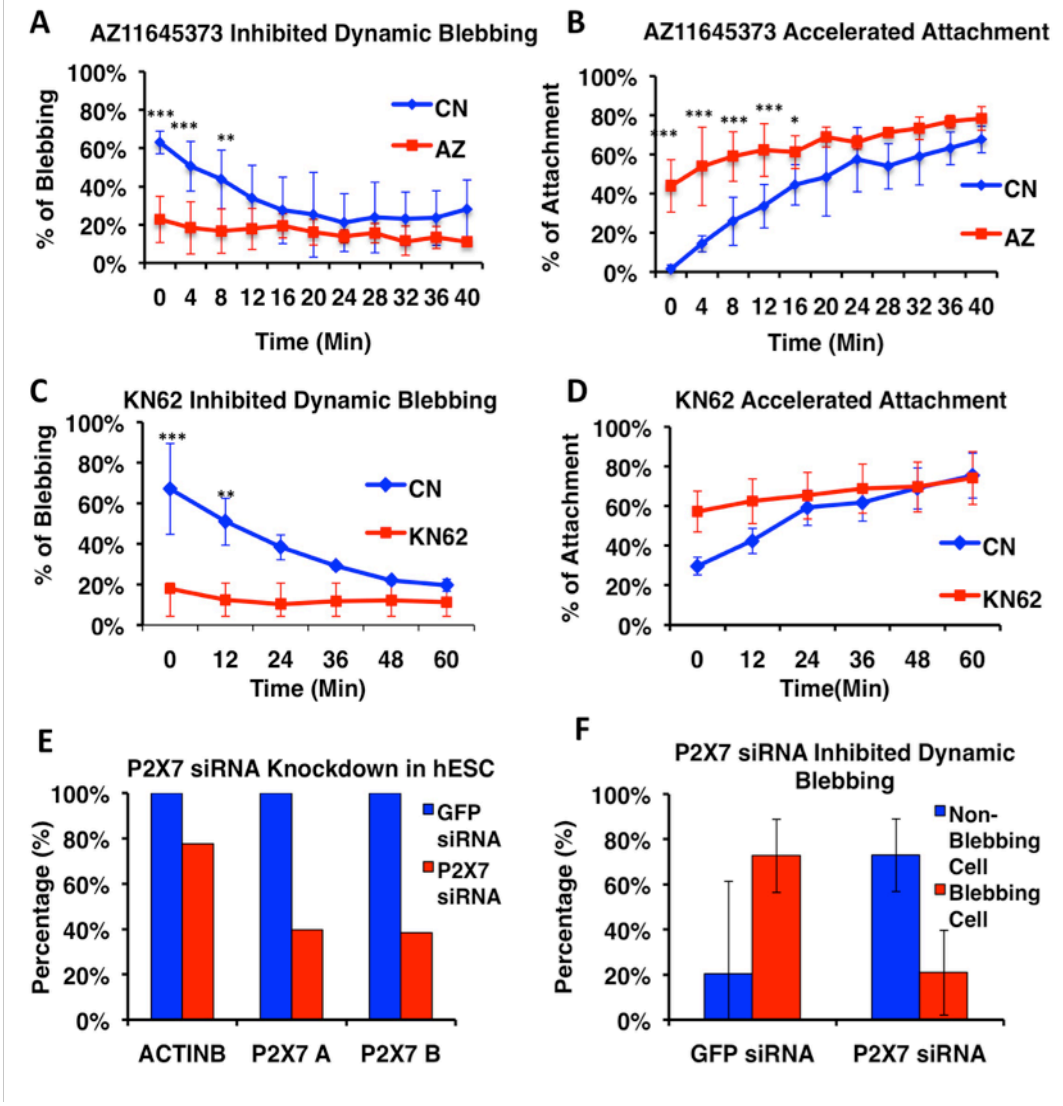

Figure 4.4: P2X7 inhibitors (AZ11645373 and KN62) and P2X7 siRNA knock-down inhibited dynamic blebbing in hESC. (A-D) Cells treated with 100 nM AZ11645373 or 5 uM KN62 underwent less dynamic blebbing than the control groups (CN). Analyses were done by counting the percentage of blebbing and attached cells in three different BioStation videos at 4 minute intervals. Data are plotted as the means ± standard deviations of independent three experiments. (E-F) Cells transfected with GFP siRNA and P2X7 siRNA using nucleofection. After 4 days, cells were collected for qPCR and time-lapse videos. (E) Actin and P2X7 gene expression was examined by qPCR. P2X7 siRNA successfully knocked down expression of P2X7 without affecting expression of actin. (F) Non-blebbing and blebbing cells were analyzed by counting the percentage of cells in each group in BioStation videos at 1.5 minute intervals. 25 cells were analyzed in the GFP siRNA group and 10 cells were analyzed in P2X7 siRNA group. * = $p < 0.05$, ** = $p < 0.01$, *** = $p < 0.001$.

Calcium influx plays a role in dynamic blebbing in hESC

Because activation of the P2X7 receptor by ATP permits Ca^{2+} influx, we hypothesized that influx of extracellular Ca^{2+} initiates dynamic blebbing of hESC. During passaging, cells were incubated with 10 mM EGTA, a chelating agent with a high affinity for extracellular calcium, and imaged in a BioStation IM. Individual cells were followed for 4 hours and classified as either blebbing or non-blebbing (Fig. 4.5 a). The 10 mM EGTA treated group had a significantly higher percentage of non-blebbing cells than the control group (Fig. 4.5 a), indicating that chelation of extracellular calcium inhibited the occurrence of dynamic blebbing.

To determine if calcium passing through the P2X7 receptor affected blebbing, hESC were pre-loaded with 10 mM BAPTA for 1 hour to chelate calcium that entered during passaging (Fig. 4.5 b). hESC were then removed from their plate and passaged onto a fresh plate in medium containing BAPTA. Individual cells were monitored in time-lapse videos collected with a BioStation IM. Approximately 70-80% of the cells in the control group underwent dynamic blebbing. This percentage was significantly reduced in the BAPTA loaded group (Fig. 4.5 b). These data support idea that BAPTA chelated calcium that entered cells through the P2X7 receptors during passaging.

Calcium influx occurred through P2X7 receptors activated by ATP.

To monitor calcium influx, cells were pre-incubated with Fluo-4 for 45 minutes then were removed from the plates with Accutase, Accutase with 3mM ATP or, Accutase with 5 μM KN62. Cells were then imaged with Nikon Eclipse Ti inverted microscope. Images were taken immediately after Accutase, Accutase with ATP, or Accutase with KN62 were added in each group. The fluorescent intensity ratio (cell/ background) was measured using Image J. Cells that were removed from the plate with Accutase or

Accutase with 3mM ATP had high calcium influx; however, calcium influx was significantly blocked by 5 μM KN-62 (Fig. 4.5 c). To confirm that calcium influx was blocked by KN-62, we also measured the ATP concentration in these three groups. ATP concentration was significantly higher in Accutase, Accutase with ATP, and Accuatse+KN62 than the control (Fig. 4.5 d). These results showed that calcium influx occurred when the P2X7 receptor was activated by extracellular ATP.

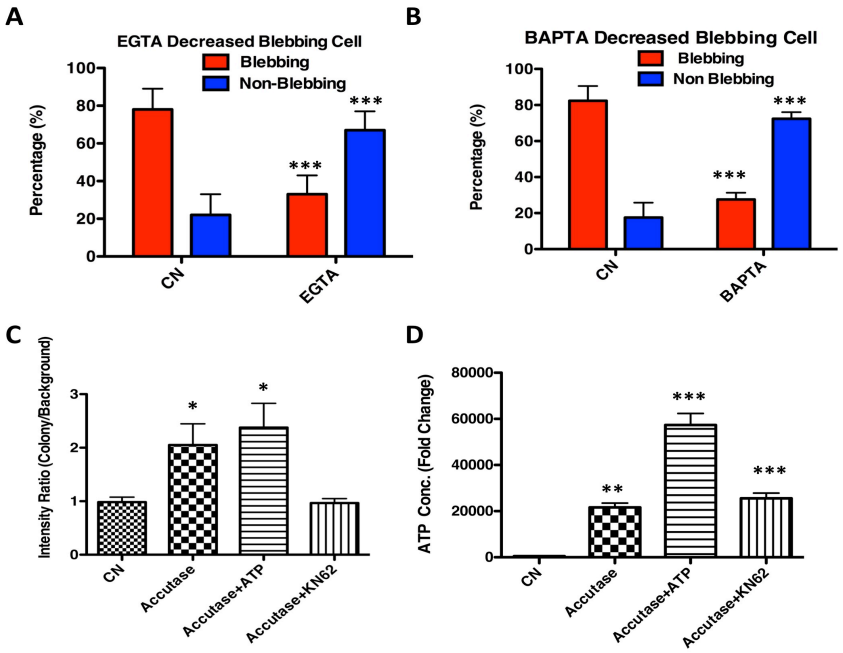

Figure 4.5: Extracellular calcium is required for dynamic blebbing. (A) EGTA inhibited dynamic blebbing in hESCs. Cells were treated with 10 mM EGTA before and during passaging. Analyses were done by counting the percentage of blebbing and non-blebbing cells in nine different BioStation videos in three independent experiments. (CN: 571 cells and EGTA: 441 cells). (B) BAPTA, a chelator of intracellular calcium, inhibited dynamic blebbing. Cells were treated with 10 mM BAPTA before and during passaging. Analyses were done by counting the percentage of blebbing and non-blebbing cells in nine different BioStation videos in three independent biological samples. (CN: 95 cells, BAPTA: 134 cells) (C) Accutase and Accutase with ATP increased calcium influx in hESC but the effect was inhibited by KN62. Cells were pre-incubated with Fluo4 and then treated with Accutase, Accutase with ATP, or Accutase with KN62. Analyses were done with Image J. (D) ATP concentrations were significantly higher in Accutase, Accutase with ATP, and Accutase with KN62. * = $p < 0.05$, ** = $p < 0.01$, *** = $p < 0.001$.

Rho and Rac Regulate Dynamic Blebbing and Cell Attachment in hESC

We next determined if Rac and Rho were involved in dynamic blebbing in hESC. Cells were treated with ROCK inhibitor (Y27632) or Rac inhibitor (NSC23766) and imaged in a BioStation IM. ROCK inhibitor blocked dynamic blebbing and accelerated cell attachment in hESC (Fig. 4.6 A, B). In contrast, cell blebbing was prolonged and attachment was delayed when Rac inhibitor was present (Fig. 4.6 C, D). To confirm that Rac stops dynamic blebbing, cells were nucleofected with a GFP-Rac-activated plasmid and imaged in BioStation IM for 6 hours. Cells which showed GFP expression were followed to determine if they undergo blebbing (Fig. 4.6 E). The percentage of blebbing cells in the population that underwent nucleofection with the Rac-activated plasmid was lower than in the control on day 0. After 5 days of culture, cells were removed from the plate with Accutase and replated. GFP positive cells with Rac-activation had significantly less blebbing than control cells (Fig. 4.6 F). We further tested the expression of active-Rac (Rac-GTP) and active-Rho (Rho-GTP) in attached cells and blebbing cells using western blotting. Blebbing cells had significantly less Rac-GTP expression than attached cells (Fig. 4.6 G). In contrast, blebbing cells had more Rho-GTP expression than attached cells (Fig. 4.6 H). These results show that Rho was activated in dynamic blebbing cells and Rac was activated in attached cells.

Figure 4.6: Rho and Rac Regulate Dynamic Blebbing and Cell Attachment hESC. (A, B) Dynamic blebbing was fully inhibited and attachment was accelerated in hESC treated with Y27632. Analyses were done by counting the percentage of blebbing and attached cells in three different BioStation videos at 20 minute intervals. Data are plotted as the means ± standard deviations of three independent experiments. (C, D) Cells treated with NSC23766, a Rac inhibitor, underwent more blebbing and less attachment than the control groups. Analyses were done by counting the percentage of blebbing and attached cells in three different BioStation videos at 12 minute intervals. Data in C and D are plotted as the means ± standard deviations of three experiments. (E, F) hESC were nucleofected with GFP-RAC activated plasmid and incubated in a BioStation IM. Phase contrast and fluorescence images of single cells are shown in at 3 and 6 hours of incubation. (F) Dynamic blebbing was inhibited in hESC after nucleofection. The D0 cells were plated and imaged in the BioStation right after nucleofection, while in the D5 cells were grown for 5 days before replating and imaging with the BioStation. Analyses were done by counting the percentage of blebbing and non-blebbing cells in nine different BioStation videos in three independent biological samples. (G, H) Blebbing cells were removed from the plates, then plated on non-coating dishes for 1 hour at 37°C. Lysates of attached and blebbing cells were collected and went through the pull-down assay to monitor Rac1 and Rho activation. (G) Western blotting showed the expression of Rac-GTP was higher in attached cells than in dynamic blebbing cells. Quantification of western blot was done by ImageJ with three independent experiments. (H) Western blotting showed the expression of Rho-GTP was higher in dynamically blebbing cells than in attached cells. * = $p < 0.05$, ** = $p < 0.01$, *** = $p < 0.001$.

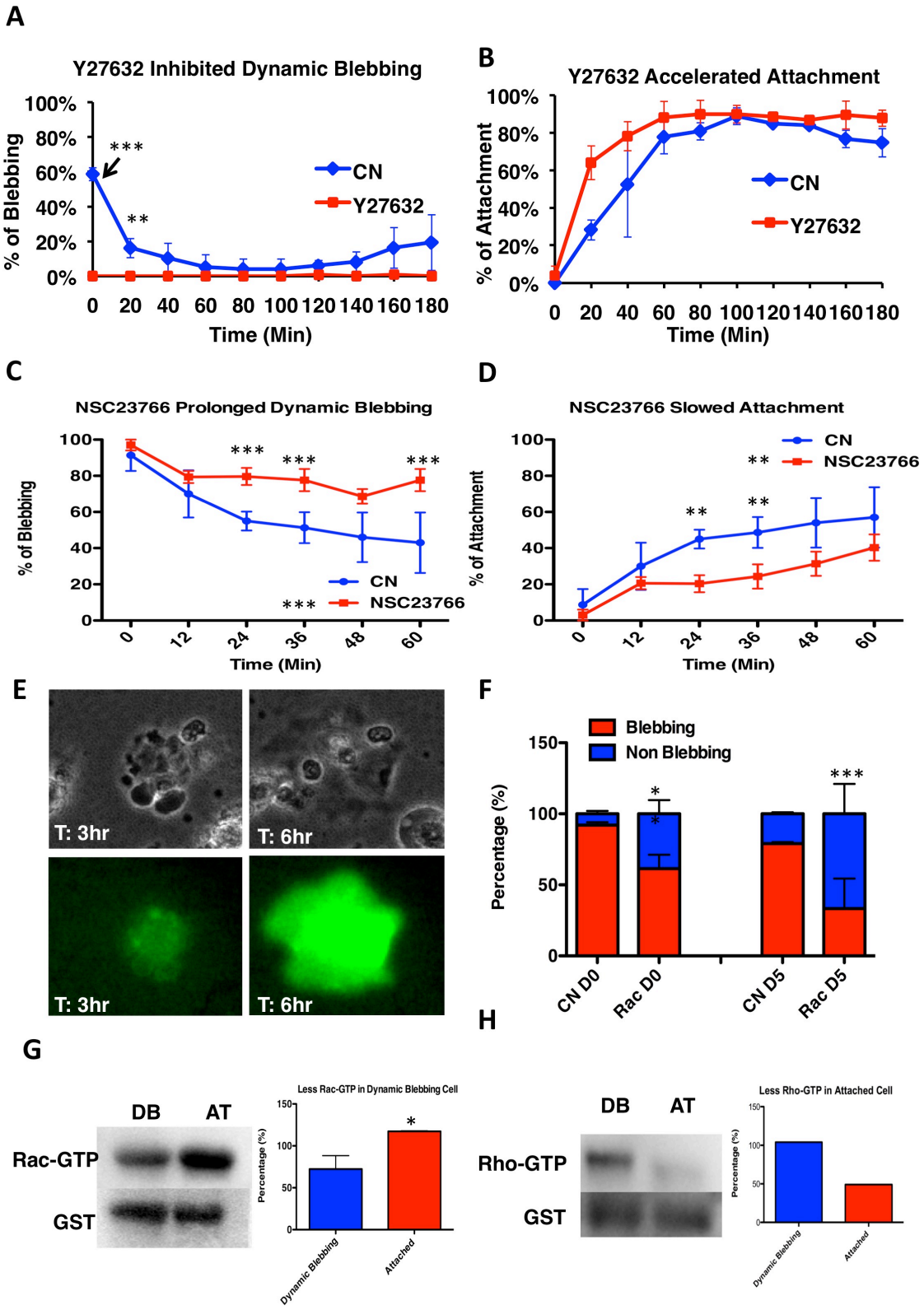
A
Y27632 Inhibited Dynamic Blebbing
% of Blebbing
100%
80%
60%
40%
20%
0%
***
**
CN
Y27632
0 20 40 60 80 100 120 140 160 180
Time (Min)
B
Y27632 Accelerated Attachment
% of Attachment
100%
80%
60%
40%
20%
0%
CN
Y27632
0 20 40 60 80 100 120 140 160 180
Time (Min)
C
NSC23766 Prolonged Dynamic Blebbing
% of Blebbing
100
80
60
40
20
0
***
***
***
***
CN
NSC23766
0 12 24 36 48 60
Time (Min)
D
NSC23766 Slowed Attachment
% of Attachment
100
80
60
40
20
0
**
**
**
CN
NSC23766
0 12 24 36 48 60
Time (Min)
E
T: 3hr
T: 6hr
T: 3hr
T: 6hr
F
Blebbing
Non Blebbing
Percentage (%)
150
100
50
0
*
*
***
CN D0
Rac D0
CN D5
Rac D5
G
DB
AT
Rac-GTP
GST
Less Rac-GTP in Dynamic Blebbing Cell
Percentage (%)
150
100
50
0
*
Dynamic Blebbing
Attached
H
DB
AT
Rho-GTP
GST
Less Rho-GTP in Attached Cell
Percentage (%)
150
100
50
0
Dynamic Blebbing
Attached

Discussion

During passaging, hESC undergo vigorous dynamic blebbing that prevents attachment and spreading of cells. If dynamic blebbing does not stop, cells fail to attach, and eventually undergo apoptosis (Chapter 3). Dynamic blebbing, which stresses cells and causes loss of cytoplasm, can be stopped rapidly when laminins are used as the substrate for attachment. Binding of laminin to hESC integrins activates a FAK, and signaling through the FAK leads to cessation of blebbing. In this study, we showed that the key upstream event that initiates dynamic blebbing in hESC is the activation of the P2X7 receptor which responds to extracellular ATP released during cell passaging (Figs. 3 and 4). P2X7 activation enables calcium influx which in turn initiates blebbing, through activation of the Rho pathway.

Because dynamic blebbing stresses cells and decreases cell survival, it is important to identify new ways to prevent or stop dynamic blebbing during passaging of hESC. Reagents that inhibit myosin II, such as ROCK inhibitors and blebbistatin, have been widely used to accelerate attachment of hESC during passaging and for plating single hESC [27,28,29,30]. However, hESC treated with ROCKi appear stressed [31], suggesting ROCKi may have off target effects that would preclude using ROCKi treated pluripotent stem cells in drug/toxicant testing and in clinical applications. Plating hESC on laminin-521 or on Matrigel coated with laminin-111 significantly reduces the time for attachment by stopping dynamic blebbing (Chapter 3) and offers a safer method for passaging hESC.

Little is known about the factors that initiate dynamic blebbing in hESC. In 2011, RNA interference was used to demonstrate that Active BCR-Related protein (Abr), a unique Rho-GEF family factor containing a functional GAP domain for Rho-class

GTPase, is an upstream regulator of ROCK-myosin hyperactivation and apoptosis in hESC [27]. In other cell types, multiple pathways may converge on Rho [35,44], suggesting additional regulators may be involved in initiating dynamic blebbing. For example, lysophosphatidic acid (LPA) is a phospholipid derivative that can act as a signaling molecule to activate the small GTPase Rho, which in turn activates ROCK. This pathway can lead to inhibition of myosin light-chain phosphatase [45]. However, there is currently no evidence that LPA is increased in hESC during culture.

Our study demonstrates that the P2X7 receptor is involved in initiating dynamic blebbing in hESC during passaging. The P2X7 receptor is an ion channel that opens in response to extracellular ATP allowing cations to enter the cell, thereby triggering diverse responses such as secretion, apoptosis, survival, and proliferation [46,47,48]. P2X7 is expressed in a variety of cell types including monocytes/macrophages, dendritic cells, mast cells, mesangial, and microglial cells [49,50,51]. Its widespread expression in immune cells suggests that the P2X7 receptor has multiple proinflammatory actions [52,53]. In addition, P2X7 is found in many non-immune cells such as human cervical epithelium, retinal pigmented epithelium, and corneal epithelium, where it has been proposed to function in apoptosis, lysosomal alkalization, cell migration, cell proliferation and cell death [54]. The normal role of P2X7 in hESC may be to facilitate proliferation, a function attributed to P2X7 in mouse ESC [55]. However, the P2X7 inhibitor did not alter hESC proliferation during 24 hours of incubation. In both human and mouse ESC, P2X7 was not present when cells began differentiating, indicating that it is an excellent surface marker for pluripotent cells.

The current study demonstrates that extracellular ATP, released during passaging, binds to P2X7 allowing calcium influx which in turn initiates dynamic blebbing

through activation of the Rho pathway. The interplay between Rac and Rho determined wheather cells underwent dynamic blebbing or attached. We showed that activation of Rac reduced dynamic blebbing and that activated-Rac was less abundant in dynamically blebbing cells than in attached hESC. Moreover, inhibition of Rac by NSC23766 extended dynamic blebbing. Rac and Rho regulate motility in many cells in which Rac signaling antagonizes Rho directly at the GTPase level [56]. For example, the balance between Rac and Rho activity determines cellular morphology and migratory behavior in NIH 3T3 fibroblasts [57].

The above results identify several targets that could be used to prevent initiation of dynamic blebbing. One strategy would be to decrease the release of ATP during passaging by using gentle methods that minimize cell death or by using reagents, such as apyrase, that hydrolyze extracellular ATP. Another potential target would be calcium which influxes upon activation of the P2X7 receptor. Inclusion of a chelating agent helped reduce dynamic blebbing, but may also interfere with cell attachment. Rac activation could be used to prevent dynamic blebbing and may be a possible target for improving attachment and plating of single hESC in the future (Fig. 4.7). The best method that we found for inhibiting initiation of dynamic blebbing was includsion of the P2X7 inhibitor (KN62) in culture medium during passaging. This inhibitor is more specific than the ROCK inhibitors, is relatively inexpensive, and does not stress or alter cell morphology, as seen with ROCK inhibitors.

In embryos, dynamic blebbing is a driving force that enables cell migration [58,59,60,61]. While a blebbing cell in suspension does not have progressive motility, in a three-dimensional matrix, blebbing cells can gain space and would be able to escape environmental danger or migrate in an embryo [62]. hESC bleb more vigorously than

other cells types (Chapter 3), indicating that hESC have a cytoskeleton that is poised for hyperactivation. Cultured hESC resemble cells of the epiblast [63,64], which undergo massive movements during gastrulation. The dynamic blebbing observed in vitro may occur because hESC (epiblast-like) would normally gastrulate in an embryo and migrate first as sheets of epiblast and then as mesenchymal cells following extrusion from the primitive steak. This point would require future investigation but the data in this study may help understand the massive cell movements characterized of gastrulating embryos.

In contrast to the hESC used in our study, mouse embryonic stem cells (mESC), which resemble the inner cell mass from which they were derived [64], show relatively little dynamic blebbing *in vitro* during passaging and attach rapidly to their substrate (Chapter 3). Recently, new methods for deriving hESC have been successful in obtaining "naïve" states of pluripotent hESC, which like mESC, resemble cells of the inner cell mass, not the epiblast [64]. It is likely that naïve hESC lines would be less prone to dynamic blebbing and may offer an additional alternative to avoid dynamic blebbing during passaging of pluripotent cells.

In summary, while hESC culture has been evolving since 1997, there is still a need for improvement of culture protocols. We have shown that regulation of dynamic blebbing is key to improving hESC culture. Survival of hESC was increased when dynamic blebbing was controlled during passaging. Characterization of the pathways that initiate and stop dynamic blebbing has led to the identification of targets that can be used to control blebbing during cell passaging. By controlling dynamic blebbing, it is possible to minimize stress, improve survival and plating efficiency, and passage single cells. Unlike ROCKi, the P2X7 inhibitor KN62 did not alter hESC morphology or cause

cells to appear stressed (Supplemental Fig. 4.1). Taken together, these data suggest that P2X7 inhibitors are good cost-effective alternatives to ROCKi during passaging of pluripotent cells. These factors will be critical in developing culturing protocols suitable for using human pluripotent stem cells in therapeutic applications. hESC also offer a tractable model for studying the process of dynamic blebbing, which plays important roles in embryonic development and occurs during cell division. Blebbing hESC may also be developed into an interesting model for studies on human gastrulation.

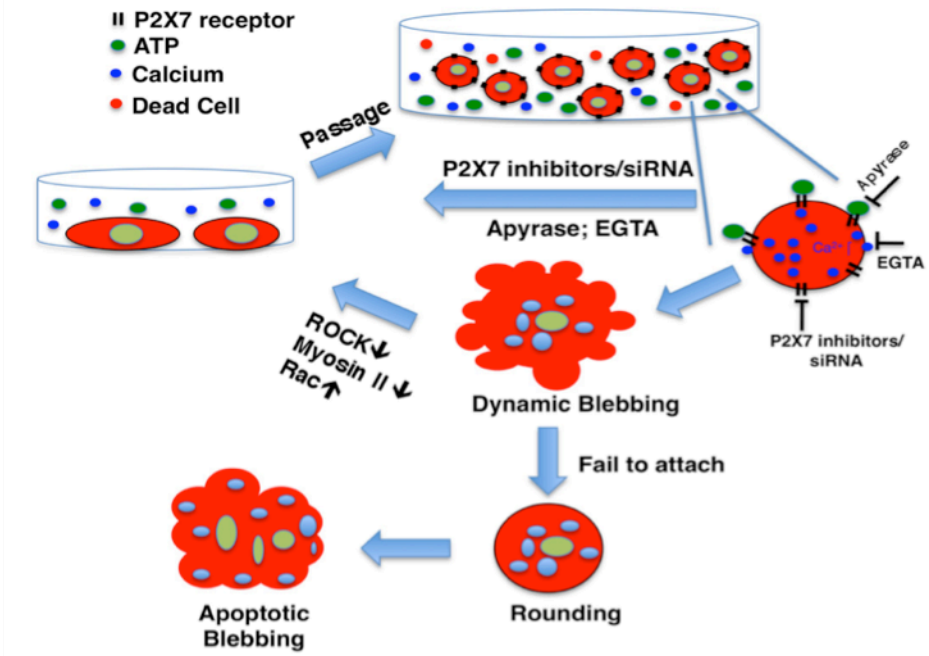

Figure 4.7: Schematic summary of the results of this study. Single hESC culture can be improved by blocking the P2X7 signaling pathway using P2X7 inhibitors/siRNA or by hydrolyzing extracellular ATP or chelating the calcium in the culture medium. Rac activation could be used to prevent dynamic blebbing and may be a possible target for improving attachment and plating of single hESC in the future.

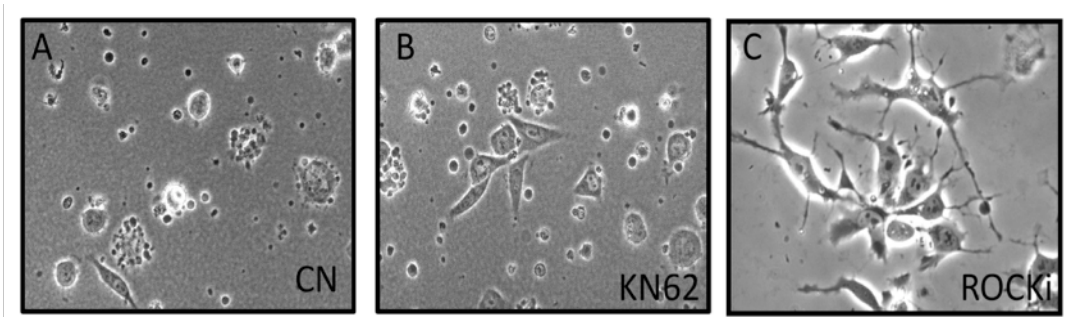

Supplemental Figure 4.1: (A) Single hESC plated on Matrigel. (B) Single hESC plated with P2X7 inhibitor (KN62) on Matrigel. (C) Single hESC plated with ROCK inhibitor (Y27632) on Matrigel. Images were taken about 20 minutes after plating. In the control (CN) and P2X7 inhibitor group (KN62), cells have attached and are beginning to spread normally. In the ROCKi group, cells have spread but have an attenuated stressed morphology.

References

1. Charras GT. A short history of blebbing. Journal of Microscopy, 2008a:231:466-478.

2. Charras GT, Paluch, E. Blebs lead the way: how to migrate without lamellipodia Nat. Rev. Mol. Cell Biol. 2008b:9:730-736.

3. Sahai E, Marshall CJ. Differing modes of tumour cell invasion have distinct requirements for Rho/ROCK signalling and extracellular proteolysis. *Nat Cell Biol*. 2003;5(8):711–719.

4. Hickson GRX, Echard A, O'Farrell PH. RHO kinase controls cell shape changes during cytokinesis. Curr Biol. 2006:16(4): 359-370.

5. Paluch EK, Rac E, et al., The role and regulation of blebs in cell migration. Curr Opin Cell Biol. 2013:5:582-590.

6. Julian L, Olson MF. Apoptotic membrane dynamics in health and disease. Cell Health and Cytoskeleton. 2015:7:133-142.

7. Khajah MA, Lugmani YA. Involvement of Membrane Blebbing in Immunological Disorders and Cancer. Med Princ Pract. 2015.

8. Guan BX, Bhanu B, Talbot P, et al. Extraction of blebs in human embryonic stem cell videos. IEEE Transactions on Computational Biology and Bioinformatics 2015a:99.

9. Guan B, Bhanu B, Talbot P, et al. Bio-inspired segmentation and detection methods for human embryonic stem cells. In: Video Bioinformatics: From Live Imaging to Knowledge. Eds B. Bhanu and P. Talbot, Springer International Publishing Switzerland 2015b:7:135-150.

10. Boss J. Mitosis in cultures of newt tissues. IV. The cell surface in late anaphase and the movements of ribonucleoprotein. Exp. Cell Res. 1955:8:181–187.

11. Porter K, Prescott D, Frye J. Changes in surface morphology of Chinese hamster ovary cells during the cell cycle. J. Cell Biol. 1973:57:815–836.

12. Fishkind DJ, Cao LG, Wang YL. Microinjection of the catalytic fragment of myosin light chain kinase into dividing cells: effects on mitosis and cytokinesis. J. Cell Biol. 1991:114:967–975.

13. Boucrot E, Kirchhausen T. Endosomal recycling controls plasma membrane area during mitosis. Proc. Natl. Acad. Sci. U.S.A. 2007:104:7939–7944.

14. Hickson GRX. Echard A. O'Farrell PH. RHO kinase controls cell shape changes during cytokinesis. Curr Biol. 2006:16(4): 359-370.

15. Maekawa M, Ishizaki T, Boku S, et al. Signaling from Rho to the actin cytoskeleton through protein kinases ROCK and LIM-kinase. Science 1999:285(5429):895-8.

16. Paluch EK, Rac E, et al., The role and regulation of blebs in cell migration. Curr Opin Cell Biol. 2013:5:582-590.

17. Blaser, H. et al. Migration of zebrafish primordial germ cells: a role for myosin contraction and cytoplasmic flow. Dev. Cell. 2006:11:613-627.

18. Trinkaus, JP. Surface activity and locomotion of *Fundulus* deep cells during blastula and gastrula stages. Dev. Biol. 1973:30:69-103.

19. Wourms, JP. The developmental biology of annual fishes. II. Naturally occurring dispersion and reaggregation of blastomers during the development of annual fish eggs. J. Exp. Xppl. 1972:182:169-200.

20. Trinkaus, JP. Ingression during early gastrulation of Fundulus. Dev. Biol. 1996:177:356-370.

21. Holtfreter, J. Properties and functions of the surface coat in amphibian embryos. J. Exp. Zool. 1943:93:251-323.

22. Kubota KY. Creeping locomotion of the endodermal cells dissociated from gastrulae of the Japanese newt, Cynops pyrrhogaster. Exp. Cell Res. 1981:133:137-148.

23. Satoh N, Kageyama T, Sirakami KT. Motility of siddociated embryonic cells in Xenopus laevis: its significance to morphogenetic movements. Dev. Growth Diff. 1976:18:55-67.

24. Gebala V, Collins R, Geudens I, et al., Blood flow drives lumen formation by inverse membrane blebbing during angiogenesis in vivo. Nat Cell Biol. 2016:18(4):443-450.

25. Maugis B, Brugues J, Nassoy P, et al. Dynamic instability of the intracellular pressure drives bleb-based motility. J Cell Sci. 2010:123(Pt22): 3884-3892.

26. Laser-Azogul A, Diamant-Levi T, Israeli S, et al. Met-induced membrane blebbing leads to amoeboid cell motility and invasion. Oncogene. 2014:33(14):1788-1798.

27. Watanabe K, Ueno M, Kamiya D, et al. A ROCK inhibitor permits survival of dissociated human embryonic stem cells. Nat. Biotechnol. 2007:25:681–686.

28. Harb N, Archer TK, Sato N. The Rho-ROCK-Myosin signaling axis determines cell-cell integrity of self-renewing pluripotent stem cells. PLOS One 2008:3(8):e3001.

29. Li X, Krawetz R, Liu S, et al. ROCK inhibitor improves survival of cryopreserved serum/feeder-free single human embryonic stem cells. Hum Raprod. 2009:24(3):580-589.

30. Ohgushi M, Matsumura M, Eiraku M, et al. Molecular pathway and cell state responsible for dissociation-induced apoptosis in human pluripotent stem cells. Cell Stem Cell. 2010:7(2):225-239.

31. Ikenouchi J, Aoki K. Membrane bleb: a seesaw game of two small GTPase. Semall GTPases. 2016:17:1-5.

32. Aoki K, Maeda F, Nagasako T, et al. A RhoA and Rnd3 cycle regulates actin reassembly during membrane blebbing. Proc Natl Acad Sci U S A. 2016:113(13):E1863-1871.

33. Weng NJH, Phandthong R, Talbot P. A video bioinformatics method to quantify cell spreading and its application to cells treated with Rho-associated protein kinase and blebbistatin. Video Bioinformatics Editors B. Bhanu and P. Talbot. Springer, 2015:ch8:151-166.

34. Volonte C, Apolloni S, Skaper SD, et al. P2X7 receptors: channels, pores and more. CNS Neurol Disord Drug Targets. 2012:11(6):705-721.

35. Panupinthu N, Zhao L, Possmayer F, et al. P2X7 nucleotide receptors mediate blebbing in osteoblasts through a pathway involving lysophosphatidic acid. J Biol Chem. 2007:282(5):3403-3412.

36. Nicotera P, Hartzell P, Davis G, et al. The formation of plasma membrane blebs in hepatocytes exposed to agents that increase cytosolic Ca2+ is mediated by the activation of a non-lysosomal proteolytic system. FEBS Lett. 1986:209(1):139-144.

37. Zheng LM, Zychlinsky A, Liu CC, et al. Extracellular ATP as a trigger for apoptosis or programmed cell death. J Cell Biol. 1991:112(2):279-288.

38. Verhoef PA, Estacion M, Schilling W. P2X7 receptor-dependent blebbing and the activation of Rho-effector kinases, caspases, and IL-1β release. J Immunol. 2003:170(11):5728-5738

39. Lin S. and Talbot P. Methods for culturing mouse and human embryonic stem cells. Methods Mol Biol 2011;690:31-56.

40. Behar RZ, Bahl V, Wang Y, et al. A method for rapid dose-response screening of environmental chemicals using human embryonic stem cells. J. Pharmacological Toxicological Methods. 2012:66(3):238-45.

41. Bahl V, Johnson K, Phandthong R, et al., Thirdhand Cigarette Smoke Causes Stress-Induced Mitochondrial Hyperfusion and Alters the Transcriptional Profile of Stem Cells. Toxicol Sci. 2016:kfw102.

42. Talbot P, zur Nieden N, Lin S, et al. Use of video bioinformatics tools in stem cell toxicology. Handbook of Nanomedicine, Nanotoxicology and Stem Cell Use in Toxicology. John Wiley & Sons, Ltd, Chichester, UK. 2014:ch21.

43. Fujimura M, Usuki F, Kawamura M, et al. Inhibition of the RHO/ROCK pathway prevents neuronal degeneration in vitro and in vivo following methylmercury exposure. Toxicol Appl Phamacol 2011:250(1):1-9.

44. Ratz PH, Miner AS, Barbour SE. Calcium-independent phospholipase A2 participates in KCl-induced calcium sensitization of vascular smooth muscle. Cell Calcium. 2009:46(1):65-72.

45. Frisca F, Crombie DE, Dottori M, et al. Rho/ROCK pathway is essential to the expansion, differentiation, and morphological rearrangements of human neural stem/progenitor cells induced by lysophosphatidic acid. J Lipid Res. 2013:54(5):1192-1206.

46. Bulanova E, Budagian V, Orinska Z, et al. ATP induces P2X7 receptor-independent cytokine and chemokine expression through P2X1 and P2X3 receptors in murine nast cells. J Leukoc Biol. 2009:85(4):692-702.

47. Adinolfi E, Callegari MG, Ferrari D, et al. Basal activation of the P2X7 ATP receptor elevates mitochondrial calcium and potential, increases cellular ATP levels, and promotes serum-independent growth. Mol Biol Cell. 2005:16(7):3260-3272.

48. Giannuzzo A, Pedersen SF, Novak I. The P2X7 receptor regulates cell survival, migration and invasion of pancreatic ductal adenocarcinoma cells. Mol Cancer. 2005:14:203.

49. Coutinho-Silva R, Persechini PM, Bisaggio RD, et al. P2Z/P2X7 receptor-dependent apoptosis of dendritic cells. Am J Physiol. 1999:276(5Pt1)C1139-1147.

50. Hickman SE, Khoury JEL, Greenberg S, et al. P2Z adenosine triphosphate reveptor activity in cultured human monocyte-derived macrophages. Blood. 1994:84:2452-2456.

51. Brough D, Le Feuvre RA, Iwakura Y, et al. Purinergic(P2X7) receptor activation of microglia induces cell death via an interleukin-1-independent mechanism. Mol Cell Neurosci. 2002:19(2):272-280.

52. Cotrina ML, Nedergaard M. Physiological and pathological functions of P2X7 receptor in the spinal cord. Purinergic Signal. 2009:5(2):223-232.

53. Coutinho-Silva R, Correa G, Sater AA, et al. The P2X7 receptor and intracellular pathogens: a continuing struggle. Purinergic Signal. 2009:5(2):197-204.

54. Wakx A, Dutot M, Massicot F, et al. Amyloid β Peptide Induces Apoptosis Through P2X7 Cell Death Receptor in Retinal Cells: Modulation by Marine Omega-3 Fatty Acid DHA and EPA. Appl Biochem Biotechnol. 2016:178(2):368-381.

55. Glaser T, de Oliveira SL, Cheffer A. Modulation of mouse embryonic stem cell proliferation and neural differentiation by the P2X7 receptor. PLOS One. 2014:9(5):e96281.

56. Parri M, Chiarugi P. Rac and Rho GTPases in cancer cell motility control. Cell Commun Signal. 2010:8:23.

57. Sander EE, ten Klooster JP, van Delft S, et al. Rac downregulates Rho activity: reciprocal balance between both GTPases determines cellular morphology and migratory behavior. J Cell Biol. 1999:147(5):1009-1022.

58. Blaser, H. et al. Migration of zebrafish primordial germ cells: a role for myosin contraction and cytoplasmic flow. Dev. Cell. 2006:11:613-627.

59. Trinkaus, JP. Surface activity and locomotion of *Fundulus* deep cells during blastula and gastrula stages. Dev. Biol. 1973:30:69-103.

60. Wourms, JP. The developmental biology of annual fishes. II. Naturally occurring dispersion and reaggregation of blastomers during the development of annual fish eggs. J. Exp. Xppl. 1972:182:169-200.

61. Trinkaus, JP. Ingression during early gastrulation of Fundulus. Dev. Biol. 1996:177:356-370.

62. Fackler OT, Grosse R. Cell motility through plasma membrane blebbing. J Cell Biol. 2008:181(6):879-884.

63. Ohgushi M, Sasai Y. Lonely death dance of human pluripotent stem cells: ROCKing between metastable cell states. Trends Cell Biol. 2011:(5):274-282

64. Ohgushi M, Matsumura M, Eiraku M, et al. Molecular pathway and cell state responsible for dissociation-induced apoptosis in human pluripotent stem cells. Cell Stem Cell. 2010:7(2):225-239.

Chapter 5: Conclusion

Key findings

Chapter 2: A video bioinformatics method was developed to quantify cell spreading in time-lapses videos using CL-Quant image analysis software. The cell spreading assay introduced in this chapter provides a rapid method for evaluating both the rate and fold change of spreading in hESC. We used the cell spreading assay to show that hESC treated with ROCKi have a stressed morphology when spreading on Matrigel. The stressed appearance of the ROCKi-treated cells suggests these inhibitors have strong off target effects and adversely alter their cytoskeleton. The use of ROCK inhibitors is not recommended in toxicological applications of hESC. The data obtained in this study indicate that better methods are needed to facilitate cell attachment and spreading during hESC passaging.

Chapter 3: This chapter shows that hESC produced more dynamic blebs and blebbed longer than other cell types and further demonstrates that dynamic blebbing interferes with attachment and survival of hESC during passaging. Cells that fail to attach eventually undergo apoptotic blebbing and die. This study is the first to show that dynamic and apoptotic blebbing were morphologically and temporally distinct. We showed that these two types of blebbing also differed in their rates of retraction, bleb intensity, assembly of cytoskeletal proteins, and distribution of organelles during blebbing. In this chapter, we summarized our data comparing dynamic and apoptotic blebbing in freshly plated hESC. When bundles of cortical actin became thin, the plasma membrane detached from the actin and blebs formed. During bleb expansion, ezrin remained associated with the bleb membrane, and actin was not attached to ezrin at this time. As the bleb expanded, actin moved into the bleb, attached to ezrin, and

reassembled under the bleb membrane. In dynamic blebbing, myosin reassembled with actin in the bleb, and their contraction causes bleb retraction. In apoptotic blebs, actin and myosin were fragmented, less abundant, or absent, which may account for their slower retraction.

Dynamic blebbing has important consequences for cultured hESC. First, cells that are dynamically blebbing cannot attach to their matrix until blebbing stops. Secondly, cells that are dynamically blebbing appear stressed and often shed part of their cytoplasm. ROCKi (Y27632) is often used to help hESC attach and spread rapidly; however, ROCKi treated cells often appear stringy and stressed and ROCKi may have off target effects. We showed that plating hESC on laminin-521, a biological molecule found in the inner cell mass, signals through an integrin-FAK pathway to stop dynamic blebbing and accelerate attachment. For hESC culture, plating on laminin-521 or Matrigel with an overlay of laminin-111 improves cell attachment and survival by reducing dynamic blebbing and enables efficient plating of single cells, while concurrently incubating in conditions that resemble the cells' natural *in vivo* environment without inhibitors that may have unwanted effects.

Chapter 4: During passaging, hESC undergo rapid dynamic blebbing that prevents attachment and spreading of cells. If dynamic blebbing does not stop, cells fail to attach, and eventually undergo apoptosis. Dynamic blebbing, which appears to stress cells and may cause loss of cytoplasm, can be stopped rapidly when laminins are used as the substrate for attachment. Binding of laminin to hESC integrins activates a FAK, and signaling through the FAK leads to cessation of blebbing.

In this study, we demonstrated that activation of P2X7 receptors by extracellular ATP released during passaging initiates dynamic blebbing in hESC and further identifies

targets that could be used to prevent P2X7 activation and subsequent dynamic blebbing. We showed that P2X7 activation enables calcium influx which in turn initiates blebbing, through activation of the Rho pathway. In this chapter, we showed dynamic blebbing was decreased by minimizing the release of ATP during passaging by using reagents such as apyrase that hydrolyze extracellular ATP. Also, we demonstrated that inclusion of a chelating agent (EGTA) helped reduce dynamic blebbing, but may also interfere with cell attachment. We found that P2X7 inhibitors (e.g., KN62) significantly reduced dynamic blebbing and accelerated cell attachment in hESC. Unlike ROCKi, KN62 did not alter hESC morphology or cause cells to appear stressed. Moreover, the P2X7 inhibitor did not affect proliferation during the first 24 hours of hESC culture.

Taken together, we have shown that regulation of dynamic blebbing is a key to improving hESC culture. Survival of hESC was increased when dynamic blebbing was controlled during passaging. Characterization of the pathways that initiate and stop dynamic blebbing has led to the identification of targets that can be used to control blebbing during cell culture. By controlling dynamic blebbing, it is possible to minimize stress, improve survival and efficiency during passaging, and passage single cells. These factors will be critical in developing culturing protocols suitable for using human pluripotent stem cells in therapeutic applications.

Summary

This dissertation deals specifically with dynamic blebbing, which is robust in hESC. Dynamic blebbing, which is observed in healthy cells, often occurs in *vitro* during the first hour after cell plating and before cell attachment and spreading on adherent substrates.

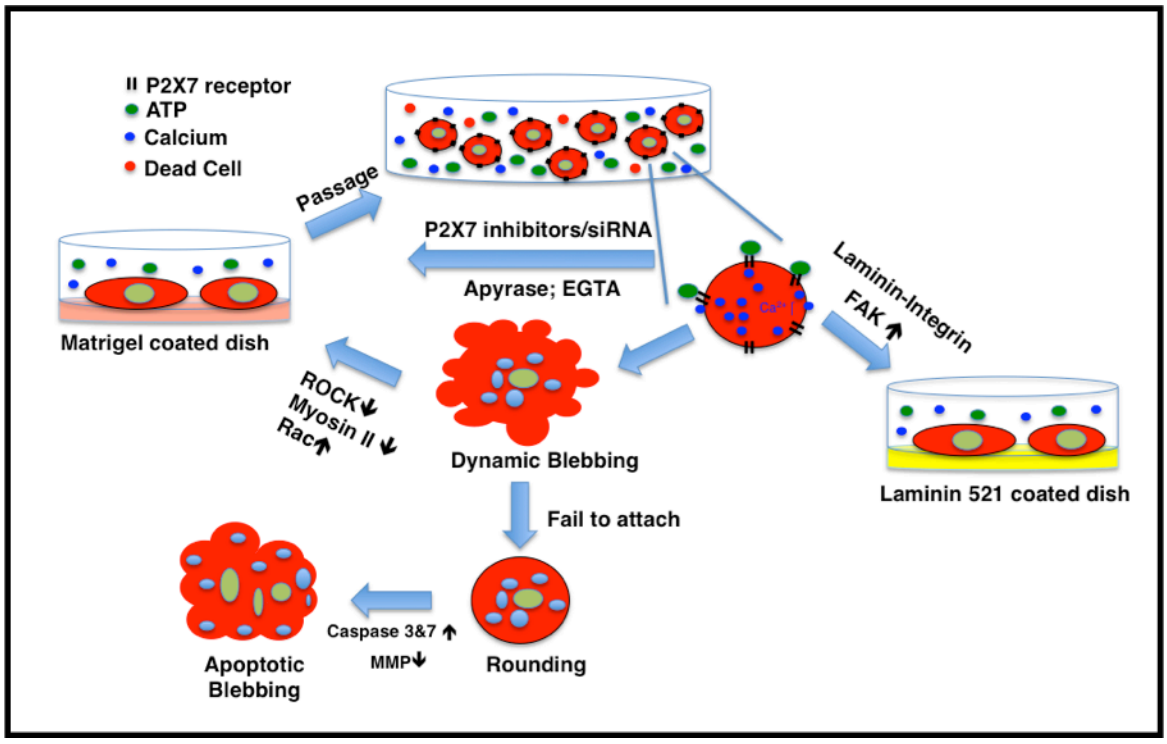

Figure 5.1: Diagram summarizing the main findings of this dissertation

Dynamic blebs are also found at the leading edge of migrating cells, where they drive cell movement. The difference between dynamic and apoptotic blebbing has been distinguished in hESC in this dissertation. Figure 5.1 is the graphic summary of the key findings of this dissertation. Single hESC culture can be improved by blocking the P2X7 signaling pathway using P2X7 inhibitors/siRNA or by hydrolyzing extracellular ATP or chelating the calcium in the culture medium. In cases where blebbing is occurring, it can

be stopped by plating hESC on Laminin 521, which activates a FAK leading to cessation of bleb formation.

These results identify targets that can be used to improve hESC culture. For example the use of a P2X7 inhibitor in conjunction with plating on laminin 521 would minimize dynamic blebbing and facilitate cell attachment and spreading. This strategy also permits the plating of single hESC, which can then be used in quantitative studies involving drugs or toxicants. The work presented here also establishes hESC as an excellent model for studying the process of dynamic blebbing. Because hESC are similar to epiblast cells in the post implantation embryo, it would also be possible to use blebbing hESC to better understand the motile forces involved in gastrulation.

Appendix

The following papers were done in collaboration with Ben Guan and Dr. Bir Bhanu while I was a NSF IGERT Fellow.

Appendix A: Bio-Inspired Segmentation and Setection Methods for Human Embryonic Stem Cells

Appendix B: Comparison of Texture Features for Human Embryonic Stem Cells with Bio-Inspired Multi-Class Support Vector Machine

Appendix C: Extraction of Blebs in Human Embryonic Stem Cell Videos

Chapter 7
Bio-Inspired Segmentation and Detection Methods for Human Embryonic Stem Cells

Benjamin X. Guan, Bir Bhanu, Prue Talbot and Nikki Jo-Hao Weng

Abstract This paper is a review on the bio-inspired human embryonic stem cell (hESC) segmentation and detection methods. Five different morphological types of hESC have been identified: (1) unattached; (2) substrate-attached; (3) dynamically blebbing; (4) apoptotically blebbing; and (5) apoptotic. Each type has distinguishing image properties. Within each type, cells are also different in size and shape. Three automatic approaches for hESC region segmentation and one method for unattached stem cell detection are introduced to assist biologists in analysis of hESC cell health and for application in drug testing and toxicological studies.

7.1 Introduction

In recent years, human embryonic stem cells (hESCs) have been used to assay toxicity of environmental chemicals [1–5]. The hESCs are one of the best models currently available for evaluating the effects of chemicals and drugs on human prenatal development [6]. The hESCs also have the potential to be a valuable model

B.X. Guan (✉) · B. Bhanu
Center for Research in Intelligent Systems, University of California,
Winston Chung Hall Suite 216, 900 University Ave., Riverside, CA 92507, USA
e-mail: xguan001@ucr.edu

B. Bhanu
e-mail: bhanu@ee.ucr.edu

P. Talbot
Department of Cell Biology and Neuroscience, University of California,
2320 Spieth Hall, 900 University Avenue, Riverside, CA 92507, USA
e-mail: talbot@ucr.edu

N.J.-H. Weng
Department of Cell Biology and Neuroscience, University of California,
2313 Spieth Hall, 900 University Avenue, Riverside, CA 92507, USA
e-mail: jweng002@ucr.edu

B. Bhanu and P. Talbot (eds.), *Video Bioinformatics*,
Computational Biology 22, DOI 10.1007/978-3-319-23724-4_7

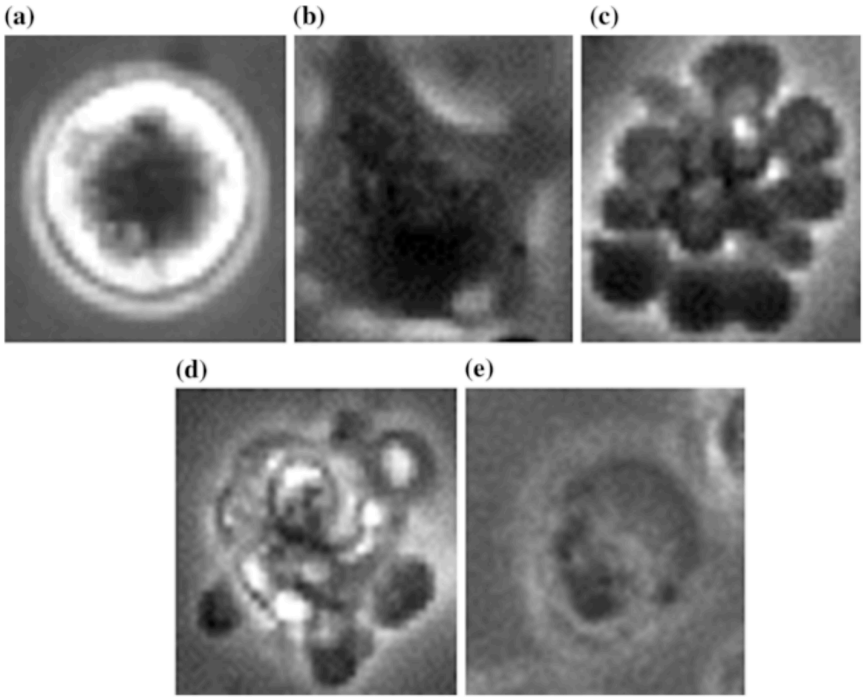

Fig. 7.1 **a** Unattached single stem cell; **b** substrate-attached single stem cell; **c** dynamically blebbing stem cell; **d** apoptotically blebbing stem cell; **e** apoptotic stem cell

for testing drugs before clinical trial. Equally important, the hESCs can potentially be used to treat cancer and degenerative diseases such as Parkinson's disease, Huntington's disease, and type 1 diabetes mellitus [6, 7].

Figure 7.1 shows five different morphological types of hESCs: (1) unattached single stem cell; (2) substrate-attached single stem cell; (3) dynamically blebbing stem cell; (4) apoptotically blebbing stem cell; and (5) apoptotic stem cell. As shown in Fig. 7.1, the inconsistency in intensities and shapes make the segmentation difficult when more than two types of cells are present in a field. Therefore, we have used bio-inspired segmentation and detection method to automate the analysis of hESCs.

Despite the enormous potential benefits of the hESC model, large-scale analysis of hESC experiments presents a challenge. Figure 7.2 shows an example of stem cell images at different magnifications. The analysis of hESCs is either semi-automated or manual [8]. CL-Quant software (DRVision Technologies) is an example of current state-of-the-art software for cell analysis, and it offers a semi-automatic approach. It requires users to develop protocols which outline or mask the positive and negative samples of stem cells using a soft matching procedure [9]. It usually takes an expert biologist 5–6 min of protocol making. The

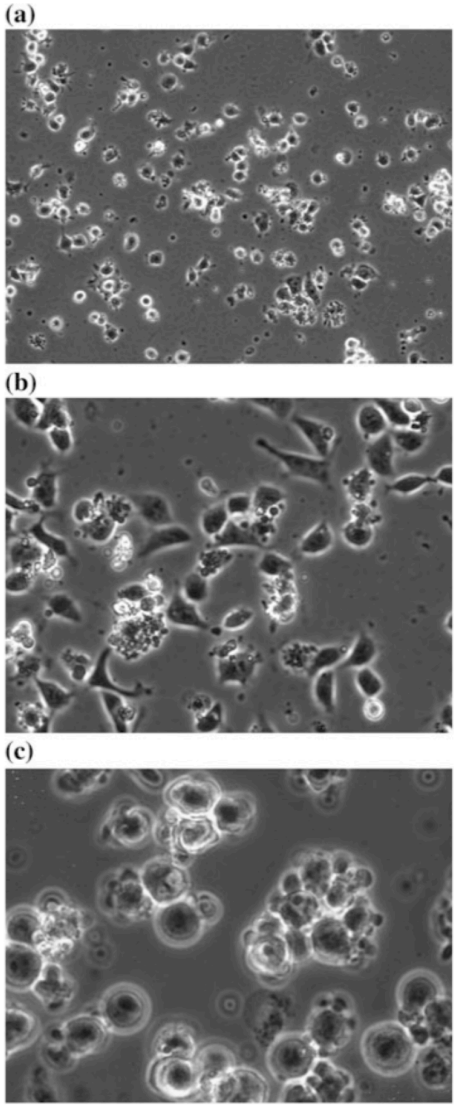

Fig. 7.2 **a** Image of hESCs taken with 10× objective; **b** Image of hESCs taken with 20× objective; **c** Image of hESCs taken with 40× objective

protocols are generally more accurate in the sample videos where the positive and negative samples are derived [8]. The segmentation accuracy of the software is also depended on the number of positive and negative samples. Although the software requires users to make protocols, it is a better alternative than analyzing the stem cells manually. Since there is no existing software for bleb detection and bleb counts, biologists often analyze frame by frame to determine the number of blebs in a video. Therefore, automatic segmentation and detection methods are essential for the future development of fast quantifiable analysis of hESCs.

In this paper, we will review bio-inspired automatic hESC region segmentation and unattached stem cell detection methods. Segmentation is a gateway to automated analysis of hESCs in biological assays. For example, the segmented results from those methods make automatic unattached single stem cell detection possible [10]. The detection of unattached stem cells is important in determining whether the cell is reactive to test chemicals. If the percentage of unattached stem cells is higher than attached stem cells, then the test chemical inhibited attachment and probably killed the cells that are unattached.

7.2 Related Work

There are two previous works for cell region detection in phase contrast images [11, 12]. Ambriz-Colin et al. [11] discuss two segmentation methods in this paper: (1) segmentation by pixels intensity variance (PIV); and (2) segmentation by gray level morphological gradient (GLMG). The PIV method performs pixel classification on the normalized image. It recognizes the probable cell regions and labels the rest as the background in the normalized image. The GLMG method detects the cell regions using morphological gradient that is calculated from the dilation and erosion operations, and by a threshold that separates the pixels belonging to a cell and to the background. Li et al. [12] use a histogram-based Bayesian classifier (HBBC) for segmentation. Li et al. [12] discuss a combined use of morphological rolling-ball filtering and a Bayesian classifier that is based on the estimated cell and background gray scale histograms to classify the image pixels into either the cell regions or the background.

In this paper, we also touch upon segmentation methods such as k-means and mixture of Gaussians by expectation–maximization (EM) algorithm. These approaches are widely used techniques in image segmentation. The k-means segmentation by Tatiraju et al. [13] considers each pixel intensity value as an individual observation. Each observation is assigned to a cluster with the mean intensity value nearest to the observation [14, 15]. The intensity distribution of its clusters is not considered in the partition process. However, the mixture of Gaussians segmentation method by the EM (MGEM) algorithm proposed by Farnoosh et al. [16] uses intensity distribution models for segmentation. The MGEM method uses multiple Gaussians to represent intensity distribution of an image [7, 13, 17, 18]. However, it does not take into account the neighborhood information. As the result, segmented regions obtained by these algorithms lack connectivity with pixels within their neighborhoods. Their lack of connectivity with pixels within their neighborhoods is due to the following challenges:

(1) incomplete halo around the cell body.
(2) intensity similarity in cell body and substrate.
(3) intensity sparsity in cell regions.

Our proposed method is intended to solve these problems using spatial information of the image data. We evolve the cell regions based on the spatial information until the optimal optimization metric value is obtained. The proposed methods are developed with three criteria: (1) robustness; (2) speed; and (3) accuracy.

The existing papers often detect cells in phase contrast images in a simple environment [19, 20]. Eom et al. [19] discuss two methods for cell detection: detection by circular Hough transform (CHT) and detection by correlation. However, those methods do not work on the complex environment where the occurrence of dynamic blebbing and existence of overlapping cells are prevalent. The CHT is sensitive to the shape variations, and the correlation method in [20] does not work on cell clusters. Therefore, a detection method based on the features derived from inner cell region is developed to solve the aforementioned problem in unattached single stem cells detection.

7.3 Technical Approach

The segmentation approaches reviewed in this paper range from simple to complex and efficient to inefficient. Even though spatial information is used in all three segmentation methods, the derivation of spatial information in each method is different. In addition, we also provide a review on the unattached single stem cell detection method. The segmentation and detection methods are discussed in the following order.

1. Gradient magnitude distribution-based approach
2. Entropy-based k-means approach
3. Median filter-induced texture-based approach
4. Unattached single stem cell detection

7.3.1 Gradient Magnitude Distribution-Based Approach

The approach in [21] iteratively optimizes a metric that is based on foreground (F) and background (B) intensity statistics. The foreground/hESC region, F, is a high intensity variation region while the background/substrate region, B, is a low intensity variation region. Therefore, we can use the magnitude of gradients of the image to segment out the cell region from the substrate region. Equations (7.1) and (7.2) show the calculation of spatial information.

$$G = \left(\frac{\mathrm{d}I}{\mathrm{d}x}\right)^2 + \left(\frac{\mathrm{d}I}{\mathrm{d}y}\right)^2 \tag{7.1}$$

$$I_{\mathrm{mg}} = \log_{\mathrm{e}}\left(\frac{(-1+e^1)\times G}{\max(G)} + 1\right) \times 255 \tag{7.2}$$

where G is the squared gradient magnitude of image, I. $\frac{\mathrm{d}I}{\mathrm{d}x}$ and $\frac{\mathrm{d}I}{\mathrm{d}y}$ are gradients of image, I, in the x and y directions. I_{mg} is the spatial information and the log transform further emphasizes the difference between cell and substrate region. Equation (7.2) normalizes G as well as transforms the image into a bimodal image. Therefore, a single threshold can segment the transformed image into cell region and substrate region.

The proposed approach uses a mean filter on I_{mg} iteratively to evolve the cell regions. It is able to group the interior cell region pixels together based on the local information. The method updates I_{mg} and evolves the cell region until optimization metric in [21] is maximized. The window size of the mean filter contributes to how fast the cell region is evolved. The transformed image is iteratively thresholded by Otsu's algorithm. The parameters for the optimization metric are also updated iteratively.

7.3.2 *Entropy-Based K-Means Approach*

The approach mentioned in [22] utilizes the k-mean algorithm with weighted entropy. The cell regions generally have higher entropy values than the substrate regions due to their biological properties. However, not all cell regions have high entropy values. Therefore, the approach exploits intensity feature to solve the following problems: (1) intensity uniformity in some stem cell bodies; and (2) intensity homogeneity in stem cell halos. Since high entropy values happen in areas with high varying intensities, the aforementioned properties can greatly affect the cell region detection. Therefore, the method in [22] proposed a weighted entropy formulation. The approach uses the fact that stem cell image has an intensity histogram similar to a Gaussian distribution. Moreover, the stem cell consists of two essential parts: the cell body and the halo [6]. The cell bodies and halos' intensity values are located at the left and right end of the histogram distribution, respectively. As the result, regions with low or high intensity values have a higher weight. The background distribution is represented by the following equation:

$$D_{\mathrm{bg}} \sim N_{256}(\mu, \sigma^2) \tag{7.3}$$

where D_{bg} is a Gaussian distribution of background with mean, μ, and variance, σ^2, and $D_{\mathrm{bg}} \in \mathcal{R}^{256}$. The foreground distribution is shown in Eq. (7.4).

$$\mathcal{W} = \text{Max}(D) - D \tag{7.4}$$

The weighted entropy is calculated by Eq. (7.5):

$$I_{\mathbf{we}}(r,c) = \log\left(1 + E(r,c) \times \sum_{(y,x)\in \boldsymbol{W}} \mathcal{W}(I(y,x))^2\right) \tag{7.5}$$

where $I_{\text{we}}(r,c)$ is the weighted entropy at the location (r,c) with $r,c \in \mathcal{R}$. $E(r,c)$ is the un-weighted entropy value of the image's gradient magnitude at location (r,c), and $I(y,x)$ is the intensity value at location (y,x). $x,y \in \mathcal{R}$, and W is the set of neighboring coordinates of (r,c). $\sum_{(y,x)\in \boldsymbol{W}} \mathcal{W}(I(y,x))^2$ is the spatial energy term. Equation (7.5) enhances the separation between cell/foreground and substrate/background regions. The normalization of I_{we} back into a 8-bit image is shown in Eq. (7.6):

$$I_{\text{wen}} = \frac{(I_{\text{we}} - \min(I_{\text{we}}))}{(\max(I_{\text{we}}) - \min(I_{\text{we}}))} \times 255 \tag{7.6}$$

7.3.3 *Median Filter-Induced Texture-Based Approach*

The segmentation method by Guan et al. [23] combines the hESC spatial information and mixture of Gaussians for better segmentation. The mixture of Gaussians alone does not able to segment the cell regions from the substrate due to its lack of spatial consistency. The cell region intensities lie on both left and right end of the image histogram. However, the mixture of Gaussians can accurately detect fragments of the cell regions. Therefore, it can serve as a good template to find the optimal threshold, T_{opt}, and filter window size, m, in the spatial transformed image for cell region detection. As a result, we exploited the spatial information due to the biological properties of the cells in the image and used the result from the mixture of Gaussians as a comparison template [23].

With the spatial information, we can easily distinguish the cell region from the substrate region. The spatial information is generated with the combination of median filtering. A spatial information image I_S at scale m in [23] is calculated by the following equation:

$$I_{\text{mf}}(m) = med(|I - med(I,m)|, m+2) \tag{7.7}$$

where $med(\cdot,m)$ denotes the median filtering operation with window size m. The operation $|I - med(I,m)|$ yields low values in the substrate region and high values in the cell regions. The larger median filter window connects the interior cell regions while preserving the edges. The transformation of the image, I, by Eq. (7.7)

generates a bimodal image from an original image that contains three intensity modes. Therefore, we can use the result from the mixture of Gaussians to find T_{opt} and m_{opt}. The cell region detection is done by finding the maximum correlation coefficient value between the results from the mixture of Gaussian and the spatial information at various T and m. The filter window size, m, varies from 3 to 25 with a step size of 2. The threshold T is from the minimum to the maximum of the spatial information image in steps of 0.5.

7.3.4 Unattached Single Stem Cell Detection

The unattached single stem cell detection by Guan et al. [10] is a feature-based classification that utilizes detected inner cell region features. The inner cell region is derived from thresholding the normalized probability map. The feature vector contains area size, eccentricity, and convexity of the inner cell region. We use the Euclidean distance as the classification measure. The Euclidean distances of the target's feature vector and the feature vectors in the training data are calculated by

$$K_f(i) = \begin{cases} \frac{1}{J}\sqrt{\sum_j K_{\text{Coef}}(i,j)^2}\sqrt{\sum_j K_{\text{Coef}}(i,j)^2} \leq J \\ 1 \qquad\qquad\qquad\qquad \text{else} \end{cases} \tag{7.8}$$

The symbol $K_f(i)$ is the Euclidean distance of the target feature vector and feature vectors from the training data where $i \in \mathbb{R}$. $K_{\text{Coef}}(i,j)$ is a matrix that contains the differences of the target feature vector and feature vectors in the training data. Variable J is equal to $\sqrt{3}$ and $j \in \{1,2,3\}$ since we have three features in our classification method.

7.4 Experimental Result

In this subsection, we briefly discuss the experimental results for each aforementioned approach.

7.4.1 Data

All time lapse videos were obtained with BioStation IM [1]. The frames in the videos are phase contrast images with 600 × 800 resolutions. The videos are acquired using three different objectives: 10×, 20×, and 40×.

7.4.2 Metrics

The true positive, TP, is the overlapped region between the binary image of detected cell regions and its ground-truth. True negative, TN, is the overlapped region between the binary image of detected background region and its ground-truth. The false positive, FP, is the detected background in the background binary image that is falsely identified as part of the cell region in cell region binary image. The false negative, FN, is the detected cell region in cell region binary image that is falsely identified as part of the background in the background binary image [24].

The true positive rate or sensitivity, TPR, measures the proportion of actual positives which are correctly identified.

$$TPR = \frac{TP}{(TP + FN)} \tag{7.9}$$

The false positive rate, FPR, measures the proportion of false positives which are incorrectly identified.

$$FPR = \frac{FP}{(FP + TN)} \tag{7.10}$$

7.4.3 Gradient Magnitude Distribution-Based Approach

The gradient magnitude distribution approach has more than 90 % average sensitivity and less than 15 % average false positive rate for all datasets that are not corrupted by noise [21]. The high performance remained after filtering is done on the noisy dataset. The dataset taken with 40× objective is corrupted by noise, and the proposed method has lower performance without filtering as shown in Tables 7.1 and 7.2. Tables 7.1 and 7.2 also show comparison of the proposal

Table 7.1 Average sensitivity

Method	10× (%)	20× (%)	40× (%)	40×[a] (%)
Guan [21]	95.85	95.65	75.09	90.42
KM	51.92	51.83	79.66	40.26
M2G	79.27	80.54	63.56	80.99

[a]filtered data

Table 7.2 Average false positive rate

Method	10× (%)	20× (%)	40× (%)	40×[a] (%)
Guan [21]	14.64	13.33	3.18	7.22
KM	4.41	5.95	30.18	0.46
M2G	11.57	14.10	3.63	9.37

[a]filtered data

method with k-means (KM) and mixture of two Gaussians (M2G). KM method performs the worst in all three methods. The proposed method's average sensitivity is higher than M2G by at least 10 % in all datasets.

7.4.4 Entropy-Based K-Means Approach

In this approach, we also compare the proposed method with k-means. However, the initial means for each cluster are assigned based on our knowledge for each cluster. Therefore, KM in this approach has significant lower false positive rate in all datasets. The entropy and k-means based on segmentation has more than 80 % average sensitivity and less than 16 % average false positive rate [22]. Table 7.3 shows that the proposed method has above 96 % average sensitivity except for the unfiltered 40× dataset. Table 7.4 shows that KM has lower average false positive rate, but it is due to the fact that it detect all pixels as background.

7.4.5 Median Filter-Induced Texture-Based Approach

The median filter-induced texture-based approach has tested only on the six datasets taken with 20× objective. The approach has more than 92 % average sensitivity and less than 7 % average false positive rate [23]. The means of all six datasets in average sensitivity and average false positive rate are 96.24 and 5.28 %. As shown in Table 7.5, mixture of two Gaussians and mixture of three Gaussians methods have the lowest average sensitivities. Even though other methods have the mean average sensitivities above 94 %, they have high false positive rate as shown in Table 7.6. Their mean average false positive rates are above 17 %.

7.4.6 Unattached Single Stem Cell Detection

The unattached single stem cell detection approach was tested on four datasets taken under 20× objective [10]. Figure 7.3 shows an ROC plots for four different

Table 7.3 Average sensitivity

Method	10× (%)	20× (%)	40× (%)	40×[a] (%)
Guan [22]	98.09	96.73	80.82	96.18
KM	37.76	38.37	40.28	40.28

[a]filtered data

Table 7.4 Average false positive rate

Method	10× (%)	20× (%)	40× (%)	40×[a] (%)
Guan [22]	19.21	17.81	5.83	15.68
KM	1.77	2.51	0.61	0.61

[a]filtered data

Table 7.5 Average sensitivity

Video	HBBC (%)	GLMG (%)	PIV (%)	M2G (%)	M3G (%)	Guan [23] (%)
1	92.08	97.08	98.90	43.52	53.16	94.30
2	84.95	93.80	97.37	29.88	42.18	92.31
3	98.46	98.89	99.80	70.46	78.14	97.67
4	99.27	98.78	99.54	79.85	87.33	98.38
5	97.07	97.66	98.82	77.38	84.40	97.25
6	97.81	98.17	99.23	74.88	81.15	97.54

Table 7.6 Average false positive rate

Video	HBBC (%)	GLMG (%)	PIV (%)	M2G (%)	M3G (%)	Guan [23] (%)
1	19.71	22.47	19.86	2.83	5.16	4.41
2	26.67	21.82	18.83	2.65	4.39	6.57
3	16.62	22.47	18.50	4.80	7.22	4.78
4	14.19	15.91	16.69	4.77	7.52	5.74
5	12.34	16.42	15.10	4.39	6.86	5.51
6	16.33	22.07	20.33	5.06	8.09	4.69

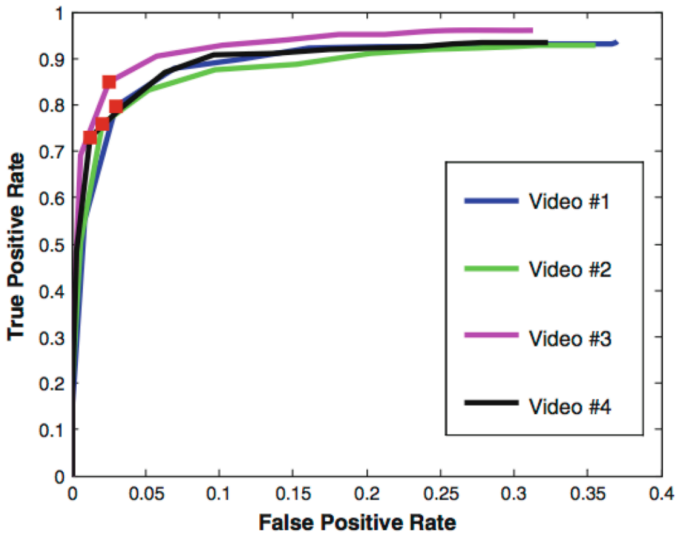

Fig. 7.3 True positive rate versus false positive rate (ROC curves) (*Note* the *red squares* are the optimal results of the proposed method)

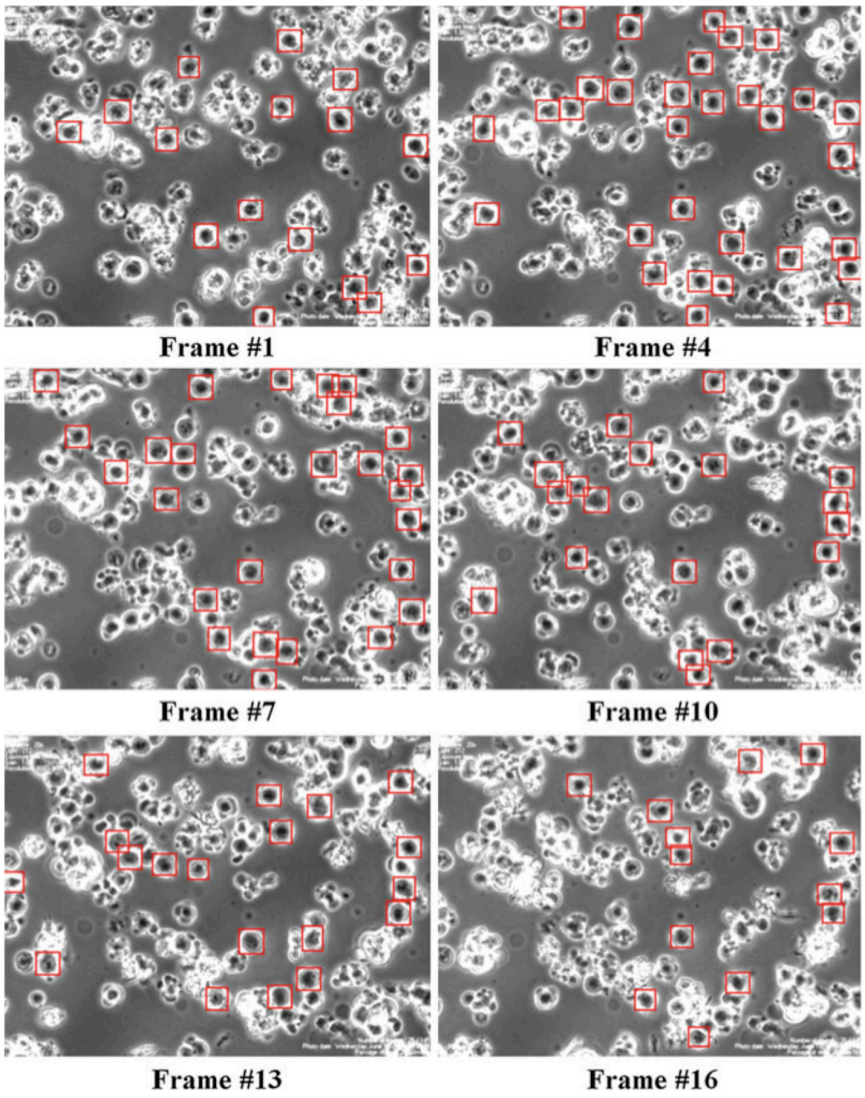

Fig. 7.4 A sample of results of unattached single stem cell detection approach

experiments. The proposed method achieves above 70 % in true positive while keeping the false positive rate below 2.5 %. Figure 7.4 shows the result of the proposed method on a sequence of images. The proposed method captured majority of the unattached single stem cells.

7.5 Performance Analysis

In this subsection, we evaluate the three aforementioned segmentation approaches mentioned above in terms of robustness, speed, and accuracy.

7.5.1 Robustness

The median filter-induced texture-based method in [23] was tested only on a 20× dataset with a set of parameters. Since the parameters are tuned for the 20× datasets, it is not reliable for datasets collected using different objectives as shown in Fig. 7.5. Most importantly, its performance is heavily depended on initial segmentation result of the mixture of Gaussians. The entropy-based k-means approach in [22] and the gradient magnitude distribution-based approach in [21] are more

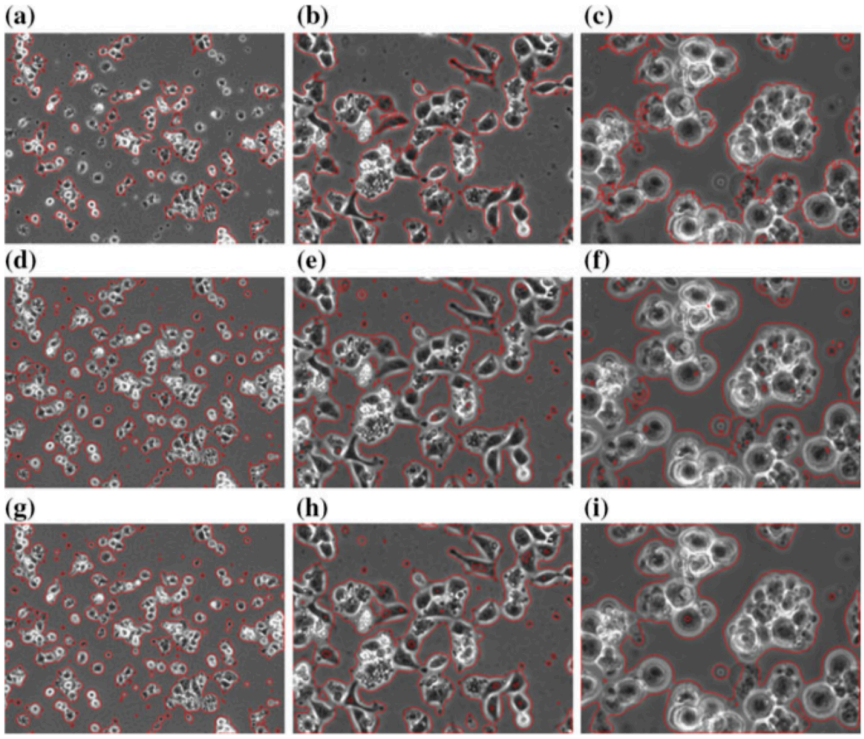

Fig. 7.5 **a–c** Median filter-induced texture-based method results for 10×, 20×, and 40× images respectively; (**d–f**) entropy-based k-means method results for 10×, 20×, and 40× images, respectively; (**g–i**) gradient magnitude distribution-based method results for 10×, 20×, and 40× images, respectively

robust with different objectives. Since both methods do not need a template to obtain the optimal segmentation, they are robust under different objectives with a same set of parameters.

7.5.2 Speed

The entropy-based k-means in [22] and gradient magnitude distribution-based in [21] approaches have only one optimization step. The median filter-induced texture-based method in [23] requires two optimization steps. However, the entropy-based k-means approach has higher time complexity than the other methods. The reason it is slow is because the method performs k-means clustering and entropy filtering for segmentation. The operations of k-means clustering and entropy filtering are extremely time consuming. Consequently, the approach's processing time is about 28 s/frame.

Since the median filter-induced texture-based method has two optimization steps, it also has high time complexity. The first optimization step is done to determine the initial segmentation result by the mixture of Gaussians. The second optimization step is done with the mixture of Gaussians result to obtain the final segmentation. Therefore, the approach's processing time is about 26 s/frame.

The gradient magnitude distribution-based approach only uses mean filtering and the Otsu's algorithm. Since mean filtering and Otsu's algorithm are faster operations, the method is the fastest among the aforementioned approaches. The gradient magnitude distribution-based segmentation only requires 1.2 s/frame of processing time. All experiments for each method are done on a laptop with an Intel (R) Core™ 2 Duo CPU processor that run at 2.53 GHz.

7.5.3 Accuracy

The entropy-based k-means approach has the highest average true positive rate (TPR) as well as the highest average false positive rate (FPR) [24]. It has a mean of about 97 % average TPR and near 18 % average FPR. Both median filter-induced texture-based and gradient magnitude distribution-based approaches have less than 12 % average false positive rate. However, the median filter-induced texture-based approach was only tested on the dataset taken with a 20× objective, and it had a mean of 96.24 % in average TPR. The gradient magnitude distribution-based method has a mean near 94 % in average TPR. Both entropy-based k-means and gradient magnitude distribution-based approaches were tested on datasets under different objectives.

7.6 Conclusion

This paper provides a brief review of three existing bio-inspired segmentation methods as well as a concise discussion on the unattached single stem cell detection method. All three segmentation approaches mentioned in this paper have above 90 % average true positive rate and less than 18 % average false positive rate in segmentation. However, the gradient magnitude distribution-based approach outperforms the other methods in the overall measures of robustness, speed, and accuracy. The gradient magnitude distribution-based approach has good detection results for images collected with all three objectives. It has smoother detected result than the other methods as shown in Fig. 7.5. In terms of speed, the method requires processing time of 1.2 s/frame. Compared to its counterparts, it is about 20 times faster when run in the same machine. In terms of accuracy, the gradient magnitude distribution-based method still has a mean near 94 % in average TPR and less than 12 % in average FPR. The unattached single stem cell detection makes possible with the accurate cell region segmentation. Therefore, the gradient magnitude distribution-based method is significant for the future development of fast quantifiable analysis of stem cells. The methods described in this chapter could be used to evaluate the health and viability of hESC cultures and the response of hESC to environmental changes or toxicants.

Acknowledgment This research was supported by National Science Foundation-Integrated Graduate Education Research and Training (NSF-IGERT): Video Bioinformatics Grant DGE 0903667 and by Tobacco-Related Disease Research Program (TRDRP): Grant 20XT-0118.

References

1. Stojkovic M, Lako M, Strachan T, Murdoch A (2004) Derivation, growth and applications of human embryonic stem cells. Reproduction 128:259–267
2. Lin S et al (2010) Comparison of the toxicity of smoke from conventional and harm reduction cigarettes using human embryonic stem cells. Toxicol Sci 118:202–212
3. Behar RZ, Bahl V, Wang Y, Lin S, Davis B, Talbot P (2012) A method for rapid dose-response screening of environmental chemicals using human embryonic stem cells. J Pharmacol Toxicol Methods. doi:10.1016/j.vascn.2012.07.003
4. Bahl BV, Lin S, Xu N, Davis B, Wang Y, Talbot P (2012) Comparison of electronic cigarette refill fluid cytotoxicity using embryonic and adult models. Reprod Toxicol 34(4):529–537
5. Behar RZ, Bahl V, Wang Y, Weng J, Lin S, Talbot P Adaptation of stem cells to 96-well plate assays: use of human embryonic and mouse neural stem cells in the MTT assay, Current Protocols, Chapter 1:Unit1C.13. doi:10.1002/9780470151808.sc01c13s23
6. Talbot P, Lin S (2011) Mouse and human embryonic stem cells: can they improve human health by preventing disease? Curr Top Med Chem 11(13):1638–1652
7. Lin S, Talbot P (2011) Methods for culturing mouse and human embryonic stem cells. Methods Mol Biol 690:31–56
8. Lin S et al (2010) Video bioinformatics analysis of human embryonic stem cell colony growth. JOVE 39, May 2010

9. Nikon (2013) CL-Quant. http://www.nikoninstruments.com/News/US-News/Nikon-Instruments-Introduces-CL-Quant-Automated-Image-Analysis-Software. Accessed July 2013
10. Guan BX, Bhanu B, Talbot P, Lin S (2012) Detection of non-dynamic blebbing single unattached human embryonic stem cells. In: IEEE international conference on image processing, Orlando, FL
11. Ambriz-Colin F, Torres-Cisneros M, Avina-Cervantes J, Saavedra-Martinez J, Debeir O, Sanchez-Mondragon J (2006) Detection of biological cells in phase-contrast microscopy images. In: Fifth mexican international conference on artificial intelligence, 2006. MICAI '06, pp 68 –77
12. Li K, Chen M, Kanade T (2007) Cell population tracking and lineage construction with spatiotemporal context. In: Proceedings of the 10th international conference on medical image computing and computer-assisted intervention (MICCAI), pp 295–302
13. Tatiraju S, Mehta A (2008) Image segmentation using k-means clustering, EM and normalized cuts, UC Irvine
14. Alsabti K, Ranka S, Singh V (1998) A efficient k-means clustering algorithm. In: Proceedings of first workshop on high performance data mining
15. Kanungo T, Mount DM, Netanyahu NS, Piatko CD, Silverman R, Wu AY (2002) An efficient k-means clustering algorithm: analysis and implementation. IEEE Trans PAMI 881–892
16. Farnoosh R, Zarpak B (2008) Image segmentation using Gaussian mixture model. Int J Eng Sci 19:29–32
17. Xu L, Jordan MI (1996) On convergence properties of the EM algorithm for Gaussian mixture. Neural Comp 129–151
18. Gopinath S, Wen Q, Thakoor N, Luby-Phelps K, Gao JX (2008) A statistical approach for intensity loss compensation of confocal microscopy images. J Microsc 230(1):143–159
19. Eom S, Bise R, Kanade T (2010) Detection of hematopoietic stem cells in microscopy images using a bank of ring filters. In: Proceedings of 7th IEEE international symposium on biomedical imaging, Rotterdam, Netherlands, pp 137–140
20. Miroslaw L, Chorazyczewski A, Buchholz F, Kittler R (2005) Correlation-based method for automatic mitotic cell detection in phase contrast microscopy. Adv Intell Soft Comput 30:627–634
21. Guan BX, Bhanu B, Talbot P, Lin S (2012) Automated human embryonic stem cell detection. In: IEEE 2nd international conference on healthcare informatics, imaging and systems biology, pp 75–82
22. Guan BX, Bhanu B, Thakoor N, Talbot P, Lin S (2013) Automatic cell region detection by K-means with weighted entropy. In: International symposium on biomedical imaging: From Nano to Macro, pp 418–421
23. Guan BX, Bhanu B, Thakoor N, Talbot P, Lin S (2011) Human embryonic stem cell detection by spatial information and mixture of Gaussians. In: Proceedings of 1st IEEE international conference on health informatics, imaging and system biology, San Jose, CA, pp 307–314
24. Pepe M, Longton GM, Janes H (2008) Comparison of receiver operating characteristics curves, UW Biostatistics Working Paper Series- Working Paper 323 [eLetter] January 2008. http://biostats.bepress.com/uwbiostat/paper323

COMPARISON OF TEXTURE FEATURES FOR HUMAN EMBRYONIC STEM CELLS WITH BIO-INSPIRED MULTI-CLASS SUPPORT VECTOR MACHINE

Benjamin X. Guan, Bir Bhanu, Prue Talbot, Sabrina Lin* and Nikki Weng**

Center for Research in Intelligent Systems, *Stem Cell Center
University of California, Riverside, CA 92521, USA
Email: {xguan001, bhanu}@ee.ucr.edu, {prue.talbot, sabrina.lin, jweng002}@ucr.edu

ABSTRACT

Determining the meaningful texture features for human embryonic stem cells (hESC) is important in the development of online hESC classification system. This paper proposes the use of novel support vector machine with bio-inspired one-against-all (OAA) multi-class structural and statistical Gabor descriptors for hESC classification. It investigates the statistical histogram information at four different orientations and two different window sizes of the Gabor filter. It demonstrates that statistical Gabor features are more accurate and reliable than a conventional histogram based features.

Index Terms— Classification, Gabor filter, Human embryonic stem cells (hESC), One-against-all (OAA)

1. INTRODUCTION

Human embryonic stem cells (hESC) are derived from the inner cell mass of developing blastocysts and can be maintained indefinitely in vitro in a pluripotent state [1]. Because of their ability to self-renew and their potential to differentiate into any cell type, hESC provide a unique resource for regenerative medicine, basic research on human prenatal development, and toxicological testing of drugs and environmental chemicals [2][3]. In the current studies, biologists have used time-lapse imaging of cells to monitor dynamic behavior of hESC in different experimental conditions [4][5][6]. While performing these studies, we observed that hESC undergo dynamic blebbing during the first 20-60 minutes after plating, and if they do not attach to their substrate during the first hour after plating, they undergo apoptosis. Due to the fact that dynamic blebbing occurs in the first hour of incubation, it can be used to evaluate hESC health following plating, and it can also serve as the basis for a rapid toxicological assay. Although it takes little time to perform the blebbing assay, manual analysis of the resulting video data is time-consuming and subjective. Therefore, analysis tool such as a hESC classification system is essential for quantified analysis. An automated classification system can help biologists to identify interesting behaviors of hESC easily. It can provide the biologists the statistics of different types of stem cell in the current analysis. It can assist the biologists to draw a conclusion for a particular experiment.

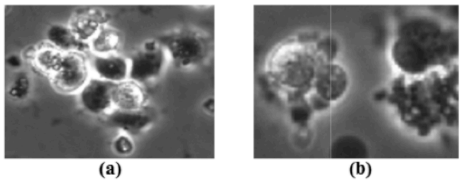

Fig. 1 (a) Cell colony; (b) close-knit cells.

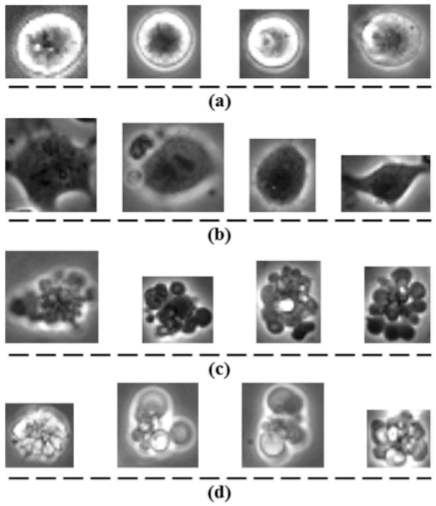

Fig. 2 (a) Unattached cells; (b) attached cells; (c) dynamically blebbing cells; (d) apoptotically blebbing cells.

A hESC video is made up by frames of phase contrast image. Each frame comprises of two major categories. One is the multi-cell category shown in Fig. 1, the other is the single cell category shown in Fig. 2. There are two types of

multi-cells: 1) cell colony; 2) close-knit cells. Cell colony comprises of two or more single cells. The close-knit cells consist of two or more individual components. Each component can either be a single cell or a cell colony. The four intrinsic types of single cell are: 1) unattached cell (U); 2) attached cell (A); 3) dynamically blebbing cell (D); 4) apoptotically blebbing cell (AP). Since the assays are formed by the four intrinsic cell types, the classification of these cell types is important. Therefore, this paper focuses on the classification of the four intrinsic types of stem cell.

2. RELATED WORKS

There is no existing study for the automated classification of hESC. However, there are many classification studies that use features based on local binary patterns (LBP), local phase quantization (LPQ), and Gabor filtering. The simplest LBP compare each of its eight neighbors' intensity values with its center intensity value [7]. The neighboring pixel has a value of 1 if its intensity value is greater than the center intensity value. Otherwise, the neighboring pixel has a value of 0. LPQ obtain local frequency coefficients for each pixel at certain frequencies [8]. The coefficients are then quantized and translated into a histogram. The Gabor filter is a 2D Gaussian kernel function that is modulated by a sinusoidal plane wave at certain frequency and orientation [9][10]. A histogram is generally generated from the Gabor filtered image as a feature vector. Conventionally, a histogram is either a histogram of the entire image or a cascaded histogram from smaller windows of the image. However, resizing the dataset is needed for a cascaded histogram. Since our dataset images have an average size of 58 by 60 pixels, we use the histogram of the entire image in this paper for all histogram based comparison methods.

TABLE 1
AVERAGE CROSS-CORRELATION (CC) VALUES FOR CELL TYPES SHOWN IN FIGURE 2 (GRAY SCALE ONLY)

Histogram Based	**U**	**A**	**D**	**AP**
U	*0.6578*	0.1064	0.3184	**0.5982**
A	0.1064	*0.7468*	**0.6187**	0.1531
D	0.3184	**0.6187**	*0.6960*	0.3945
AP	**0.5982**	0.1531	0.3945	*0.7365*

(a)

Statistics Based	**U**	**A**	**D**	**AP**
U	*0.9992*	0.9981	0.9984	**0.9990**
A	0.9981	*0.9996*	**0.9988**	0.9979
D	0.9984	**0.9988**	*0.9985*	0.9982
AP	**0.9990**	0.9979	0.9982	*0.9992*

(b)

Underline & italics denote correlation and bold denotes highest CC value in the row.

Our contribution in this paper is to introduce a binary support vector machine (SVM) with a bio-inspired one-against-all (OAA) model for multi-class classification [11][12]. We use statistical Gabor wavelet for multi-class classification. We investigate the Gabor filter parameters and find out parameters that yield the best performance in multi-class classification for the four intrinsic cell types. We compared the conventional histogram based features and the statistics based features in this paper.

3. TECHNICAL APPROACH

In this section, we first explain our motivation and the problem formulation. We also briefly explain Gabor filter in subsection 3.2. We then elaborate on the statistical Gabor descriptors for multi-class classification.

3.1. Motivation and Problem Formulation

The four intrinsic hESC considered in this paper have characteristics such as roundedness, elongatedness and bubble-like shape. Texture is important to distinguish these cell types, so we use texture features in this paper. Since Gabor filters give useful descriptors at different window sizes, frequencies and orientations, we investigated the Gabor filter for classification of hESC. For the choice of a classifier, we have used the SVM. The SVM is a binary decision classifier. As a result, we also adopted OAA model for multi-class classification. The OAA model is the most efficient way to use SVM for multi-class classification [12].

The OAA model for multi-class classification is bio-inspired. Based on biological insights, the unattached cells are round, and they are brighter in intensity than attached and dynamically blebbing cells. As shown in Fig. 2, unattached and apoptotically blebbing cells have high intensity values while attached and dynamically blebbing cells are darker in intensity. Table 1 shows support for our biological insights. The cross-correlation (CC) value between cell types using either the gray scale histogram based or statistics based features shows that highest CC value among cell types separates the 4 cell types into 2 groups. Since apoptotically blebbing cell has a higher average CC value than unattached cell, the positive and negative sets at level 0 of OAA hierarchy is given by: {U} and {A, D, AP}.

With the aforementioned facts, we deduced a bio-inspired structure for one-against-all classification method. Fig. 3 shows how the OAA method is constructed with SVM as a fundamental classifier. If the input image is recognized as negative sample, then further classification is needed. The positive and negative samples at each level are chosen based on how a particular cell type is prevalently different from the rest of other cell types.

Since we are developing an online classification system, accuracy, reliability and low time complexity are essential. The fewer the feature descriptors, the lower the

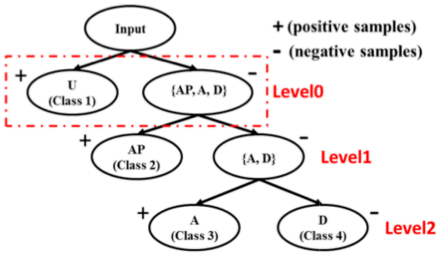

Fig. 3 Bio-inspired one-against-all (OAA) model for multi-class classification.

time complexity. Therefore, we only considered five key statistical features; 1) mean; 2) mode; 3) entropy; 4) variance; 5) energy.

3.2. Gabor Filter

Gabor filtering is a convolution of an image, I , with a 2D Gaussian kernel, G , that is modulated by a sinusoidal plane wave. The Gaussian equation is shown in equation (1). The modulation, M, is shown in equation (2). The final modulated Gabor equation, G_M, is shown in equation (3) [9].

$$G(x,y) = \frac{1}{2\pi s_x s_y} e^{-\frac{1}{2}\left(\left(\frac{x}{s_x}\right)^2 + \left(\frac{y}{s_y}\right)^2\right)} \quad (1)$$

$$M(x,y,f,\theta) = \cos\left(2\pi f\left(x\cos(\theta) + y\sin(\theta)\right)\right) \quad (2)$$

$$G_M(x,y,f,\theta) = G(x,y)M(x,y,f,\theta) \quad (3)$$

Note that x ∈ $[-S_x, S_x]$, y ∈ $[-S_y, S_y]$, S_x and S_y are standard deviation in the x and y direction, f is the frequency of sinusoidal wave, and θ is the orientation. The final filtered image, I_G , is obtained by convolution as shown in below [9][10]. (Note that * denotes convolution.)

$$I_G = I * G_M \quad (4)$$

3.3. Statistical Descriptors

The statistical descriptors are derived directly from the histogram of the image with or without filtering. The following equations show the statistics based descriptors that are derived from the histogram of an image [13].

$$\mu = \frac{1}{S}\sum_{n=0}^{N} nH(n) \quad (5)$$

$$\psi = \max_n\left(\mathrm{H(n)}\right) \quad (6)$$

$$\rho = -\sum_{n=0}^{N} \frac{H(n)}{S}\log_2\left(\frac{H(n)}{S} + 1\right) \quad (7)$$

$$\sigma^2 = \frac{1}{S}\sum_{n=0}^{N} H(n)(n-\mu)^2 \quad (8)$$

$$\phi = \frac{\sum_{n=0}^{N}\left(H(n)\right)^2}{\left(\sum_{n=0}^{N} H(n)\right)^2} \quad (9)$$

where H is the histogram of the image and n is an index which spans from 0 to N. In this paper, N is 255. S is the total number of pixels in the image. μ, ψ, ρ, σ^2 and ϕ are mean, mode, entropy, variance and energy of the image. The statistical descriptors of all the texture filters mentioned in this paper are obtained using the above equations.

4. EXPERIMENTAL RESULTS

4.1. Data

All time lapse videos were obtained with a BioStation IM under 20x objective [14]. Each video frame was taken roughly 2 minutes apart for the purpose of data variation from frame to frame. The frames in the video were phase contrast images with 600 x 800 resolution. Each frame was then decomposed into smaller images by a cell region detection algorithm [15]. The four intrinsic cell types were then identified by an expert stem cell biologist from the pool of images, and datasets were generated from 8 videos.

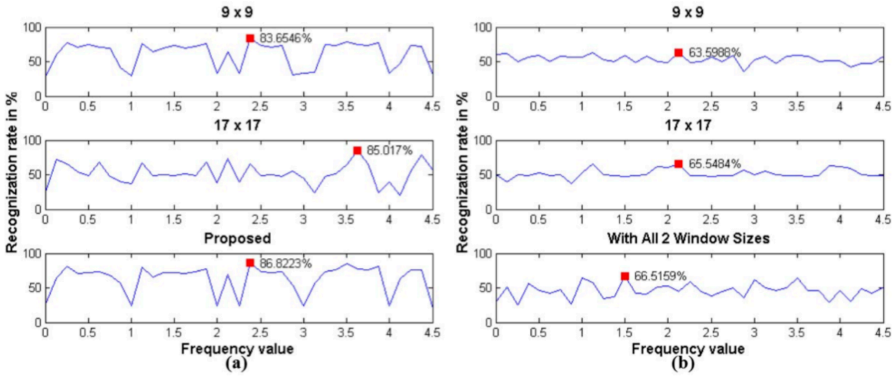

Fig. 4 (a) Methods with Gabor statistics for each window size under different frequencies; (b) Methods with Gabor histogram for each window size under different frequencies. (red square denotes optimal point.)

TABLE 2: TEN-FOLD COMPARISON RESULTS IN THIS PAPER (4 ORIENTATIONS ARE USED FOR ALL GABOR METHODS)

Features	Unattached	AP Blebbing	Attached	Dynam. Blebbing	ARR
Gray Scale Histogram	29.04%	94.91%	0.00%	100.00%	55.99%
Gray Scale Statistics	0.00%	0.94%	0.00%	95.00%	23.99%
LBP Histogram	34.11%	11.70%	0.00%	97.75%	35.89%
LBP Statistics	0.68%	5.85%	5.63%	83.50%	23.92%
LPQ Histogram	43.56%	24.15%	0.00%	100.00%	41.93%
LPQ Statistics	1.78%	3.58%	18.16%	76.25%	24.94%
Gabor Histogram (9x9)	70.41%	86.42%	0.00%	93.75%	62.64%
Gabor Statistics (9x9)	78.49%	87.17%	71.55%	97.50%	83.68%
Gabor Histogram (17x17)	82.74%	74.34%	0.00%	99.00%	64.02%
Gabor Statistics (17x17)	86.58%	80.38%	76.89%	100.00%	85.96%
Gabor Wavelet Histogram*	62.88%	87.74%	0.00%	99.75%	62.59%
Proposed*	**78.08%**	**90.38%**	**78.25%**	**100.00%**	**86.68%**

*** denotes windows 9 x 9 and 17 x 17 are used. AP denotes apoptotically, and ARR denotes average recognition rate.**

There was no preprocessing on the dataset images, and their average size is about 58 by 60 pixels. The test datasets had 269 images with 73 images of unattached cell, 103 images of attached cell, 40 images of dynamically blebbing cell and 53 images of apoptotically blebbing cell. The training datasets had a total of 120 images with 30 images for each cell type.

4.2. Parameters

For the Gabor filter, we used 4 orientations and 2 different window sizes [10]. The orientations in degrees were 0, 45, 90 and 135. The window sizes were 9 x 9 and 17 x 17. The frequencies were learned with search from 0 to 4.5 with a 0.125 step size [9]. Note that we used 4 orientations in each window to construct either a histogram based or statistics based descriptor. The optimal frequencies for the Gabor methods are selected when the average recognition rate is achieved and it is shown in Fig. 4. The proposed method used all orientations and window sizes for the descriptors. The frequencies used in the histogram based methods were 2.125, 2.125 and 1.5 for 9 x 9, 17 x 17 and method with all window sizes. For the Gabor statistics based descriptors, we used frequencies 2.375, 3.625 and 2.375 for 9 x 9, 17 x 17 and the proposed. For the LBP, we used 8 neighbors [7]. For the LPQ, the default parameters had the window size of 3 x 3 and decorrelation value of 1 [8].

4.3. Results

We compared the proposed method with histogram and statistics based methods in gray scale, LBP, LPQ and Gabor features at different window sizes with four orientations. The Gabor histogram based method with 2 window sizes and 4 orientations was also compared. As shown in Table 2, the proposed method yields ten-fold accuracies of 78.08% for unattached cell, 90.38% for apoptotically blebbing cell, 78.25% for attached cell and 100.00% for dynamically blebbing cell. The proposed method outperformed all other methods in the average recognition rate (ARR) for all cell types. The methods with Gabor descriptors outperformed all the other non-Gabor descriptors with the minimum of 6.6% and the maximum of 62.76% in ARR. Among the Gabor filter based methods, the proposed method outperforms them by at least 0.72% and at most 24.09%. The histogram based features were not able to distinguish attached and dynamically blebbing cells. As a result, the ten-fold accuracy of the attached cells was 0% for all histogram based features. We also tested the proposed features with nearest-neighbor (NN) method, and it yielded 83.95% in ARR [16]. The SVM outperformed NN by 2.73%.

5. CONCLUSIONS

In this paper, we used SVM with bio-inspired one-against-all model and feature vector derived from Gabor statistics for multi-class classification. In term of accuracy, the Gabor with statistical descriptors methods outperformed all other comparison methods as shown in Table 2. In term of feature vector size, the proposed approach has only 40 descriptors which is less than a single histogram that contains 256 descriptors. In term of reliability, the ten-fold average recognition rate of the proposed method is differed from the predicted accuracy under optimal frequency shown in Fig. 4 by less than 0.2%.

6. ACKNOWLEDGEMENT

This research was supported by NSF-IGERT: Grant DGE 0903667 and by TRDRP: Grant 20XT-0118 and 20FT-0084.

7. REFERENCES

[1] J. A. Thomson, J. Itskovitz-Eldor, S. S. Shapiro, M. A. Waknitz, J. J. Swiergiel, V. S. Marshall and J. M. Jones, "Embryonic stem cell lines derived from human blastocysts," *Science*, vol. 282, no. 5395, pp. 1145-1147, 1998.

[2] Z. Zhu and D. Huangfu, "Human pluripotent stem cells: an emerging model in developmental biology," *Development*, vol. 140, pp. 705-717, 2013.

[3] P. Talbot and S. Lin, "Mouse and human embryonic stem cells: can they improve human health by preventing disease?," *Current Topics in Medicinal Chemistry*, vol. 11, no. 13, pp. 1638-1652, 2011.

[4] S. Lin, V. Tran and P. Talbot, "Comparison of toxicity of smoke from traditional and harm reduction cigarettes using embryonic stem cells as a novel model for pre-implantation development," *Human Reproduction*, vol. 24, pp. 386-397, 2009.

[5] S. Lin, S. Fonteno, J-H Weng, and P. Talbot, "Comparison of toxicity of smoke from conventional and harm reduction cigarettes using human embryonic stem cells," *Toxicological Sciences*, vol. 118, pp. 202-212, Aug. 2010.

[6] S. Lin, S. Fonteno, S. Satish, B. Bhanu and P. Talbot, "Video bioinformatics analysis of human embryonic stem cell colony growth," *Journal of visualized experiments*, vol. 39, May 2010.

[7] T. Ojala, M. Pietikäinen and T. Mäenpää, "Gray scale and rotation invariant texture classification with local binary patterns," *Proc. ECCV*, vol. 1842, pp. 404-420, 2000.

[8] J. Heikkila, V. Ojansivu and E. Rahtu, "Improved blur insensitivity for decorrelated local phase quantization," *International Conference on Pattern Recognition*, pp. 818-821, 2010.

[9] I. Fogel and D. Sagi, "Gabor filters as texture discriminator," *Biol. Cybern.*, vol 61, pp. 103-113, 1989.

[10] W. K. Kong, D. Zhang and W. Li, "Palmprint feature extraction using 2-D Gabor filters," *Pattern Recognition*, vol. 36, pp. 2339-2347, 2003.

[11] C. Chang, C. Lin and C. J. Lin, "LIBSVM: a library for support vector machines," 2001, Available Online: http://www.csie.ntu.edu.tw/~cjlin/libsvm.

[12] O. Chapelle, P. Haffner and V. Vapnik, "SVMs for histogram-based image classification," *IEEE transactions on Neural Networks*, vol. 10, no. 5, pp. 1055-1064, 1999.

[13] R.C. Gonzalez and R.E. Woods, Digital Image Processing: Third Edition. Upper Saddle River, NJ: Pearson Education Inc., pp. 795-856, 2008.

[14] Nikon. Biostation-IM. http://www.nikoninstruments.com/content/search?SearchText=Biostation+IM (accessed 22 Jan. 2014).

[15] B.X. Guan, B. Bhanu, P. Talbot, & S. Lin, "Automated human embryonic stem cell detection," *Proc. 2nd IEEE International Conf. On Health Informatics, Imaging and System Biology*, pp. 75-82, Sept. 2012.

[16] J. H. Friedman, J. Bentely and R. A. Finkel, "An algorithm for finding best matches in logarithmic expected time," *ACM Trans. On Mathematical Software*, vol. 3, No. 3, pp. 209- 226, 1977.

This article has been accepted for publication in a future issue of this journal, but has not been fully edited. Content may change prior to final publication. Citation information: DOI 10.1109/TCBB.2015.2480091, IEEE/ACM Transactions on Computational Biology and Bioinformatics

Extraction of Blebs in Human Embryonic Stem Cell Videos

Benjamin X. Guan*, *Student Member, IEEE*, Bir Bhanu*, *Fellow, IEEE*
Prue Talbot** and Nikki Weng**

Abstract— Blebbing is an important biological indicator in determining the health of human embryonic stem cells (hESC). Especially, areas of a bleb sequence in a video are often used to distinguish two cell blebbing behaviors in hESC; dynamic and apoptotic blebbings. This paper analyzes various segmentation methods for bleb extraction in hESC videos and introduces a bio-inspired score function to improve the performance in bleb extraction. Full bleb formation consists of bleb expansion and retraction. Blebs change their size and image properties dynamically in both processes and between frames. Therefore, adaptive parameters are needed for each segmentation method. A score function derived from the change of bleb area and orientation between consecutive frames is proposed which provides adaptive parameters for bleb extraction in videos. In comparison to manual analysis, the proposed method provides an automated fast and accurate approach for bleb sequence extraction.

Index Terms— Bleb extraction, bioinformatics, bio-inspired, human embryonic stem cell (hESC).

1 Introduction

Blebs are membrane protrusions that appear and disappear from the surface of cells. The extraction of blebs and their changing area over time in live videos is important for understanding the mechanisms and function of human embryonic stem cell (hESC) blebbing behavior. The nature of blebbing behavior can be used to evaluate cell health-dynamic blebs indicate healthy cells and apoptotic blebs indicate dying cells. The ability to analyze rates of bleb formation and retraction are important in the field of toxicology and could form the basis of an assay that depends on a functional cytoskeleton [1] [2] [3]. The biologists attempt to clarify the difference between dynamic and apoptotic blebbings in hESC by comparing the time of their occurrences. Blebbing is considered to be related to signaling pathways. It is significant for biologists to have enough evidence to determine whether Calcium, ATP and P2X7 inhibitors can change the blebbing behavior through the Rho-Rock Pathway or not. Inhibitors can alter blebbing behavior by either blocking the pathway leading to myosin activation or inhibit myosin directly. The dynamic segmentation of blebs enables a rapid analysis to make quantified measurements on very large datasets collected with hESC under different experimental conditions. This will lead to the understanding of foundational mechanisms and function of blebbing which can ultimately control/regulate dynamic blebbing in hESC.

Two types of bleb characterization are needed to be understood: Image characterization and physical characterization of blebs. Image characterization of blebs requires the development of computational methods that can provide high detection accuracy with minimum user interaction with blebs in video. Physical characterization of blebs provides enormous understanding of the dynamic cell behavior. For example, it enables the development of a method to prevent blebbing behaviors that lead to cell death. Bleb detection in video is a way to accelerate our understanding of blebs for the development of its physical characterization.

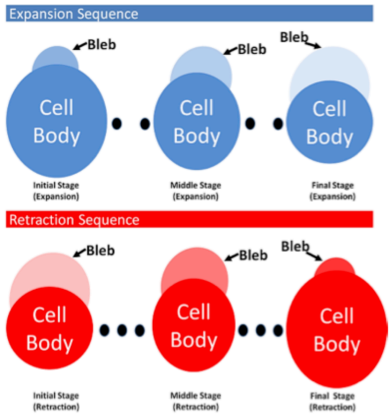

Fig. 1. Expansion and retraction processes occuring over time.

This paper uses the H9 line of hESC (WiCell, Madison, WI.) which are normally about 10 microns in diameter. The average bleb-to-cell body ratio is about 16:57. In 2D images, a single cell can have an average of 6 or a maximum of 11 blebs with a 20x objective. This paper is in-

* *B.X. Guan and B. Bhanu are with the Center for Research in Intelligent Systems and the Department of Electrical and Computer Engineering, University of California-Riverside, Riverside, CA 92521 USA (e-mail: xguan001@ucr.edu; bhanu@cris.ucr.edu).*
** *P. Talbot and N. Weng are with the Stem Cell Center, University of California Riverside, Riverside, CA 92521 USA (e-mail: talbot@ucr.edu; jweng002@ucr.edu).*

xxx-xxxx/0x/$xx.00 © 200x IEEE Published by the IEEE Computer Society

This article has been accepted for publication in a future issue of this journal, but has not been fully edited. Content may change prior to final publication. Citation information: DOI 10.1109/TCBB.2015.2480091, IEEE/ACM Transactions on Computational Biology and Bioinformatics

tended to explain the bleb formation phenomena and to introduce a method to segment sequences of bleb regions in video for further analysis. Bleb formation consists of two processes: 1) expansion; 2) retraction [4] [5]. In the first stage, the bleb expands sporadically. During the retraction stage, the bleb either retracts back and disappears or partially retracts. Complete bleb retraction normally occurs during dynamic blebbing, which is a characteristic of healthy cells. However, if bleb retraction does not occur or occurs slowly, the cell is likely undergoing apoptosis or cell death. Fig. 1 shows the sequences of both bleb expansion and retraction. During expansion, bleb size increases while cell body size decreases. In contrast, during bleb retraction, bleb size decreases while cell body size increases. At the final stage of expansion, the bleb is called an *intermediate bleb*. The intermediate bleb indicates that transition from expansion to retraction is occurring. The intermediate bleb has the maximum bleb size in full bleb formation process.

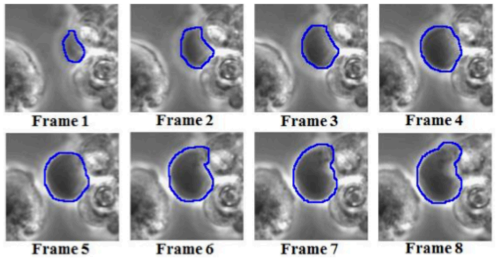

Fig. 2. Example of bleb expansion sequence.

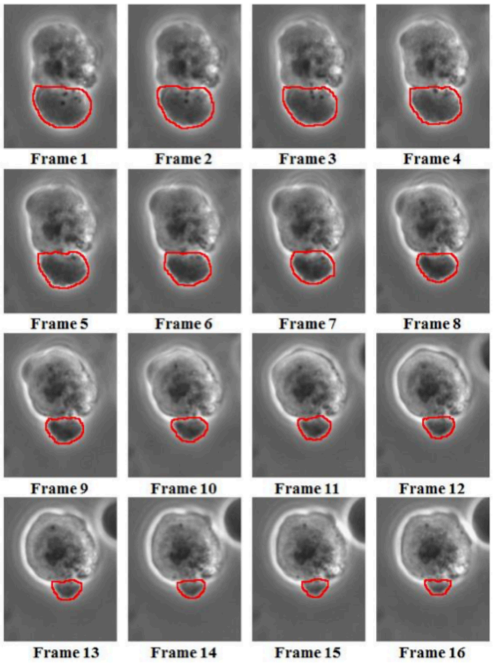

Fig. 3. Example of bleb retraction sequence.

Fig. 2 and 3 show phase contrast images of blebbing sequences for both expansion and retraction. The expansion and retraction processes are visually similar but biologically distinct [6] [7]. Based on our observation on the videos, the change in area and orientation between blebs from the consecutive frames are important for the segmentation of blebs. With the modeled distributions of the change in area and orientation, adaptive parameters for segmentation methods are possible. Additionally, segmentation methods with adaptive parameters improve the performance in the detection of blebs.

Section 2 presents related work and the contributions of this paper. Section 3 describes the technical approach in detail. Section 4 provides experimental results and discussions on video data. Finally, Section 5 provides the conclusions of the paper.

2 Related Work And Contributions

2.1 Blebbing of Human Embryonic Stem Cell

Both hESC dynamic and apoptotic blebbings consist of two processes: expansion and retraction. From our previous studies, we observed that hESC tends to have more blebs as well as having a higher rate of blebbings. Apoptotic blebblings in non-healthy cells are commonly studied. However, blebs exist in both healthy and non-healthy cells. Therefore, it is essential to analyze dynamic blebbings in healthy cells. Understanding the differences between both dynamic and apoptotic blebbings' mechanism and function can lead to a breakthrough in development of regenerative medicine.

2.2 Computational Models for Blebbing

Charras et al. [4] [5] reasoned that blebbing depends on parameters such as pressure, membrane-cortex, adhesion energy and membrane tension of a cell. The plasma membrane of a hESC is attached under tension to a cortex of filaments. If the connection with the filaments is weakened, a bleb is produced by an event of pouring cytoplasmic fluid into the weakened region. When the growth of the bleb stops, the bleb either retracts or stays the same. If an actin cortex reforms under the bleb membrane, retraction is likely to occur and is driven by myosin-II.

StryChalski et al. [6] assumed that blebbing occurs due to detachment of the cytoskeleton from the plasma membrane, which produces a pressure-driven flow of cytosol toward the area of detachment and into the area of expansion. They proposed a computational model of blebbing based on the mechanics of intracellular fluid, the actin cortex, and the cell membrane. The model considers the bleb formation time as a function of parameters derived from cytoplasmic properties [6]. A similar model has been proposed in [7].

2.3 Detection and Segmentation Methods for Cells

Due to the abundance, heterogeneity, dimensionality and complexity of the image data, manual image processing

This article has been accepted for publication in a future issue of this journal, but has not been fully edited. Content may change prior to final publication. Citation information: DOI 10.1109/TCBB.2015.2480091, IEEE/ACM Transactions on Computational Biology and Bioinformatics

and analysis is not feasible. In the analysis of biological images, the performance of a segmentation method heavily depends on the tuning of segmentation parameters [8]. It is a tedious process yet the tuned parameters do not guarantee the same performance on similar images. Object detection and segmentation are essential in the analysis of hESC and they are closely related.

Guan et al. [9] [10] present bio-inspired detection/segmentation methods for hESC in phase contrast images. Their segmentation method was developed based on the image property differences between cell region and background [10]. Yin et al. [11] also developed a cell segmentation method by using a bag of local Bayesian classifier. Their segmentation method classifies each pixel in a region with a Bayesian classifier. However, both methods only work for extraction of cell and cell colony from a phase contrast video. In this paper, we are concerned with the detection of blebs of a single cell. Note that blebs are part of the cell with similar image properties. Since there is no previous work on detection of blebs, we will exploit the following four commonly used methods for image segmentation: *region growing*, *normalized cut*, *meanshift* and *watershed*.

Region growing (RG) by Adams et al. [12] [13] grows a region initially from a seed point and groups its neighboring pixels to its region based on their similarity coefficient threshold. *Normalized cut (NC)* method by Shi et al. [14] is a graph based approach, and performs segmentation by maximizing association within groups while minimizing disassociation between groups. *Meanshift (MS)* method by Comaniciu et al. [15] is a well-known density based approach that partitions the image by assigning pixels into clusters with the same mode [16] [17]. *Watershed (WS)* method performs a flooding process on a gradient image where it starts at a local minima and builds watersheds to separate adjacent catchment basins [18] [19].

2.4 Challenges for Bleb Analysis

Since a bleb is part of the cell, it brings the following challenges: i) bleb intensity and texture vary for different cells; ii) blebs are connected to the cell body; iii) blebs have similar intensity/texture as the cell body or background; iv) neighboring blebs share similar intensity and texture. Fig. 4 shows a set of expanding and retracting blebs. Although these blebs look similar, they are different from each other in intensity and texture. Therefore, the conventional segmentation methods with constant parameters will not work well on all the bleb images in a video. Most importantly, blebbing is a dynamic process, and the bleb properties change over time. As a result, subsequent blebs in the same video sequence might have different image properties. Consequently, the performance of *RG*, *NC*, *MS* and *WS* methods will suffer from any constant input parameters.

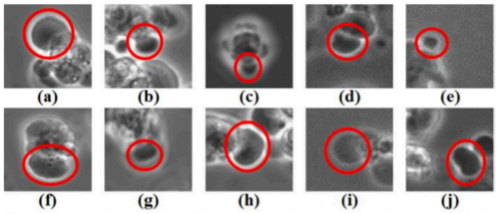

Fig. 4. A sample of blebs. (Note: the variety of blebs that are circled in these images)

TABLE 1
DEFINITION OF THE SYMBOLS USED IN THIS PAPER

Symbol	Definition
t	Index for the distribution functions.
$E(t; A_E)$	Exponential distribution function.
A_E	Inverse scaling parameter of the exponential.
$G(t; A_G, B_G)$	Gaussian distribution function.
A_G	Mean for the Gaussian distribution.
B_G	Standard deviation for the Gaussian distribution.
$LN(t; A_{LN}, B_{LN})$	Lognormal distribution function.
A_{LN}	Location parameter of the lognormal.
B_{LN}	Scale parameter of the lognormal.
$\mathcal{P}(t; A_{\mathcal{P}})$	Poisson distribution function.
$A_{\mathcal{P}}$	Mean parameter of the Poisson.
$RL(t; A_{RL})$	Rayleigh distribution function.
A_{RL}	Mode parameter of the Rayleigh distribution.
$GAM(t; A_{GAM}, B_{GAM})$	Gamma distribution function.
A_{GAM}	Shape parameter of the Gamma distribution.
B_{GAM}	Scale parameter of the Gamma distribution.
$S_{\alpha,\phi}(\Delta A, \Delta\theta)$	Bio-inspired optimization metric.
$\Delta A, \Delta\theta$	Values for change in bleb area and orientation.
α	Parameters vector of modeled ΔA distribution.
ϕ	Parameters vector of modeled $\Delta\theta$ distribution.

2.5 Contributions of this Paper

We propose a bio-inspired optimization method for the segmentation of dynamic blebs. The proposed approach adapts parameters for images in the bleb formation process: expansion and retraction. The parameters for the bio-inspired metric are derived directly from the distributions of change in area and orientation between consecutive blebs. Since the health status of a cell can be determined from the bleb formation process, it is important to improve the accuracy in bleb detection. Therefore, the proposed optimization method is essential in quantitative analysis of cell health.

3 TECHNICAL APPROACH

In this section, we first introduce the derivation of the statistical models for bio-inspired optimization metric. We also elaborate on the optimization metric. We then explain the segmentation methods for the detection of blebs in video. In addition, a summary of the proposed algorithm and a flowchart for segmentation in video are also provided. For the convenience of the reader, a summary of the symbols used in this paper is given in Table 1. Fig. 5 shows the overview of the proposed system.

The proposed system uses exhaustive search to obtain an optimal solution. Segmentation result with specific parameters is given a score in the bio-inspired optimization step. This score is calculated based on the modeled distributions. The modeled distributions are the general-

This article has been accepted for publication in a future issue of this journal, but has not been fully edited. Content may change prior to final publication. Citation information: DOI 10.1109/TCBB.2015.2480091, IEEE/ACM Transactions on Computational Biology and Bioinformatics

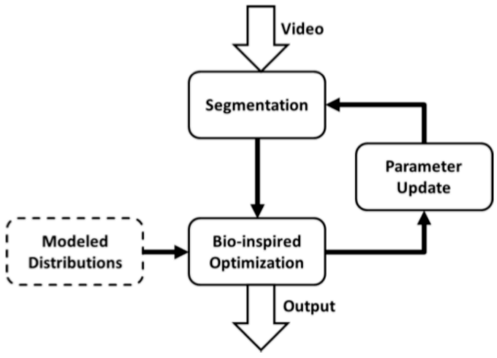

Fig. 5. Overview of the proposed system.

ized distributions obtained from distribution fitting the change in bleb areas and orientations.

3.1 Modeled Distributions

3.1.1 Motivation

Since image properties of a bleb changes with time, constant parameters of segmentation methods will perform poorly. Therefore, dynamic parameters with consideration of bleb changes over time are needed for the segmentation methods. Based on our observation of the hESC blebbing videos, we concluded that ΔA and $\Delta\theta$ between consecutive frames provide relative behavior of a bleb over time. Fig. 1 shows an example of how bleb changes over time. Therefore, we obtain the generalized models for ΔA and $\Delta\theta$ distributions through model fitting.

3.1.2 Learning the Distributions of ΔA and $\Delta\theta$

We used a model fitting technique on the actual distributions of ΔA and $\Delta\theta$. Equations (1)-(6) are used in our model fitting technique [20] [21]. Definitions of parameters for the following equations are provided in Table 1.

Exponential distribution function:

$$E(t; A_E) = A_E e^{-A_E t} \quad (1)$$

Gaussian distribution function:

$$G(t; A_G, B_G) = \frac{1}{B_G\sqrt{2\pi}} e^{-\frac{(t-A_G)^2}{2B_G^2}} \quad (2)$$

Lognormal distribution function:

$$LN(t; A_{LN}, B_{LN}) = \frac{1}{tB_{LN}\sqrt{2\pi}} e^{-\frac{(\ln(t)-A_{LN})^2}{2B_{LN}^2}} \quad (3)$$

Poisson distribution function:

$$\mathcal{P}(t; A_{\mathcal{P}}) = \frac{A_{\mathcal{P}}^t}{t!} e^{-A_{\mathcal{P}}} \quad (4)$$

Rayleigh distribution function:

$$RL(t; A_{RL}) = \frac{t}{A_{RL}^2} e^{\frac{-t^2}{2A_{RL}^2}} \quad (5)$$

Gamma distribution function:

$$GAM(t; A_{GAM}, B_{GAM}) = \frac{1}{\Gamma(A_{GAM}) B_{GAM}^{A_{GAM}}} t^{A_{GAM}-1} e^{-\frac{t}{B_{GAM}}} \quad (6)$$

$\Gamma(*)$ is a gamma function operator. The optimal parameters and mean squared error (MSE) for each distribution is shown in Table 2. Since we are seeking model that yields low MSE for each distribution, we conclude that both ΔA and $\Delta\theta$ can be characterized as Gamma distributions. Fig. 6 shows the best models that fit the actual ΔA and $\Delta\theta$ distributions.

TABLE 2
MODELED DISTRIBUTIONS: PARAMETERS AND MSE

Parameters and MSE for ΔA Distribution

Parameters	Exp.	Gauss.	Log.	Poisson	Rayleigh	Gamma
A	61.810	61.810	2.617	61.810	103.134	**0.431**
B	'NA'	132.356	2.983	'NA'	'NA'	**143.288**
MSE	1.07E-03	1.43E-03	9.48E-04	2.10E-03	1.77E-03	**9.29E-04**

Parameters and MSE for Δθ Distribution

Parameters	Exp.	Gauss.	Log.	Poisson	Rayleigh	Gamma
A	19.474	19.474	0.970	19.474	31.116	**0.338**
B	'NA'	39.535	4.369	'NA'	'NA'	**57.574**
MSE	4.29E-03	6.25E-03	4.11E-03	8.80E-03	8.31E-03	**3.60E-03**

Note: A and B → parameters for each model distribution;
MSE → mean squared error; Bold → best result ; Exp. → Exponential;
Gauss. → Gaussian; Log. → Lognormal; NA → not applicable.

3.2 Bio-inspired Optimization for Segmentation

For this paper, the segmentation methods with the bio-inspired optimization are called *bio-optimized* methods. The bio-inspired optimization metric provides an adaptive solution to the segmentation problem with following two steps. First, the metric yields scores for a set of parameters in a particular segmentation method and retains the corresponding scores of the parameters in the set. Second, optimal solution is selected from the parameters with the highest score.

3.2.1 Bio-inspired Optimization Metric

The optimization metric $S_{\alpha,\phi}(\Delta A, \Delta\theta)$ considers D_1 and D_2, the modeled ΔA and $\Delta\theta$ distributions, as two independent distributions. $D_1(\Delta A; \alpha)$ is a score of ΔA in a distribution that is parameterized by α. $D_2(\Delta\theta; \phi)$ is a score of $\Delta\theta$ in a distribution that is parameterized by ϕ. The general form of the optimization metric is shown below.

$$S_{\alpha,\phi}(\Delta A, \Delta\theta) = D_1(\Delta A; \alpha) * D_2(\Delta\theta; \phi) \quad (7)$$

The final form of the optimization metric is shown in the following equation:

$$S_{max} = \max_{\Delta A, \Delta\theta} S_{\alpha,\phi}(\Delta A, \Delta\theta) \quad (8)$$

The optimized S_{max} is found when the metric score is maximized with a given ΔA and $\Delta\theta$ values.

3.2.2 Parameter Update

The initial centroid and area of the bleb are given by the end user. Bleb centroid tells the algorithm about the region of interest. Bleb area is needed to calculate ΔA and $\Delta\theta$ for the segmentation parameters. The subsequent bleb centroid and bleb area in a video sequence are generated automatically. The bleb centroid of the next frame is the centroid of the current detected bleb region [22]. Moreover, the assumption of smooth/gradual transition between consecutive frames is made for bleb formation processes. The detected bleb at each frame is a region where the optimal parameters of a segmentation method that maxim-

This article has been accepted for publication in a future issue of this journal, but has not been fully edited. Content may change prior to final publication. Citation information: DOI 10.1109/TCBB.2015.2480091, IEEE/ACM Transactions on Computational Biology and Bioinformatics

ized the bio-inspired optimization metric which is described in equation (8). Equation (8) uses the modeled distributions as shown in Fig. 6 to calculate the scores for the segmentation parameters. When the maximum score is found, the estimated bleb centroid and current bleb area for the next frame are updated. The output of the method for a video is a sequence of binary masks of the detected blebs.

3.3 Segmentation Methods Compared

In this section, we explain each segmentation method in detail and show how bio-optimization is achieved. We also provide Table 3 which summarizes the search range for each optimization parameter.

TABLE 3
OPTIMIZATION PARAMETERS AND RANGES

Method	Optimizing Parameters	Range of Optimization
Region Growing	Similarity coefficient threshold	0 to 1 with step 0.01
NCUT	Number of clusters	2 to 10 with step 1
Meanshift	Spatial bandwidth	1 to 8 with step 1
	Range bandwidth	1 to 8 with step 1
Watershed	Suppressing value/threshold	1 to 254 with step 1

3.3.1 Region Growing

Region growing is a region based segmentation method. It starts with an initial seed point and iteratively evolves its region by evaluating its region's neighboring contour. It groups the contour pixels based on a similarity threshold. The contour pixels are grouped into the region if the similarity between the pixel and region feature is less than a threshold. As a result, the performance of the region growing method depends on the selection of the threshold. In the bio-optimized region growing approach, the threshold is an adaptive parameter that is needed to be found. The search range for the optimal threshold in the bio-optimized region growing is from 0 to 1 with stepsize 0.01.

3.3.2 Normalized Cut

Normalized cut is a graph based approach. It considers each pixel as a vertex and edge as a connection weight between pixels. The main objective of this approach is to minimize the disassociation between the groups while maximizing the association within the groups. The number of possible groups is determined by the end user. As a result, the number of possible groups in an image is the adaptive parameter in the bio-optimized normalized cut. Since the bleb is the foreground and the rest of the image is the background, we have at least two components in the image. Based on observation, each frame consists of five different regions: 1) background; 2) cell body; 3) halo; 4) bleb; 5) debris or part of neighboring cell. Since the image contains these five basic regions, the number of expected regions is five under ideal condition. With the consideration of the worst case scenario, we double the number of possible components in an image. Therefore, the search range is set to be 2 to 10 components.

3.3.3 Meanshift

Meanshift method is a density based approach. It has two parameters: spatial and range bandwidths. It also requires the minimum size of a region. In this paper, the minimum size of a region is set to be 60 pixels which is the smallest recognizable bleb. The spatial range determines the size of the search window that computes the meanshift. The range bandwidth determines the window size that is used to compute the feature. In this paper, the optimization search range for the spatial bandwidth is from 1 to 8 and the range bandwidth is from 1 to 8.

3.3.4 Watershed

Watershed is a topological based method. It is often applied on a gradient image. It partitions the image into two different sets: catchment basins and watershed line. The watershed method floods the topographic surface of a gradient image from its regional minima. It builds watershed lines to prevent waters in different catchment basins from merging. In this paper, the gradient image is the Euclidean distance transform of the marker image. The marker im-

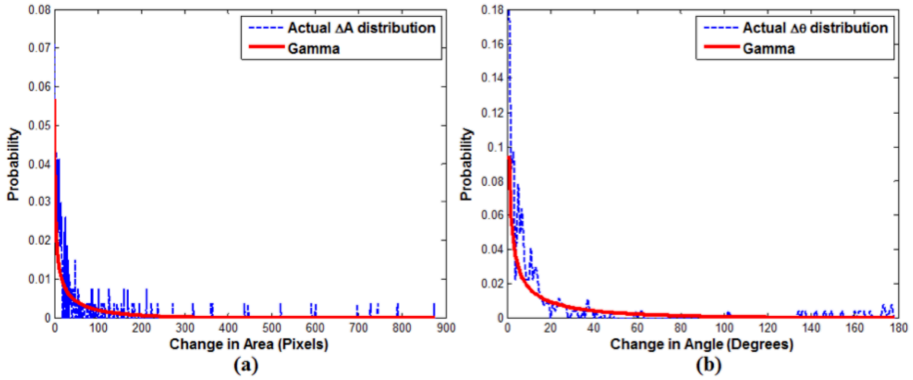

Fig. 6. Modeled fitting for (a) ΔA distribution and (b) $\Delta\theta$ distribution are Gamma. (ΔA and $\Delta\theta$ are derived from both expansion and retraction datasets.)

This article has been accepted for publication in a future issue of this journal, but has not been fully edited. Content may change prior to final publication. Citation information: DOI 10.1109/TCBB.2015.2480091, IEEE/ACM Transactions on Computational Biology and Bioinformatics

age (binary image) is obtained with the extended minimum of the original image [19]. The extended minimum approach depends on the suppressing value to binarize the image. Therefore, the suppressing value is the adaptive parameter for the bio-optimized watershed. Since the image is an 8 bit image, the search range for the optimal suppressing value is from 1 to 254.

3.4 Summary of the Proposed Algorithm

Algorithm 1 Bleb extraction in video

Input: V is a video with a total F number of frames. B_{cent} and B_{area} are given bleb centroid and area initially.
Output: R is a sequence of binary masks of blebs.

1: **procedure** BlebExtraction(V, B_{cent} , B_{area})
2: Set frame index f to 1.
3: Perform segmentation with different segmentation parameters on f_{th} video frame, $V(f)$.
4: Obtain optimal parameters/segmentation result by equation (8)
5: Save optimal segmentation result to $R(f)$
6: Update estimated B_{cent} and B_{area} with $R(f)$
7: Increment frame index f by 1.
8: Repeat steps 3 to 7 until index $f > F$
9: Output segmentation result R.
10: **end procedure**

To further explain the segmentation block as shown in Fig. 5, a flow chart of segmentation is provided in Fig. 7. It shows a general process of segmentation with a set of parameters for a single bleb.

4 Experimental Results

4.1 Data

All time lapse videos were obtained with a BioStation IM [23] [24]. The frames in the video are phase contrast images. The videos were acquired using 20x objective with 600 x 800 resolution. Each video frame is acquired at 2 seconds time interval. For this experiment, we have 26 expansion, 30 retraction, and 9 full bleb formation videos which are cropped randomly from the BioStation's raw videos. A total of 692 frames are in the 65 videos. The ΔA and $\Delta\theta$ distributions are derived from the first 13 expansion and 15 retraction videos. The remaining 13 expansion, 15 retraction and 9 full bleb formation videos are used as the testing dataset. The ground-truth for all videos was generated manually by expert biologists.

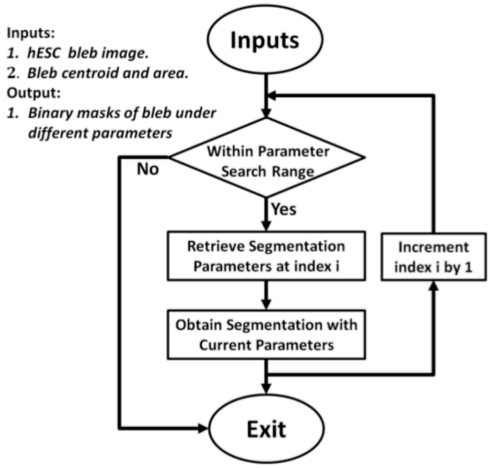

Fig. 7. Flowchart for segmentation

4.2 Parameters

4.2.1 Segmentation Parameters of Standard Algorithms

The conventional segmentation parameters are identified individually by a receiver operating characteristic (ROC) curve [25]. Fig. 8 shows the ROC curves for four different segmentation methods. The training frames are obtained from the first frame of each 28 experimental videos. The optimal point is the maximum true positive rate within the range of 0 to 0.4 false positive rates. Based on the ROC, we determined that the region growing's optimal similarity threshold is set to be 0.15. For the normalized cut method, the optimal number of components is 2. For meanshift, optimal range and spatial bandwidths are 1 and 3. Its minimum region criterion is set to 60 pixels which is the smallest recognizable bleb size. For watershed, the optimal suppressing value is 115.

4.2.2 Parameters for the Proposed Method

For the proposed method, the first bleb area and center were needed initially for each video sequence and were provided by the end user. The modeled distribution parameters are also required for the bio-inspired optimization metric. Since ΔA and $\Delta\theta$ distributions are best fitted by Gamma distribution with different parameters, we uses their optimal parameters in the optimization metric.

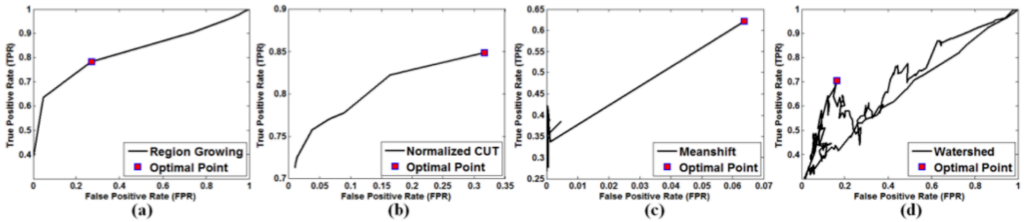

Fig.8. ROC plot for (a) Region growing, (b) normalized CUT, (c) meanshift, (d) watershed.

This article has been accepted for publication in a future issue of this journal, but has not been fully edited. Content may change prior to final publication. Citation information: DOI 10.1109/TCBB.2015.2480091, IEEE/ACM Transactions on Computational Biology and Bioinformatics

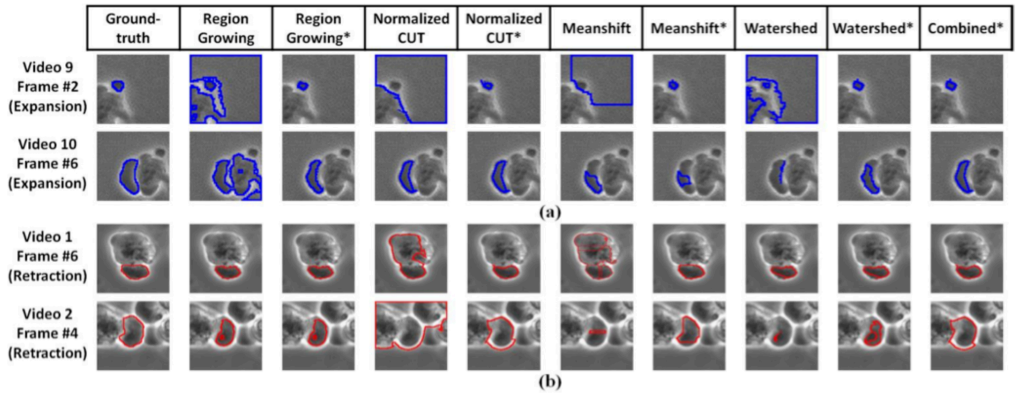

Fig.9. Visual comparisons of four different blebs with results from (a) expansion process and (b) retraction process. (Note that frames from two sets of videos are used in the figure: expansion and retraction videos. Expansion results are outlined in blue and retraction results are outlined in red.)

ΔA distribution is modeled as Gamma distribution with parameters A_{GAM} and B_{GAM} equal to 0.431 and 143.288. $\Delta\theta$ distribution is also modeled as a Gamma distribution with parameters A_{GAM} and B_{GAM} equal to 0.338 and 57.574. The aforementioned model parameter values are used in equations (7) and (8).

There are two different types of parameters that need to be considered for our approach: (a) the parameters of the optimization metric and (b) the range of parameters of the selected segmentation method. For the optimization metric parameters, the parameter sensitivity depends on the size and the quality (independent samples, image quality, etc.) of the representative dataset. Typically, a larger training dataset can better generalize the parameters in the optimization metric. For each segmentation method, the range of parameter values depends on the method and the characteristics of video frames. For this paper, a detailed discussion is provided in Subsections 3.3 and 4.2 to determine the parameter range for each segmentation method. This range provided good segmentation results for the videos used in this paper.

4.3 Performance Measures

For comparison, we use methods suggested by Shattuck et al. [25][26]. Our comparison metrics are Jaccard similarity (JAC), Dice coefficient (DIC), sensitivity (SEN), specificity (SPC) and balanced accuracy (BAC). The JAC is a measure of similarity between experimental results and the ground-truth. The DIC is the measure of the agreement between experimental results and ground-truth. The SEN is a measurement of the proportion of actual positives which are correctly identified. The SPC measures the proportion of the actual negatives which are correctly identified. Moreover, the true positive rate (TPR) is equivalent to SEN, and the false positive rate (FPR) is same as SPC subtracted from 1. The BAC is an average of SEN and SPC. The equation for each metric is shown below:

$$JAC = \frac{TP}{(TP+FP+FN)} \quad (9)$$

$$DIC = \frac{2TP}{(2TP+FP+FN)} \quad (10)$$

$$SEN = \frac{TP}{(TP+FN)} \quad (11)$$

$$SPC = \frac{TN}{(FP+TN)} \quad (12)$$

$$BAC = \frac{SEN+SPC}{2} \quad (13)$$

The variables are defined as follows: 1) true positive (TP), 2) true negative (TN), 3) false positive (FP) and 4) false negative (FN). TP indicates the overlapped region of the detected bleb's binary mask and the bleb ground-truth's binary mask. TN is the overlapped region of the detected background's binary mask and the background ground-truth's binary mask. FP is the detected background's binary mask that is falsely identified as part of the bleb region. FN is the detected bleb's binary mask that is falsely identified as part of the background.

4.4 Segmentation Results

4.4.1 Qualitative Results

The bio-inspired optimization on all segmentation methods, combined bio-optimized method, has better performance on average than other methods as shown in Fig. 9. All bio-optimized methods have segmentation results closer to the ground-truth. Since the segmentation with the bio-optimized methods is constrained by the bio-optimization metric, over-segmentation was less significant than the conventional methods.

4.4.2 Quantitative Results

The segmentation methods with the bio-inspired optimization outperformed all conventional segmentation methods in this paper. The conventional meanshift with fixed parameters outperforms the other conventional segmentation methods. Based on average mean JAC and average mean DIC of the three datasets, the bio-optimized meanshift outperformed the conventional meanshift by more than 12%. In addition, all other bio-optimized methods outperformed their conventional counterparts by at least 5% in both mean JAC and mean DIC. The mean JAC and mean DIC performances for each dataset are shown in Table 4.

This article has been accepted for publication in a future issue of this journal, but has not been fully edited. Content may change prior to final publication. Citation information: DOI 10.1109/TCBB.2015.2480091, IEEE/ACM Transactions on Computational Biology and Bioinformatics

The top four performers based on the average mean JAC and average mean DIC of the three datasets are ranked as combined bio-optimized method, bio-optimized region growing, bio-optimized meanshift and bio-optimized watershed. Table 5 shows corresponding average mean JAC and average mean DIC for the aforementioned top performers. The combined bio-optimized method is the best performer in all datasets. The combined bio-optimized method also has 79.19% in average mean BAC which is the best overall performance in all

TABLE 4
RESULTS ON EXPERIMENTAL DATA (NOTE ALL VALUES ARE IN PERCENTAGE)

Results on Expansion Videos

Metric	JAC				DIC				SEN				SPC			
Method	**Min**	**Max**	**Std**	**Mean**	**Min**	**Max**	**Std**	**Mean**	**Min**	**Max**	**Std**	**Mean**	**Min**	**Max**	**Std**	**Mean**
Region Growing	2.02	77.96	26.42	21.92	3.95	87.61	29.36	30.16	68.75	99.86	9.27	84.09	3.00	99.97	40.49	49.04
Region Growing*	**43.22**	**80.69**	**12.97**	**60.11**	**60.35**	**89.31**	**10.12**	**74.33**	**43.22**	**81.18**	**12.59**	**63.73**	**95.56**	**100.00**	**1.38**	**99.44**
NCUT	1.97	62.11	20.49	21.75	3.86	76.62	25.05	31.87	58.87	100.00	15.24	78.43	2.86	100.00	35.73	61.18
NCUT*	9.58	62.07	20.16	42.90	17.48	76.59	21.97	57.19	55.17	83.62	9.14	67.71	85.61	100.00	5.12	95.48
Meanshift	2.57	69.74	20.84	39.78	5.01	82.18	23.74	53.68	46.25	73.55	8.89	60.95	35.84	100.00	17.58	90.94
Meanshift*	**29.83**	**73.70**	**13.67**	**55.24**	**45.95**	**84.86**	**12.02**	**70.19**	**29.89**	**77.36**	**14.63**	**58.62**	**96.93**	**100.00**	**0.82**	**99.59**
Watershed	3.89	61.10	18.21	21.99	7.50	75.85	22.37	32.99	43.11	100.00	18.61	76.91	23.51	98.77	22.81	73.91
Watershed*	**27.55**	**73.99**	**15.17**	**45.99**	**43.20**	**85.05**	**14.00**	**61.67**	**27.55**	**78.63**	**17.69**	**51.14**	**96.21**	**100.00**	**1.16**	**99.14**
Combined*	**45.06**	**78.87**	**9.05**	**60.68**	**62.13**	**88.18**	**7.05**	**75.17**	**48.12**	**81.18**	**9.76**	**65.30**	**96.30**	**100.00**	**0.99**	**99.54**

Results on Retraction Videos

Metric	JAC				DIC				SEN				SPC			
Method	**Min**	**Max**	**Std**	**Mean**	**Min**	**Max**	**Std**	**Mean**	**Min**	**Max**	**Std**	**Mean**	**Min**	**Max**	**Std**	**Mean**
Region Growing	4.68	32.64	8.39	12.78	8.94	49.22	12.36	21.80	63.59	98.30	8.97	81.43	4.71	86.57	30.18	53.22
Region Growing*	**15.21**	**74.55**	**14.86**	**57.26**	**26.41**	**85.42**	**14.65**	**71.54**	**37.82**	**74.57**	**9.63**	**62.31**	**76.12**	**100.00**	**6.12**	**98.22**
NCUT	2.69	16.66	4.15	10.95	5.24	28.57	6.85	19.50	66.24	100.00	11.66	84.78	5.78	82.21	22.09	51.10
NCUT*	14.30	62.62	13.31	43.20	25.03	77.01	13.98	59.13	47.47	86.69	11.76	62.90	78.70	99.95	6.67	95.51
Meanshift	4.82	70.87	20.30	42.23	9.21	82.95	21.73	56.52	41.91	76.04	10.12	59.96	77.12	100.00	6.74	95.34
Meanshift*	**41.63**	**73.77**	**9.22**	**58.30**	**58.78**	**84.90**	**7.53**	**73.25**	**46.53**	**76.84**	**7.99**	**60.97**	**99.02**	**100.00**	**0.28**	**99.77**
Watershed	5.73	49.89	14.23	22.22	10.83	66.57	18.07	34.40	32.34	94.16	19.34	62.27	53.77	98.63	15.08	82.52
Watershed*	**26.62**	**68.73**	**13.41**	**47.59**	**42.04**	**81.47**	**12.84**	**63.40**	**28.08**	**78.80**	**15.09**	**52.63**	**97.83**	**100.00**	**0.75**	**99.21**
Combined*	**41.63**	**73.77**	**9.42**	**59.92**	**58.78**	**84.90**	**7.60**	**74.52**	**49.48**	**82.05**	**10.41**	**65.73**	**96.35**	**100.00**	**1.00**	**99.32**

Results on Full Bleb Formation Videos

Metric	JAC				DIC				SEN				SPC			
Method	**Min**	**Max**	**Std**	**Mean**	**Min**	**Max**	**Std**	**Mean**	**Min**	**Max**	**Std**	**Mean**	**Min**	**Max**	**Std**	**Mean**
Region Growing	1.25	21.45	6.60	5.07	2.47	35.33	10.78	9.05	62.65	91.32	8.55	78.76	2.83	96.43	33.70	55.73
Region Growing*	**9.71**	**55.08**	**13.71**	**40.79**	**17.70**	**71.03**	**16.15**	**56.56**	**11.45**	**55.28**	**13.11**	**41.94**	**99.60**	**100.00**	**0.13**	**99.93**
NCUT	1.44	4.08	0.84	2.49	2.85	7.85	1.60	4.84	87.05	100.00	4.55	97.22	1.43	77.52	19.56	45.31
NCUT*	1.47	36.22	15.49	16.95	2.89	53.18	22.62	26.33	50.05	99.67	21.48	73.29	1.43	99.53	35.23	71.28
Meanshift	3.57	48.78	17.02	37.46	6.90	65.58	21.82	52.10	16.04	56.30	12.18	47.85	83.05	99.93	5.57	97.90
Meanshift*	**11.15**	**55.79**	**13.02**	**43.33**	**20.06**	**71.62**	**15.36**	**59.23**	**14.02**	**56.62**	**12.54**	**44.46**	**99.42**	**100.00**	**0.19**	**99.92**
Watershed	2.81	64.93	20.20	17.24	5.47	78.74	24.10	25.75	19.48	88.07	19.07	64.57	76.63	99.77	8.44	90.86
Watershed*	**13.52**	**58.35**	**19.19**	**33.97**	**23.82**	**73.70**	**21.17**	**48.03**	**17.72**	**69.68**	**20.19**	**37.56**	**98.08**	**100.00**	**0.62**	**99.71**
Combined*	**11.15**	**55.79**	**13.14**	**44.07**	**20.06**	**71.62**	**15.51**	**59.92**	**14.02**	**56.62**	**12.62**	**45.24**	**99.42**	**100.00**	**0.19**	**99.92**

* denotes a bio-optimized method and bold denote the top four performers. Combined* denotes optimization on all four segmentation methods.

This article has been accepted for publication in a future issue of this journal, but has not been fully edited. Content may change prior to final publication. Citation information: DOI 10.1109/TCBB.2015.2480091, IEEE/ACM Transactions on Computational Biology and Bioinformatics

TABLE 5
TOP FOUR PERFORMERS

Measure	Combined*	Region Growing*	Meanshift*	Watershed*
Average Mean JAC	**54.89%**	52.72%	52.29%	42.52%
Average Mean DIC	**69.87%**	67.48%	67.56%	57.70%
Average Mean BAC	**79.17%**	77.59%	77.22%	73.23%

*** denotes a bio-optimized method, and bold denotes best performance.**

three experimental datasets. The combined bio-optimized's average mean BAC shows that at least 79% of bleb and background regions can be accurately retrieved.

To determine the statistical significance of the top four performers (combined*, region growing*, meanshift*, and watershed*) as shown in Table 5, a t-test with 5% significant level for the combined* method against the other three top performers (region growing*, meanshift* and watershed*) is carried out. The t-test was done for DIC measure. We found that the bio-optimized combined method failed to reject the null hypothesis for the bio-optimized region growing and bio-optimized meanshift methods. However, the null hypothesis was rejected for the bio-optimized watershed method. The acceptance of the null hypothesis was due to the fact that the combined* approach favored one individual segmentation method in some experiments. Therefore, it essentially yields the same solution as a particular segmentation method.

Based on Table 4, the bio-optimized methods generally have lower average standard deviation (Std) in both JAC and DIC measures than their counterparts with exceptions of bio-optimized *NC* and bio-optimized *RG*. The conventional *NC* and *RG* have consistent lower performances in both JAC and DIC for all three datasets. Since the cell and the bleb are dynamically changing over time, adaptive parameters that are found with the bio-optimized metric improves the performance and consistency of the segmentation methods significantly. The fixed parameters in the conventional segmentation methods are not sufficient to handle the blebbing sequence where the bleb's image properties change over time.

Due to the bio-optimized metric, the bio-optimized segmentation methods did not suffer from severe over-segmentation. The bio-optimized segmentation methods' solutions are bounded by the bio-optimized metric. Therefore, the bio-optimized segmentation methods have higher performance for the blebbing sequence than the conventional segmentation methods. The constant parameters in the conventional segmentation approaches are the cause for their low performance. The proposed methods with adaptive parameters are able to capture the local region of the bleb more accurately.

TABLE 6
COMPUTATIONAL TIME STATISTICS PER FRAME IN SECONDS

Method	Min	Max	Mean	Std
Region Growing	0.02	1.39	0.32	0.35
Region Growing*	2.42	38.52	12.52	11.99
NCUT	0.29	4.81	1.74	1.48
NCUT*	2.36	47.56	16.49	14.18
Meanshift	0.02	0.17	0.06	0.05
Meanshift*	0.33	3.86	1.22	1.13
Watershed	0.01	0.05	0.02	0.01
Watershed*	1.67	12.79	4.85	3.28
Combined*	6.61	122.54	36.14	35.07

*** denotes a bio-optimized method.**

4.5 Discussion

4.5.1 Effect of Model Parameters on Performance

The parameters that characterized the ΔA and $\Delta\theta$ distributions are essential in the optimization process. Inaccurate model parameter values might lead to either under-segmentation or over-segmentation of the bleb. As a result, the model parameters found through model fitting are important for equation (7) which yields a score for each element in a set of segmentation parameters.

4.5.2 Effect of Bleb and Cell Sizes on Performance

The bleb and cell body size are important for the performance in the optimization process. There are three types of small blebs that have poor performance in the proposed method:

1. Small blebs due to smaller cell (typically a small bleb has roughly 240 pixels or less).
2. Small blebs at the initial stage of the expansion.
3. Small blebs at the final stage of the retraction.

The smaller blebs for any process are not fully developed and often have similar intensity and texture as the cell body. Therefore, over-segmentation is bound to happen if the cell body and its bleb share similar image properties. The proposed method yields a lower value in comparison metric for small blebs. However, larger cells with larger blebs often perform better. A typical large bleb has 1700 or more pixels.

4.5.3 Automation in Segmentation

The bio-optimized segmentation method is a semi-automated approach in which the initial bleb centroid and area is given by the user in the first frame. Automation is done on the subsequent frames in a video for the optimal segmentation result with equation (8). However, it still alleviates the biologist's burden from complete manual extraction of bleb in video for analysis. The proposed yields bleb area distribution and provides the bleb boundary over time. It is a useful data mining approach to help biologist quantify analyses on dynamic and apoptotic blebbing behavior.

4.5.4 Time Complexity

Since the proposed method was an iterative optimization process, it yielded higher time complexity for all bio-optimized segmentation methods. The best performer among the bio-optimized segmentation methods was the combined bio-optimized method. However, it required an average of 36.14 seconds to process a single frame as shown in Table 6. The bio-optimized meanshift was the only bio-optimized method with the lowest time complexity. The tradeoffs between the bio-optimized meanshift and combined bio-optimized method were performance and time complexity. The experiments were done on a

This article has been accepted for publication in a future issue of this journal, but has not been fully edited. Content may change prior to final publication. Citation information: DOI 10.1109/TCBB.2015.2480091, IEEE/ACM Transactions on Computational Biology and Bioinformatics

laptop with an Intel(R) Core™ 2 DUO CPU processor that run at 2.53 GHz.

5 Conclusions

The bio-optimized segmentation methods have better performances than their conventional counterparts. Their high performance shows the modeled distributions is significant for segmenting blebs in videos. With the bio-inspired optimization metric, low performance due to over-segmentation is reduced. However, the segmentation method might not generate an ideal/exact solution to optimize the metric tightly due to the fact that a bleb has similar image properties to its cell body. The over-segmentation in the approach is the inability of the segmentation method to discern the bleb from its cell body.

In terms of biological contribution, this paper introduces a new concept that the bleb formation/retraction process can be used as a biological indicator of cell health. Healthy cells retract their blebs back to the cell body, while non-healthy cells do not retract them or retract them slowly. In terms of a computational contribution, this paper suggests a bio-inspired optimization metric to segment bleb regions. We introduced an approach to improve bleb detection accuracy by using adaptive parameters instead of using constant parameters for all bleb frames in a video. The proposed segmentation methods with adaptive parameters found by the bio-inspired optimization metric has consistently higher performance. In the future work, we will consider incorporating shape prior information in our approach for accurate bleb detection [27][28]. Shape prior will introduce shape variability consideration in our approach [27].

This work can be used by biologists to evaluate the state of health of hESC in culture in various experimental conditions. It could be valuable in drug screening and in toxicological studies where short times to an endpoint are desirable, as well as resource and time saving. It may be adaptable in the future to high throughput screening of chemicals and drugs that need to be evaluated for embryotoxicity.

Acknowledgment

This research was supported by National Science Foundation Integrated Graduate Education Research and Training (NSF-IGERT): Video Bioinformatics Grant DGE 0903667 and by Tobacco-Related Disease Research Program (TRDRP): Grant 20XT-0118 and Grant 22RT-0127.

References

[1] S. Lin, et al., "Comparison of the toxicity of smoke from conventional and harm reduction cigarettes using human embryonic stem cells," in *Toxicol Sci.*, vol. 118, pp. 202-212, Aug. 2010.

[2] Z. Zhu and D. Huangfu, "Human pluripotent stem cells: an emerging model in developmental biology," in *Development*, vol. 140, pp. 705-717, 2013.

[3] P. Talbot and S. Lin, "Mouse and human embryonic stem cells: can they improve human health by preventing disease?," in *Current Topics in Medicinal Chemistry*, vol. 11, no. 13, pp. 1638-1652, 2011.

[4] G.T. Charras, et al., "Life and times of a cellular bleb," in *Biophysical Journal*, vol. 94, pp. 1836-1853, March 2008.

[5] J. Tinevez, U. Schulze, G. Salbreux, J. Roensch, J. Joanny and E. Paluch, "Role of cortical tension in bleb growth," in *PNAS*, vol. 106, no. 44, pp.18581-18586, Nov. 2009.

[6] W. Strychalski and R. D. Guy, "A computational model of bleb formation," in *Mathematical Medicine and Biology*, pp. 1-16, Jan. 2012.

[7] F. Y. Lim, Y. L. Koon and K. H. Chiam, "A computational model of amoeboid cell migration," in *Computer Methods in Biomechanics and Biomedical Engineering*, pp. 1-12, Jan. 2013.

[8] E. Meijering, "Cell segmentation: 50 years down the road [life sciences]," in *IEEE Signal Processing Magazine*, vol. 29, no. 5, pp. 140–145, 2012.

[9] B.X. Guan, B. Bhanu, P. Talbot, & S. Lin, "Detection of non-dynamic blebbing single unattached human embryonic stem cells," in *IEEE International Conference on Image Processing*, pp. 2293-2296, Sept. 2012.

[10] B.X. Guan, B. Bhanu, P. Talbot, & S. Lin, "Automated human embryonic stem cell detection," in *Proc. 2nd IEEE International Conf. On Health Informatics, Imaging and System Biology*, pp. 75-82, Sept. 2012.

[11] Z. Yin, R.Bise, T. Kanade and M. Chen, "Cell segmentation in microscopy imagery symposium on biomedical imaging," in *ISBI*, pp. 125-128, 2010.

[12] R. Adams and L. Bischoff, "Seeded region growing," in *IEEE Trans. PAMI*, vol. 16, no. 6, pp. 641-647, June 1994.

[13] Y. Sun and B. Bhanu, "Reflection symmetry-integrated image segmentation," in *IEEE Trans. Pattern Analysis and Machine Intelligence*, vol. 34, no. 9 , pp. 1827-1841, Sept. 2012.

[14] J. Shi and J. Malik, "Normalized cuts and image segmentation," in *IEEE Trans. PAMI*, vol. 22, no. 8, pp. 888-905, Aug. 2000.

[15] D. Comaniciu and P. Meer, "Mean Shift: A robust approach toward feature space analysis," in *IEEE Trans. Pattern Analysis and Machine Intelligence*, vol. 24, no. 5, pp. 603-619, May 2002.

[16] P. Meer and B. Georgescu, "Edge detection with embedded confidence," in *IEEE Trans. Pattern Anal. Machine Intelligence*, vol. 23, no. 12, pp. 1351-1365, December 2001.

[17] C. Christoudias, B. Georgescu and P. Meer, "Synergism in low level vision," in *IEEE 16th International Conference on Pattern Recognition*, vol. 4, pp. 150-155, 2002.

[18] F. Meyer, "Topographic distance and watershed lines," in *Signal Processing*, vol. 38, pp. 113-125, July 1994.

[19] P. Soille, Morphological Image Analysis: Principles and Applications, Springer-Verlag, pp. 170-171, 1999.

[20] E. W. Weisstein, "Least Squares Fitting," From MathWorld--A Wolfram Web Resource, [Online]. Available: http://mathworld.wolfram.com/LeastSquaresFitting.html. [Accessed 10 Jan. 2015].

[21] E. W. Weisstein, "Statistical Distributions," From MathWorld--A Wolfram Web Resource, [Online]. Available: http://mathworld.wolfram.com/topics/StatisticalDistributions.html. [Accessed 10 Jan. 2015].

[22] R.C. Gonzalez and R.E. Woods, Digital Image Processing: Third Edition, Upper Saddle River, NJ: Pearson Education Inc., pp. 689-794, 2008.

[23] "Biostation-IM," Nikon, [Online]. Available: http://www.nikoninstruments.com/Products/Light-Microscope-Systems/Live-Cell-Screening-Systems/BioStation-IM. [Accessed 10 Jan. 2015].

[24] P. Talbot, N. zur Nieden, S. Lin, I. Martinez, B.X. Guan and B. Bhanu, "Use of video bioinformatic tools in stem cell toxicology," in *Handbook on Nanotoxicology, Nanomedicine and Stem Cell Use in Toxicology*, April 2013.

[25] M. Pepe, G.M. Longton, and H. Janes, "Comparison of receiver operating characteristics curves," UW Biostatistics Working Paper Series- Working Paper 323[eLetter] January 2008. [Online]. Available:

This article has been accepted for publication in a future issue of this journal, but has not been fully edited. Content may change prior to final publication. Citation information: DOI 10.1109/TCBB.2015.2480091, IEEE/ACM Transactions on Computational Biology and Bioinformatics

http://biostats.bepress.com/uwbiostat/paper323. [Accessed 10 Jan. 2015].

[26] D. W. Shattuck, S. R. Sandor-Leahy, K. A. Schaper, D. A. Rottenberg and R. M. Leahy, "Magnetic resonance image tissue classification using a partial volume model," in *NeuroImage*, Vol. 13, pp. 856-876, 2001.

[27] T. F. Cootes, C. J. Taylor, D. H. Cooper and J. Graham, "Active shape models – their training and application," *Computer Vision and Image Understanding*, Vol. 61, No. 1, pp. 38-59, January 1995.

[28] S. Zhang, Y. Zhan, M. Dewan, J. Huang, D. N. Metaxas, X. S. Zhou, "Towards robust and effective shape modeling: Sparse shape composition," *Medical Image Analysis*, Vol. 16, No. 1, pp. 265-277, 2012.

Benjamin X. Guan received the B.S. degree with high honor in June 2008 and M.S. degree in December 2009 in Electrical Engineering from the University of California, Riverside. He is currently pursuing his Ph.D. degree in Electrical Engineering at the University of California, Riverside. His research interests are human embryonic stem cell segmentation, detection and classification. He received the Best Paper Award from the IEEE International Conference on Health Informatics, Imaging and System Biology in 2012. He is a member of the IEEE.

Bir Bhanu (S'72 -- M'82 -- SM'87 -- F'95) received the S.M. and E.E. degrees in electrical engineering and computer science from the Massachusetts Institute of Technology, Cambridge, MA, USA; the Ph.D. degree in electrical engineering from the University of Southern California, Los Angeles, CA, USA; and the M.B.A. degree from the University of California, Irvine, CA. Dr. Bhanu is a Distinguished Professor of electrical and computer engineering, and serves as the Founding Director of the Interdisciplinary Center for Research in Intelligent Systems, University of California at Riverside (UCR), Riverside, CA. In addition, he serves as the Director of the National Science Foundation (NSF) Interdisciplinary Graduate Education, Research, and Training Program in video bioinformatics, Interim Chair Department of Bioengineering (since July 2014) and the Director (since 1991) of Visualization and Intelligent Systems Laboratory. He was the founding faculty in the Bourns College of Engineering and the founding Professor of electrical engineering with UCR, and served as its First Chair from 1991 to 1994. Since 1991, 2006, and 2008, he has been a Cooperative Professor of computer science and engineering, bioengineering, and mechanical engineering, respectively, with UCR. He was a Senior Honeywell Fellow with Honeywell Inc., Minneapolis, MN, USA. He has been with the Faculty of the Computer Science, University of Utah, Salt Lake City, UT, USA, and with Ford Aerospace and Communications Corporation, Newport Beach, CA; French Institute for Research in Computer Science and Control (INRIA); and IBM San Jose Research Laboratory, San Jose, CA. He has been the Principal Investigator of various programs for the NSF, the Defense Advanced Research Projects Agency (DARPA), NASA, the Air Force Office of Scientific Research, the Office of Naval Research, the Army Research Office, and other agencies and industries in the areas of video networks, video understanding, video bioinformatics, learning and vision, image understanding, pattern recognition, target recognition, biometrics, autonomous navigation, image databases, and machine-vision applications. He is the coauthor of the books Computational Learning for Adaptive Computer Vision (to be published), Human Recognition at a Distance in Video (Berlin, Germany: Springer-Verlag, 2011), Human Ear Recognition by Computer (Berlin, Germany: Springer-Verlag, 2008), Evolutionary Synthesis of Pattern Recognition Systems (Berlin, Germany: Springer-Verlag, 2005), Computational Algorithms for Fingerprint Recognition (Norwell, MA: Kluwer, 2004), Genetic Learning for Adaptive Image Segmentation (Norwell, MA: Kluwer, 1994), and Qualitative Motion Understanding (Norwell, MA: Kluwer, 1992). He is the coeditor of Video Bioinformatics - From Live Imaging to Knowledge (Springer Computational Biology Series, 2015), Computer Vision Beyond the Visible Spectrum (Berlin, Germany: Springer-Verlag, 2004), Distributed Video Sensor Networks (Berlin, Germany: Springer-Verlag, 2011), and Multibiometrics for Human Identification (Cambridge, U.K.: Cambridge University Press, 2011). He is the holder of 18 (five pending) U.S. and international patents. He has more than 475 reviewed technical publications, including over 135 journal papers and 44 book chapters. Dr. Bhanu is a Fellow of the Institute of Electrical and Electronics Engineers (IEEE), American Association for the Advancement of Science, the International Association of Pattern Recognition, Fellow of American Institute of Medical and Biological Engineering (AIMBE) and the International Society for Optical Engineering. He has served as the General Chair for the IEEE Conference on Computer Vision and Pattern Recognition (CVPR), the IEEE Conference on Advanced Video and Signal-Based Surveillance, the Association for Computing Machinery/IEEE Conference on Distributed Smart Cameras, the DARPA Image Understanding Workshop, the IEEE Workshops on Applications of Computer Vision (founded in 1992, now Winter Applications of Computer Vision Conference), and the CVPR Workshops on Learning in Computer Vision and Pattern Recognition, Computer Vision Beyond the Visible Spectrum, and Multi-Modal Biometrics. He has been on the Editorial Board of various journals and has edited special issues of several IEEE Transactions, such as the IEEE TRANSACTIONS ON PATTERN ANALYSIS AND MACHINE INTELLIGENCE, IEEE TRANSACTIONS ON IMAGE PROCESSING, IEEE TRANSACTIONS ON SYSTEMS, MAN, AND CYBERNETICS -- PART B: CYBERNETICS, IEEE TRANSACTIONS ON ROBOTICS AND AUTOMATION, AND IEEE TRANSACTIONS ON INFORMATION FORENSICS AND SECURITY. He served on the IEEE Fellow Committee from 2010 -- 2012. He was the recipient of the Best Conference Papers and Outstanding Journal Paper Awards, and the Industrial and University Awards for Research Excellence, Outstanding Contributions, Team Efforts and Doctoral/Dissertation Advisor/Mentor Award.

Prue Talbot is a Professor of Cell Biology and the Director of the UCR Stem Cell Center and Core. Her lab is interested in using stem cells to prevent disease and in the effects of tobacco products on human health, including prenatal development. Some of her recent projects have included working with engineers to develop video bioinformatics tools to study morphological and dynamic changes in stem cells during growth and differentiation under normal and stressful conditions and to be able to predict adverse reactions of cells to chemical treatments.

Nikki Jo-Hao Weng received the B.S. degree in Chang Gung University, Taiwan. She is currently a Ph.D student in the cell, molecular and developmental biology program at UC Riverside. She also participates in the UC Riverside NSF integrated graduated education research and training program (IGERT) on video bioinformatics.